UNIVERSITY OF MILANO - BICOCCA

Department of Biotechnology and Biosciences

Ph.D. Program in Biology (XXVIII cycle)

INVESTIGATING THE EFFECTS OF DRUG-LOADED NANOPARTICLES ON THE CELLULAR BEHAVIOR OF PROLIFERATIVE DISEASES

Tutor: Prof. Paolo Tortora

Cotutor: Prof. Davide Prosperi

Coordinator: Prof. Paolo Tortora

Ph.D. Candidate:

Laura Pandolfi

Mat. 775149

Academic year 2015

Contents

INTRODUCTION

CHAPTER 1 Antiproliferative effect of the curcumin analogue ASC-J9 delivered by PLGA nanoparticles against estrogen-dependent breast cancer

CHAPTER 2 Engineered gold nanoparticles targeted to mesenchymal cells from patients with bronchiolitis obliterans syndrome do not elicit inflammatory response and can be safely inhaled in rodents.

Abstract

A common feature of nanoparticles (NPs) is their large surface area to volume ratio that makes them an attractive tools for the development of drug delivery systems, improving several properties of “free” drugs: solubility, pharmacokinetic profile and biodistribution.

During my PhD, I studied different nanovehicles loaded with “free” hydrophobic drugs against two “over-proliferative” diseases to evaluate the efficacy and safety of nanodrugs.

Firstly, I focused my attention on the anti-proliferative effect of ASC-J9, a promise in the treatment of prostate cancer. ASC-J9 is a very hydrophobic molecule, which limits drug administration. ASC-J9 was loaded on PLGA NPs in order to improve the solubility of the molecule and applied to an estrogen-dependent breast cancer. My results showed a cellular growth inhibition associated with a specific G2/M cell cycle block, which led to apoptosis.

During the last years, I worked in collaboration with group of IRCCS San Matteo (PV). In a previous work (2015), Cova et al evaluated the effectiveness of gold NPs functionalized with anti-CD44 monoclonal antibody loaded with everolimus (GNP-HCe), prepared by our laboratory, in inhibiting mesenchymal cells (MCs), one of the major causes of bronchiolitis obliterans syndrome (BOS). Considering that BOS is due to an alteration of inflammatory process the aim is determined the effect of GNP-HCe on macrophages, neutrophils and lymphocytes with *in vitro* assays assessing cytokine secretion, cell apoptosis and ROS production. Next, we administered GNP-HCe by aerosolization in normal mice evaluating the localization and toxicity on lungs. GNP-HCe were able to reduce ROS and not to enhance the activity of three major components of immune response. The *in vivo* experiments confirmed that inhaled NPs did not raise the inflammatory response, because the bronchoalveolar lavage of mice did not show significant increase of IL-8 cytokine. This study discloses the possibility to plan a new pharmacological treatment for patients affected by pulmonary fibroproliferative disorders directly targeting MCs without altering the immune response.

The studies performed during my PhD thesis demonstrates that we were able to produce efficient NPs to vehicle different drugs in order to enhance their targeting and therapeutic effect, reducing side effects and complications in a future idea of therapy on human patients.

Introduction

I. Nanotechnology

Nanotechnology is a multidisciplinary scientific approach conducted at the nanoscale, preferentially within the 1 to 100 nanometers range. Chemists, biologists, physicists, material scientists and engineers share their knowledge to work at the molecular level and fabricate minute synthetic structures to improve the existing or gain totally new properties of matter. The applications of nanotechnology to disease treatment, diagnosis, monitoring and to the control of biological systems have recently been referred to as “nanomedicine” by the National Institutes of Health in USA.

Nano-objects have an extremely high surface area to volume ratio, therefore some of them are very reactive or catalytically active. The small size of these nanosystems, which can be design to have different compositions, confers unique chemical, physical and biological properties on them that can be used to overcome the limitations of molecular imaging and gene/drug delivery (Figure 1). Moreover, after the development of multifunctionalized nanoparticles, their applications in medicine are unprecedented.[1,2,3]

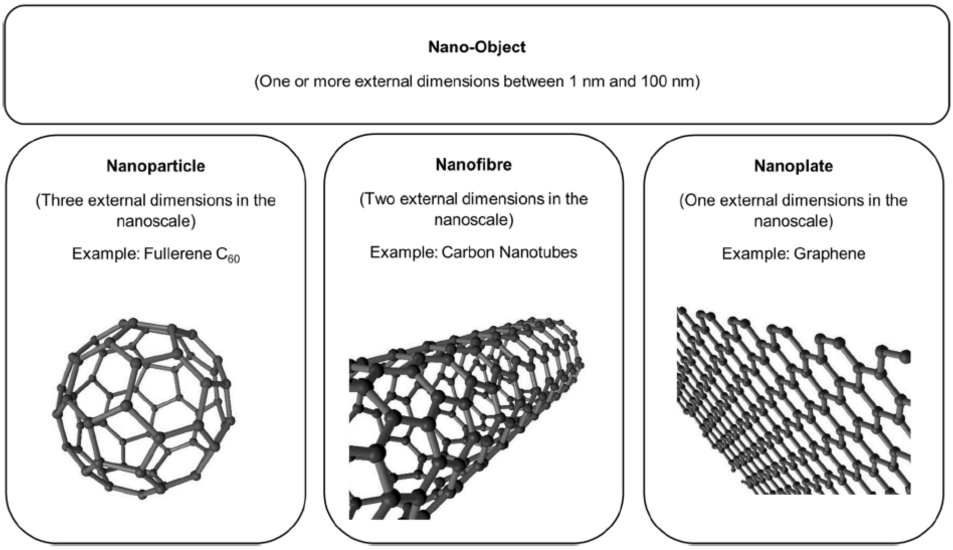

Figure 1. Nano-objects can be divided in nanoparticles, nanofibres and nanoplate depending on the number of external dimensions in the nanoscale.[3]

I.i Nanoparticles (NPs)

The studies of human diseases carried out so far have allowed researchers to understand that they originate from multiple biological alterations at molecular or nanoscale levels. For this reason, NPs formulations can be very useful to diagnose, monitor and treat human diseases, especially when overcoming the biological barriers is needed.

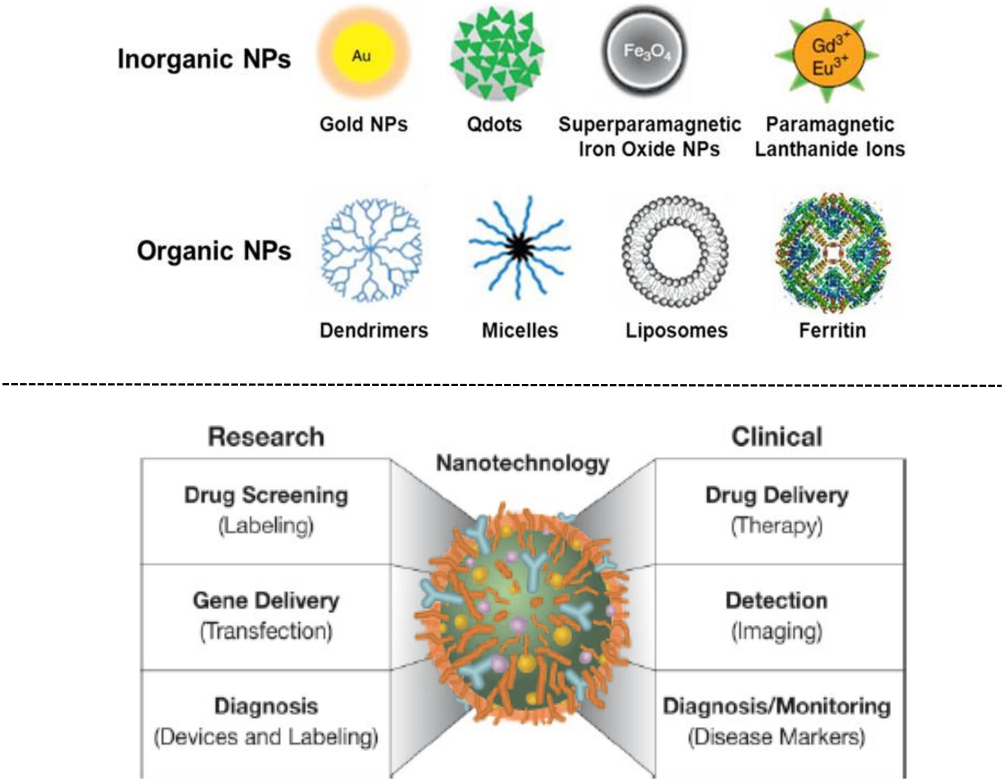

Figure 2. Schematic representation of typical nanocarriers and their possible applications in research and clinical. **Liposomes** contain amphiphilic molecules, which have hydrophobic and hydrophilic groups that self-assemble in water. **Dendrimers** are branched nanostructures; each terminus contains reactive chemical functional groups that allow the addition of multiple monomers to increase the size of the nanostructure. **Gold NPs** and **superparamagnetic Iron Oxide NPs** are solid metal particles that are conventionally coated with drug molecules, proteins, or oligonucleotides. **Quantum dots** are semiconductor nanocrystals endowed with strong photoluminescence usually consisting of a core-shell structure. **Ferritins** are protein assemblies with 4-8 nm interior cavities that provide a versatile, biocompatible platform for the synthesis and encapsulation of oxide and metal NPs or a wide range of molecules.[4-6]

NPs can be obtained from a variety of materials, but the most commonly used in nanomedicine are shown in Figure 2. Their unique size-dependent physicochemical properties allows for their use in various fields, from clinical diagnosis and detections of specific pathologies markers to therapy, such as drug target-therapy or gene delivery. Moreover, the surface of nanomaterials is usually coated with polymers or biorecognition molecules to achieve an improved biocompatibility and selective binding with biological molecules.[4,5]

A common feature of all NPs is their large surface area to volume ratio, which may be orders of magnitude greater than that of bulk materials. For example, cutting a 1 cm cube into 10^{21} cubes of 1 nm on a side, will result in the same overall volume and mass, but the surface area will be increased by a factor of 10 million. Thus, the advantage of using nanomaterials as carriers is that their surface can be coated with a large number of active molecules, which can be delivered using only small volumes of formulation allowing them to interact directly with cells through membrane receptors or entering passively without altering the behavior and biochemical properties of the molecular targets.[6]

I.ii Nanomaterials for in vivo investigation and in vitro diagnosis

A handful of nanomaterials are under investigation in clinical trials or have already been approved by the FDA for use in humans,[7,8,9] and several proof-of-concept studies of nanomaterials in cell culture and small animal models for medical applications are underway.[10,11,12] A number of these nanomaterials are designed to target tumors *in vivo* and are intended for use either as drug carriers or as contrast agents for molecular imaging.

Nanomaterials infused into the bloodstream can accumulate in tumors owing to the “enhanced permeability and retention” (EPR) effect, as the vasculature of immature tumors presents fenestrations with pores ranging from 200 to 600 nm, allowing for the extravasation of NPs from the blood into the tumor tissue (Figure 3).[11,13] The infusion of antineoplastic drugs exploiting nanomaterials as carriers results in an increased accumulation of drugs at the tumor, as compared with conventional administration.

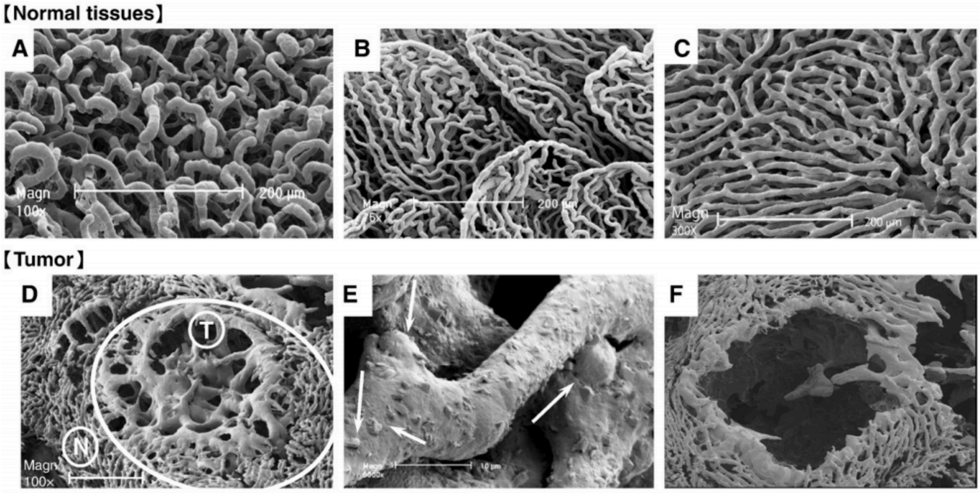

Figure 3. SEM images of blood vessels in various normal tissues (A–C) and metastatic liver tumors (D–F). Normal capillaries of the pancreas (A), colon (intestinal villi) (B), and liver (sinusoid) (C) are shown. (D) Metastatic tumor nodule (identified with T) in the liver, the normal liver tissue is indicated with "N." (E) Tumor vessels at the capillary level (larger magnification), with a rough surface. After i.v. injection of the macromolecular anticancer drug-loaded micelles, the tumor vascular bed (visible in D) was completely disintegrated, as shown by an empty void (F).[13]

In addition, the high ratio of surface area to volume favors high surface loading of therapeutic agents: when using organic nanomaterials, their hollow or porous core allows the encapsulation of hundreds to thousands of drug molecules within a single carrier NP. As the carrier degrades to some extent, the drug molecules are released and the rate of degradation can even be controlled and finely tuned according to the coating composition. These delivery nanovehicles can also be coated with polymers, such as polyethylene glycol (PEG), to increase their half-life in the blood circulation, to prevent opsonins from adhering to the nanomaterial surface, and reduce the rapid metabolism and clearance of the nanoparticulate. Moreover, the use of nanomaterials for drug delivery may minimize adverse effects by preventing the nonspecific uptake of therapeutic agents from healthy tissues. [4,12,14]

NPs are further attractive as sensitive contrast agents for cancer imaging. For instance, in magnetic NP-enhanced magnetic resonance imaging (MRI), a contrast can be observed between tissues having captured iron oxide NPs from those that did not incorporate, owing to a difference in the precession frequency of the water protons in proximity of paramagnetic nanodipoles. The use of magnetic NPs as contrast agents for MRI, as compared to conventional MRI, was associated with substantial increase in both diagnostic sensitivity (90.5% *vs*. 35.4%) and specificity (97.9% *vs*. 90.4%) in the detection of metastatic tumors.[15]

NPs can be also employed as labels for measuring molecules of interest in biological samples. To this aim, nanomaterials can be used to either simplify/amplify the readout or to lower substantially the detection threshold of a diagnostic device. NPs are used in lateral-flow *in vitro* diagnostic assays (LFA), such as the urine pregnancy test, for detecting protein markers (e.g., human chorionic gonadotropin [hCG]).[16] This allows an easier readout of the signal at the point of care without the need for a more complex instrumentation. A number of FDA-approved LFAs for measuring human immunodeficiency virus (HIV), malaria, and cardiac markers are also available. Although this technique is simple to use and can be carried out rapidly (one complete assay takes less than 1 h), it suffers from poor detection sensitivity (millimolar to micromolar, depending on the biomarker). Gold NPs are also used in high throughput genomic detection devices without the need for polymerase chain reaction (PCR) amplification but with sensitivity on the same order of that of PCR-based assays.[17] This technology has been approved by the FDA for genetic screening to determine drug sensitivity and to detect genetic mutations. This approach does not suffer from the problems often associated with conventional fluorescent probes for microarray labeling, such as photobleaching (a loss of signal after exposure to light), and can detect multiple markers with a high sensitivity (95%) and low detection threshold (down to 10^{-18} M). A modification of this approach called the bio-barcode assay is currently being validated for the detection of proteins associated with prostate cancer.[16]

I.iii Nanomaterials for theranostics

The term "theranostic" defines the combination of diagnostic and therapeutic capabilities into a single agent, and identifies the ongoing efforts in clinics to develop more specific and personalized therapies for various diseases.[18]

The rationale arose from the fact that several diseases are broadly heterogeneous and all existing treatments are effective for only limited patient subpopulations and at selective stages of disease development. The close marriage between diagnosis and therapy could provide therapeutic protocols that are more specific to individuals and, therefore, more likely to offer improved prognoses. The emergence of nanotechnology has offered an unprecedented opportunity to draw diagnosis and therapy closer.

NP-based imaging and therapy have been investigated separately, and their understanding has now evolved in nanoplatforms that can co-deliver therapeutic and imaging functions (Figure 4). These NPs possess unique optical or magnetic properties so that they have been previously studied in the imaging setting, and are now achieving successful outcomes under several circumstances.[19]

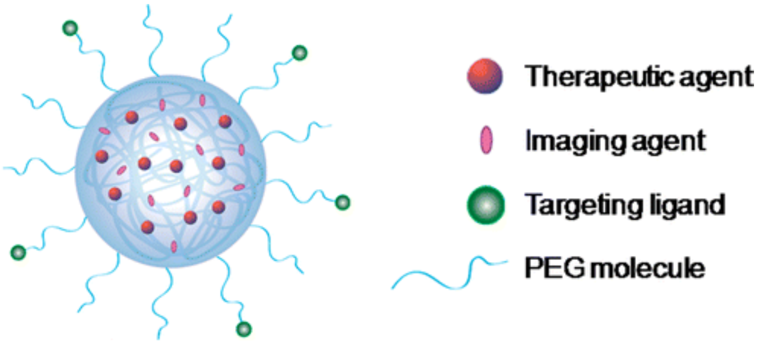

Figure 4. Example of nanotheranostic device. Nanotheranostics can deliver treatments while simultaneously monitoring therapy response in real-time, thereby decreasing the potential of over- or under-dosing patients.[20]

These have laid the foundations for the current applications, since the imaging probes can be easily upgraded when loaded with appropriate therapeutics. It has been shown that various kinds of therapeutics, including those based on small molecules, proteins and nucleotides can be conveniently tethered onto nanoplatforms. The large capacity even allows for the loading of a second or third functionality, a feature that encourages the formation of all-in-one nanosystems with comprehensive features.[19,20]

I.iv NPs as drug delivery systems

NPs are found to be attractive platforms for the delivery of increasingly potent, selective, and multifunctional anti-cancer drug conjugates.[20,21,22]

Drug delivery systems (DDSs) can improve several crucial properties of "free" drugs, such as solubility, *in vivo* stability, pharmacokinetics, and biodistribution, enhancing their efficacy. Moreover, NPs can provide effective carriers for biomolecules such as DNA, RNA, or proteins, protecting these materials from degradation and transporting them across the cell-membrane barrier. Colloidal NPs functionalized by tumor therapeutic agents such as paclitaxel,[21,22] anthracycline,[23] doxorubicin were proved to be efficiently delivered into cancer cells *in vitro* and *in vivo* studies.[24,25,26]

For a successful delivery, carriers must: (a) form condensed complexes with biomolecules, (b) improve plasma half-life and targeting efficiency compared to free drug, (c) facilitate penetration of the cell membrane after complexation, and (d) unload their payloads at the final destination (e.g., the target cell). To serve this purpose, two approaches, which can be either alternative or synergistic, are "passive" and "active" targeting. The passive targeting route takes advantage of the biological function of the reticuloendothelial system (RES), a cell family of the immune system comprising circulating monocytes, bone marrow progenitors and tissue macrophages, which are deputed to the first clearance activity in mammalian organisms. Once unprotected particles are immersed in the blood stream, an array of plasma proteins recognizes them as invading entities and immediately adsorb on their surface. The parameters affecting the extent of opsonization are essentially related to the physical properties of the NP surface, including size, shape, charge and aggregation state. Large objects are rapidly cleared and highly charged particles have a tendency to attract opsonins. Consequently, NPs coated by these plasma proteins are rapidly endocytosed by the RES cells, resulting in their removal from circulation and accumulation in organs with high phagocytic activity, such as liver and spleen.

Particle size is a key parameter as magnetic particles smaller than 400 nm accumulate in the liver (70-90%) and spleen (3-10%) quickly; particles in the range 100-200 nm had been shown that escape filtration by liver and spleen, while NPs below 5 nm can be cleared by renal route.[27,28,29] Therefore the optimal particle size for drug delivery treatments ranges between 10 to 100 nm, as these will have the longest blood circulation time. It has been suggested that also the shape can play a role.[30] Hence, passive nanocarriers can be used to deliver drugs for the treatment of hepatic diseases, such as liver metastases, and to favor the internalization of antibiotics by phagocytic cells of the RES for the treatment of intracellular infections. On the other hand, active targeting relies on specific recognition of the ligands that are displayed on delivery vehicles by cell surface receptors. The ligand used for active targeting can be a small molecule, or a peptide or protein.[31]

A key goal of DDSs is to discharge their payloads specifically at the diseased tissue. The release could be triggered by internal stimuli such as, in particular, glutathione (GSH), by pH, or by or external stimuli (e.g., light). Significantly, the internal stimuli operate in a biologically controlled manner, whereas the external stimuli provide spatial-temporal control over the release.[32]

II. Aim of the work

The aim of my PhD project was to take advantage of the multifaceted features characterizing nanomaterials in order to enhance the targeting and the therapeutic effect of three different hydrophobic drugs against two different "over-proliferative" diseases, namely breast cancer and chronic lung allograft dysfunction, according to the schematic summarized in Table 1.

Table 1. Summary of PhD project

NP	Drug	Pathology
PLGA NPs	ASC-J9	Estrogen-dependent breast cancer
GNPs	everolimus	Bronchiolitis obliterans syndrome

Therefore, the overall layout of my thesis includes two chapters, in which I have described in more details the pathology, the drug and the nanovehicle used.

Chapter 1: Poly(lactic-*co*-glycolic acid) (PLGA) NPs that are biodegradable copolymer nanovehicle consisting of oligomers of lactic acid and glycolic acid.

Chapter 2: Gold NPs (GNPs), belonging to the family of colloidal metal NPs, the most intensely studied nanomaterials due to their unique size-dependent electronic and optical properties, combined with a great potential in a broad range of biomedical applications.

III. References

---

[1] Liu Y. et al. Nanomedicine for drug delivery and imaging: a promising avenue for cancer therapy and diagnosis using targeted functional nanoparticles. *Int. J. Cancer.* 2007; 120: 2527-2537.

[2] Lim ZZ. et al. Gold Nanoparticles in cancer therapy. *Acta Pharmacol. Sin.* 2011; 32: 983-990.

[3] Xing Y. et al. Radiolabeled Nanoparticles for Multimodality Tumor Imaging. *Theranostics*. 2014, 4:290-306.

[4] McNeil SE. et al. Nanotechnology for the biologist. *J. Leuc. Biol*. 2005, 78: 585-594.

[5] Kim BY. et al. Nanomedicine. *N. Engl. J. Med.* 2010, 363: 2434-2443.

[6] Peer D. et al. Nanocarriers as an emerging platform for cancer therapy. *Nat. Nanotech*. 2007, 2: 751-760.

[7] McCarthy TD. et al. Dendrimers as drugs: discovery and preclinical and clinical development of dendrimer-based microbicides for HIV and STI prevention. *Mol. Pharm.* 2005, 2: 312-318.

[8] Davis ME. et al. Evidence of RNAi in humans from systemically administered siRNA via targeted nanoparticles. *Nature* 2010, 464: 1067-70.

[9] Liu Z. et al. Multiplex multicolor Raman imaging of live cells with isotipically modified single walled carbon nanotubes. *J. Am. Chem. Soc*. 2008, 130: 13540-13541.

[10] Hobbs SK. et al. Regulation of transport pathways in tumor vessels: role of tumor type and microenvironment. *Proc. Natl. Acad. Sci. U.S.A.* 1998, 95: 4607-4612.

[11] Prencipe G. et al. PEG branched polymer for functionalization of nanomaterials with ultralong blood circulation. *J. Am. Chem. Soc.* 2009, 131: 4783-4787.

---

[12] Fang J. et al. The EPR effect: Unique features of tumor blood vessels for drug delivery, factors involved, and limitations and augmentation of the effect. *Adv. Drug Deliv. Rev*. 2011, 63: 136–151.

[13] Alexis F. et al. Factors affecting the clearance and biodistribution of polymeric nanoparticles. *Mol. Pharm*. 2008, 5: 505- 515.

[14] Thaxton CS. et al. Nanoparticle-based bio-barcode assay redefines "undetectable" PSA and biochemical recurrence after radical prostatectomy. *Proc. Natl. Acad. Sci. U.S.A.* 2009, 106: 18437-18442.

[15] Postuma-Trumpie GA. et al. Lateral flow (immuno) assay: its strengths weaknesses, opportunities and threats: a literature survey. *Anal Bioanal. Chem.* 2009, 393: 569-582.

[16] Nam JM. et al. Nanoparticle-based bio-bar codes for the ultrasensitive detection of proteins. *Science.* 2003, 301: 1884-1886.

[17] Lammers T. et al. Theranostic nanomedicine. *Acc. Chem. Res.* 2011; 44: 1029-1038.

[18] Kim TH. et al. Nanotheranostics for personalized medicine. *Expert. Rev. Mol Diagn*. 2013; 13: 257–269.

[19] Craig GE. et al. Cisplatin tethered gold nanoparticles that exhibit enhanced reproducibility, drug loading, and stability: a step closer to pharmaceutical approval? *Inorg. Chem.* 2012; 51: 3490– 3497.

[20] Gibson JD. et al. Paclitaxel-functionalized gold nanoparticles. *J. Am. Chem. Soc.* 2007; 129: 11653–11661.

[21] Zhang XQ. et al. Strategy for increasing drug solubility and efficacy through covalent attachment to polyvalent DNAnanoparticle conjugates. *ACS Nano.* 2011; 5: 6962–6970.

[22] Ferrari M. Cancer nanotechnology: opportunities and challenges. *Nat. Rev. Cancer.* 200; 5: 161–171.

---

[23] You J. et al. Exceptionally high payload of doxorubicin in hollow gold nanospheres for near-infrared light-triggered drug release. *ACS Nano* 2010; 4: 1033- 1041.

[24] Wang F. et al. Doxorubicin tethered responsive gold nanoparticles facilitate intracellular drug delivery for overcoming multidrug resistance in cancer cells. *ACS Nano.* 2011; 5: 3679–3692.

[25] Park H. et al. Multifunctional nanoparticles for combined doxorubicin and photothermal treatments. *ACS Nano*. 2009; 3: 2919–2926.

[26] Zhang X. et al. Ultrasmall gold-doxorubicin conjugates rapidly kill apoptosis-resistant cancer cells. *Bioconjugate Chem*. 2011; 22: 235–243.

[27] Chomoucka J. et al. Magnetic nanoparticles and targeted drug delivering. *Pharmacol. Res.* 2010; 62: 144- 149.

[28] Longmire M. et al. Clearance Properties of Nano-sized Particles and Molecules as Imaging Agents: Considerations and Caveats. *Nanomedicine.* 2008; 3: 703-717.

[29] Blanco E. et al. Principle of nanoparticle designfor overcoming biological barriers to drug delivery. *Nature Biotech.* 2015; 33: 941-951.

[30] De M. et al. Applications of Nanoparticles in Biology. *Adv. Mater.* 2008; 20: 4225–4241.

[31] Ghosh P. et al. Gold nanoparticles in delivery applications. *Adv. Drug Deliv. Rev.* 2008; 60: 1307–1315.

[32] Pal SL. et al. Nanoparticle: An overview of preparation and characterization. *J. Applied Pharma. Science*. 2011; 6: 228-234.

Chapter 1

Antiproliferative effect of the curcumin analogue ASC-J9 delivered by PLGA nanoparticles against estrogen-dependent breast cancer cells

1.1 Introduction

1.1.1 Breast cancer

Breast cancer is the most frequent cancer in women. In Italy, estimated incidence and mortality until 2012 are 120 per 100,000 and 22.9 per 100,000, respectively.[1] However, it is worthwhile to notice that the mortality rate is decreasing 1.64%/year thanks to the early detection of cancer (clinical breast exams and mammography) and improvement in treatments.[2]

Breast cancer is a very heterogeneous disease, which lead to the development of different classification systems. The most important is based on a histological criteria (Figure 1.1), in this respect breast cancer are divided in *in situ* carcinomas, which don't spread outside the origin site, and invasive carcinomas.

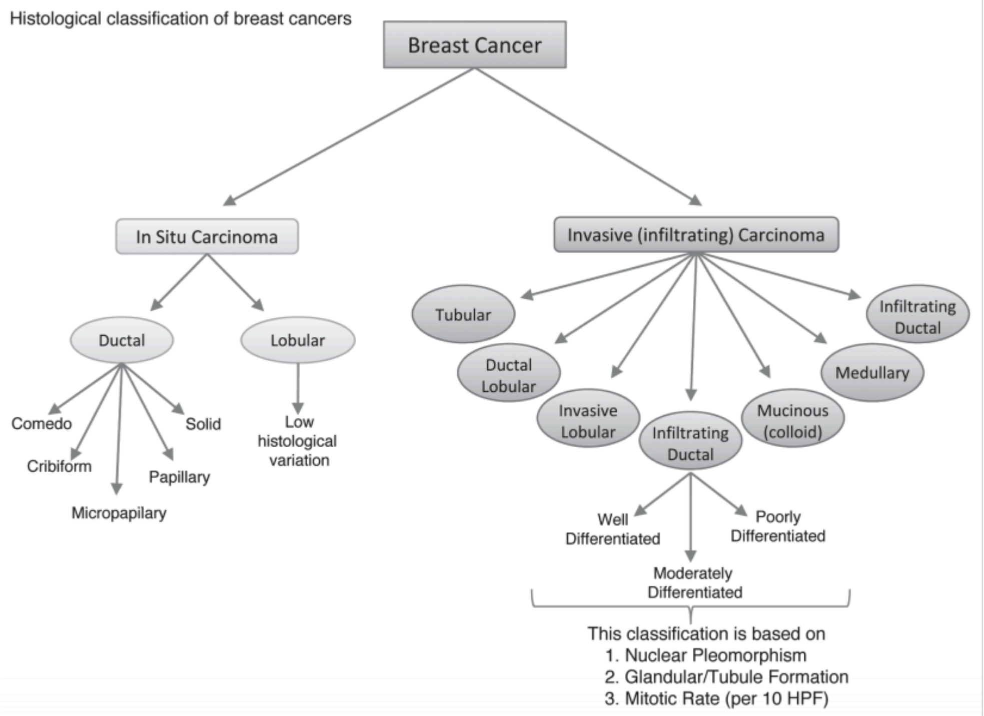

Figure 1.1 Histological classification of breast cancer subtypes.[3]

Another important classification in based on molecular markers, including estrogen receptor (ER), progesterone receptor (PR), and human epidermal growth factor receptor 2 (Her2), that can split breast cancer phenotype in different subtypes (Table 1).

Table 1. Molecular classification of breast cancers.[3,4]

Subtypes	Specific markers	Percentage
Basal-like Triple Negative	$ER^- PR^- Her2^-$ $EGFR^+$	15-20%
$Her2^+$	$Her2^+ ER^- PR^-$	10-15%
Luminal subtypes A	$ER^+ Her2^- PR^{low}$	40%
Luminal subtypes B	$ER^+ Her2^+ PR^{low}$	20%

The latter classification is primarily important to define the appropriate treatment for a patient, because every subtype has different prognosis and identifies specific targets for therapy. In particular, both luminal types are sensitive to endocrine therapies, including estrogen receptor antagonist (e.g. *tamoxifen*) and aromatase inhibitors (e.g. *Aromasin*®), and the Her2 group could be treated with the specific monoclonal antibody trastuzumab (*Herceptin*®, Roche) against the relevant overexpressed receptor.[3,4]

Despite remarkable progress in the treatment of breast cancer, patients frequently develop resistance to therapies through the alteration of different pathways that govern the survival of cancer, resulting in recurrences that exhibit increased aggressiveness and lower sensitivity to treatments.[5] For this reason, is important to achieve a better understanding of the mechanisms that initiate breast cancer and its progress in order to develop more specific and efficient therapies.

1.1.2 PLGA NPs in cancer treatment

Chemotherapy plays an important role in the clinical management of cancer, but the inaccessibility of several physiological targets and the adverse effects that limit the maximum tolerated dose have resulted in the development of alternative therapies. In particular, the development of NP formulations have attracted great attention offering enhanced sensitivity for *in vivo* tumor imaging, using currently available clinical imaging modalities and higher target-specific drug delivery.[6]

Among the nanocarriers, poly(lactic-co-glycolic acid) (PLGA) NPs have amazing potential in cancer treatment.

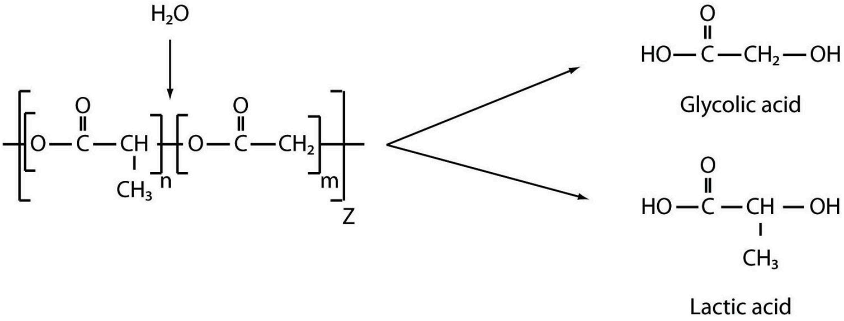

Figure 1.2. Chemical structure of poly(lactic-co-glycolic acid) and the hydrolysis of the polymer.[7]

PLGA is a copolymer consisting of multimer sequences of lactic acid and glycolic acid (Figure 1.2), making it a broadly useful and successfully biodegradable polymer for the development of nanoformulations for cancer treatment. By changing the ratio between lactic and glycolic acid, different forms of PLGA NPs with different degradation rate can be obtained. In this way, it is possible to control the release of the drug of interest and increase its bioavailability.[7]

Understanding the mechanism of biodegradation of PLGA NPs is fundamental for *in vitro* and *in vivo* studies. After several studies, it has been known that PLGA copolymers are degraded in the body by hydrophilic cleavage of the linkage between lactic and glycolic acid, and the main degradation mechanism involves the bulk erosion route rather than the surface erosion (Figure 1.3).[8]

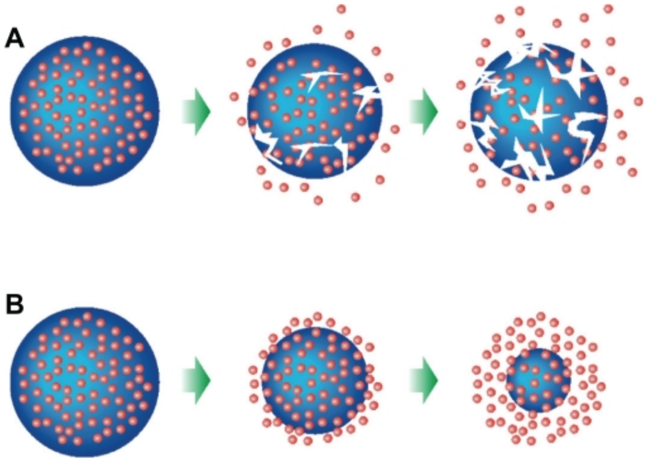

Figure 1.3. Degradation mechanisms of polymeric NPs: (A) bulk erosion and (B) surface erosion.[8]

Polymeric NPs can reach and accumulate at the tumor site thanks to the enhanced permeability and retention (EPR) effect, due to the presence of abnormal fenestrations in tumor vasculatures. However, the functionalization of PLGA NPs with targeting ligands allows the active targeting of nanocarriers to the final destination (e.g. specific cancer cells).[9]

The increasing experience in preparation, characterization and *in vivo* application of anticancer agents (e.g. Paclitaxel,[10,11] Docetaxel,[12] Doxorubicin[13] and Curcumin[14,15]) carried by PLGA NPs has provided the proof that these NPs are a very promising carriers for cancer treatment with higher efficacy and fewer side effects.

1.1.3 Aim of the work

In a recent work, we have demonstrated the potential activity of intracellular drug release from curcumin-loaded PLGA NPs in breast cancer cells, which resulted in tumor growth inhibition induced by the accumulation of cancer cells in G2/M phase of cell cycle.[16] The medical properties of curcumin, a natural product obtained from the rhizome of *Curcuma Longa*, spread into a broad range of pharmacological activities, including chemotherapeutic properties.[17,18] As a consequence, a number of curcumin analogues has been synthesized with the aim to improve the pharmacological profile of the natural product, as poor solubility combined with very low bioavailability limit its use in the clinical practice. These compounds have been further tested to investigate their activity against known and specific biological targets.[19]

Among the synthetic derivatives, in recent years, *in vivo* and *in vitro* studies have demonstrated that 1,7-bis(3,4-dimethoxyphenyl)-5-hydroxyhepta-1,4,6-trien-3-one, commonly referred to as ASC-J9, held great promise in the treatment of prostate cancer cells. ASC-J9 is able to bind the androgen receptor (AR) thus leading to a decrease in AR transactivation, resulting in the suppression of AR-mediated cell proliferation, angiogenesis and tumor growth.[20] In other works, ASC-J9 also showed effects on steroid receptors.[21] In addition, ASC-J9 has been suggested as a possible therapeutic agent for the treatment of AR-dependent neurodegenerative disorders. For example, the development of spinal and bulbar muscular atrophy (SBMA) is correlated to a motor neuron degeneration resulting from the aggregation of the AR with an expanded polyglutamine tract (AR-polyQ).

ASC-J9 possesses a chemical structure very similar to curcumin, but differs in the aromatic substituents, where the two hydroxyls that characterize curcumin, are completely methylated (Figure 1.4). This modification makes ASC-J9 extremely hydrophobic, and this hurdle limits its administration.

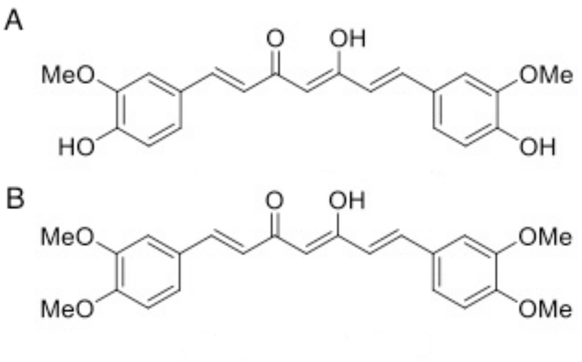

Figure 1.4. Chemical structure of (A) curcumin and (B) ASC-J9. The difference between the two molecules is the presence of two additional methylated hydroxyls in the ASC-J9 catechol rings.

Considering that aggressive breast cancer cell populations are generally estrogen-dependent (see Table 1), and based on the promising data collected from previous *in vitro* investigations on steroid receptor,[21] in the present work we developed ASC-J9-loaded PLGA nanocarriers in order to improve the drug solubility of the molecule investigating their effect on the growth inhibition of MCF-7 cells, an estrogen-dependent breast cancer cell line. In particular, we have characterized our nanoconstruct and evaluated the effects on the inhibition of cell proliferation induced by ASC-J9, triggering cell cycle arrest and eventually apoptosis.

1.2 Materials and methods

1.2.1 Reagents

50:50 PLGA (M_w = 45-60 kDa with an inherent viscosity of 0.59 dL g^{-1}), poly(vinyl alcohol) (PVA, M_w = 9-10 kDa, 80% hydrolyzed) were purchased from Sigma-Aldrich (St. Louis, MO) and used as received. Other chemicals and solvents were supplied by Sigma-Aldrich (St. Louis, MO), Fluka (St. Gallen, Switzerland), and Riedel-de Haen (Seelze, Germany) and used as received. Water was deionized and ultrafiltered by a Milli-Q apparatus (Millipore Corporation, Billerica, MA).

1.2.2 ASC-J9-loaded PLGA NPs (P-ASC-J9)

P-ASC-J9 were prepared using the "solvent-evaporation" process (also termed the single-emulsion process),[15,22] which is the gold standard technique for the encapsulation of hydrophobic compounds. The procedure of our standardized nanoformulation followed the same synthetic steps of the previously published preparation with curcumin.[15] The reagents used here were PLGA polymer (50 mg, 1 μmol) and freshly prepared ASC-J9 (5 mg, 12.5 μmol), corresponding to 10 wt% polymer. NP characterization, drug content evaluation, morphology, Raman spectroscopy, dynamic light scattering (DLS) distribution, ζ-potential, NP tracking analysis (NTA, NanoSight distribution), fluorescence analysis, and kinetics of drug release were evaluated following NP synthesis.

1.2.3 Drug loading and Encapsulation Efficiency (EE %)

UV-vis and fluorescence spectroscopy were used to determine the amount of drug encapsulated in P-ASC-J9. P-ASC-J9 powder (500 μg) was dispersed in water and mixed with a chloroform/ethanol solution 90:10. After stirring (3 h), the extracted ASC-J9 from NPs was determined in the organic phase by UV-vis

(424 nm) and fluorescence emission (λ_{ex} = 420 nm; λ_{em} = 522 nm). Pure PLGA and PVA did not interfere in the analysis of ASC-J9. The encapsulation efficiency was calculated using the equation 1:

Equation1:

$$EE\ (\%) = \frac{drug_{loaded}(\mu g_{drug} \cdot mg_{NPs}{}^{-1})}{drug_{initial}(\mu g_{drug} \cdot mg_{NPs}{}^{-1})} \times 100$$

UV-vis quantification was recorded using a Nanodrop 2000C spectrophotometer from Thermo Fisher Scientific (Wilmington, Germany). Fluorescence spectra were recorded using a Fluoromax-4P spectrofluorometer from Horiba Scientific (New Jersey, U.S.A.). The results of the experiments are expressed as the average of three different analysis.

1.2.4 Morphology

SEM images of NPs were obtained by a Zeiss EM-109 microscope (Oberkochen, Germany) operating at 80 kV. For the analysis, NPs were dispersed under sonication in water (5 μg mL^{-1}) and a drop of the resulting solution was placed on a Formvar/carbon-coated copper grid and air-dried.

1.2.5 Particle size and surface charge analysis

P-ASC-J9 and empty PLGA NPs (PNPs) were dispersed in the solvent with a final concentration of 5 μg mL^{-1}. DLS measurements were performed at 90° using Plus Particles Size Analyzer from Brookhaven Instrument Corporation (Holtsville, NY).

ζ-potential measurements were elaborated on the same instrument equipped with an AQ-809 electrode soaked in 10 mM NaCl aqueous solution (pH 7.25, σ = 14.2 mS cm^{-1}), and data were processed by Zeta-Plus software. Sight distribution spectra were collected (at 23 °C) by NanoSight LM10 from NanoSight Limited (Amesbury, U.K.) and analyzed with NTA software.

1.2.6 Fluorescence stability analysis of encapsulated drug

Fluorescence emission of free and encapsulated ASC-J9 was recorded in the range 490 to 700 nm (λ_{ex} = 420 nm). Buffers used: 20 mM acetate (pH 4.75), 20 mM phosphate (pH 7.40), 20 mM ammonium (pH 9.25), and cell culture Dulbecco's Modified Eagle Medium (DMEM, pH 7.40). Free ASC-J9 (5 mM in DMSO stock solution) was diluted in all buffers at a final concentration of 5 μM; P-ASC-J9 were dispersed directly in the medium so as to achieve the same average drug concentration. Equal amounts of empty PNPs did not interfere in the analysis.

1.2.7 *In vitro* drug release profiles

In vitro ASC-J9 release from PLGA NPs was evaluated by the dissolution technique.[15] ASC-J9 release was performed at 37 °C in all buffers used for fluorescence analysis (from acid to alkaline pH), supplemented with 2 wt % bovine serum albumin (BSA) to mimic a biological environment and enhance drug dissolution in these solvents. Maximum drug solubility was preliminarily estimated in order to calculate the necessary amount of solvent to perform kinetics under *sink* conditions.[23] Briefly, in the respective buffer was kept a nanoparticulate dispersion of P-ASC-J9 (1 mg mL^{-1}) under mild stirring at 37 °C in a closed container, to prevent evaporation of the solvent. Samples (1 mL) were withdrawn at regular time intervals, and NPs were separated from the supernatant by centrifugation (8000 g). The nanoparticulate deposit was resuspended in fresh buffer (1 mL) and replaced in the kinetic batch. Every 24 h all the solvent was completely replaced with fresh buffer. After centrifugation, solubilized ASC-J9 in each particle-free supernatant was analyzed spectrophotometrically at 424 nm.

All kinetic measurements were performed in triplicate, and the average values were taken ± standard deviations. The kinetic analysis of the release data was elaborated using the Peppas-Korsmeyer model (equation 2):

$$f_t = kt^n$$

$$log f_t = \log k + n \cdot \log(t) \qquad \text{(eq 2)}$$

where f_t is the fractional amount of drug released, k is the release constant, n is the release exponent and t is the time of release.
To determine the exponent (n), we investigated the linear tract of the kinetic curve until the fractional released amount reached 70%.

1.2.8 Raman spectroscopy

The Raman analysis of free ASC-J9, P-ASC-J9 and PNPs were performed using Aramis Horiba Jobin-Yvon micro-Raman spectrometer equipped with a HeNe laser operating at 633 nm and a solid state near-infrared laser operating at 785 nm. Briefly, a small amount of powder of each nanoparticulate was deposited on a silica slide and measured without other manipulation of the sample. Spectra were collected using 785 nm laser line with an output power of 50 mW focused on the sample through a 10X objective. Data were obtained averaging 3 different measurements of 20 s each.

1.2.9 Cell cultures and *in vitro* experiments

MCF-7 human breast cancer cells were maintained in 50% DMEM and 50% Ham's F-12 medium supplemented with 10% fetal bovine serum (FBS), L-glutamine (2 mM), penicillin (50 UI mL^{-1}) and streptomycin (50 mg mL^{-1}). 3T3-L1 mouse embryonic fibroblasts were maintained in the same medium of MCF-7 with exception of Ham's F-12 medium. Both cell lines were grown at 37 °C with 5% of CO_2. Cell culture medium, supplements and antibiotics were purchased from EuroClone.

For each *in vitro* test, P-ASC-J9 or PNPs were resuspended in complete culture medium to a final concentration of 5 μM, 10 μM and 20 μM. Stock solutions of free ASC-J9 (5 mM) were diluted with culture medium to get the same amount of drug carried by P-ASC-J9.

1.2.10 Cell viability

To test P-ASC-J9 or PNPs toxicity, 3-(4,5-Dimethylthiazol-2-yl)-2,5-Diphenyltetrazolium Bromide (MTT) assay was performed. MCF-7 and 3T3-L1 were seeded (5×10^3 cells per well) in a 96-well plate and grown for 24 h. The cells were then treated with different concentrations (5, 10 and 20 μM) of PNPs, free ASC-J9 and P-ASC-J9, referring to the quantity of ASC-J9. After 24, 48 and 72 h of exposure at 37 °C, the cell viability was monitored according to the manufacturer's inctructions (CellTiter 96 Non-radioactive Cell Proliferation Assay, Promega), and absorbance of formazan products were read immediately by ELISA plate reader at λ = 570 nm and as wavelength reference of 620 nm.

The results are expressed as means ± standard deviation (SD) of three individual experiments for each cell line.

1.2.11 Apoptotic cell death analysis

MCF-7 cells were seeded in a 6-well plate at a concentration of 1.5×10^5 cells per well and were grown for 24 h. Then cells were incubated for 3 and 24 h at 37 °C with 5, 10 and 20 μM of PNPs, free ASC-J9 and P-ASC-J9. After exposure, floating cells were collected in flow cytometry tubes, adherent cells were washed twice with phosphate buffer solution (PBS), trypsinized and collected in the respectively FACS tubes. All collected cells were treated for flow cytometry analysis according to Annexin-V-PE-Cy5 Apoptosis detection kit (BioVision Inc.).

Sample acquisition (at least 20 thousand events) was performed by FACS Calibur flow cytometer (Becton Dickinson - BD) and analyzed by CellQuest Pro Software (BD).

1.2.12 Cell cycle analysis

MCF-7 cells were seeded in a 6-well plate (10^5 cells per well) and after 24 h were incubated with 5, 10 and 20 μM free ASC-J9 and P-ASC-J9 for 24, 48 and 72 h at 37 °C. Once collected and fixed (70% ethanol), cellular DNA was stained at 4 °C with a mixture of propidium iodide (10 μg mL^{-1}) and RNase A (18 μg mL^{-1}).

Sample acquisition was performed using flow cytometry equipped with a doublet discriminator module (FACS Calibur; BD, San Jose, CA, U.S.A.), and the DNA content was analyzed by FlowJo software (TreeStar Inc., OR, U.S.A.).

1.2.13 Radical scavenging efficiency

2,2-Diphenyl-2-picrylhy-drazyl (DPPH) was used as the source of free radicals.[24] Stock solution of free ASC-J9 (5 mM in DMSO) was further diluted to reach the same amount of drug in the nanoformulation. PNPs and P-ASC-J9 corresponding to 10 μM drug content were resuspended in 4 mL of water and used for the analysis. To the aqueous reaction mixture, a methanolic solution of DPPH (5 mM) was added to reach a final concentration of 100 μM DPPH; dark colored solutions were kept in the dark at 37 °C for 1, 4, 8, 24 and 48 h.

For each time, the scavenging activity was determined spectrophotometrically at 520 nm against untreated DPPH solution as control. All results correspond to ± standard deviation (SD) of 5 individual readings for each sample. The antioxidant activity was calculated (eq 3) as percentage of DPPH that was decreased in comparison with the untreated sample (100%):

$$antioxidant\ activity\ (\%) = \frac{Abs_{untreated} - Abs_{treated}}{Abs_{untreated}} \times 100 \quad \text{(eq3)}$$

1.2.14 Measurement of intracellular level of Reactive Oxygen Species (ROS)

ROS were measured using 2',7'–dichlorofluorescein diacetate (DCFDA) Cellular ROS detection assay kit (Abcam – Mitosciences), according to the manufacturer's instruction. MCF-7 cells were seeded in a 96-well plate at a concentration of 5×10^3 cells per well and grown for 24 h. Then, cells were washed with the supplied buffer, followed by incubation of 100 μL $well^{-1}$ of DCFDA (25 μM) for 45 minutes at 37 °C. Next, cells were incubated with PNPs, free ASC-J9 and P-ASC-J9 at a drug concentration corresponding to 5, 10 and 20 μM for 15 min, 1, 4 h at 37 °C. Untreated cells were used as a negative control. Fluorescence was measured in triplicate by Fluoromax-4P spectrofluorometer (λ_{ex} = 485 nm; λ_{em} = 535 nm).

1.2.15 Confocal laser scanning microscopy

Cells were grown on a coverslip in a 6-well plate (10^5 cells), and the same experimental procedure for flow cytometry analysis was performed. Images were obtained with Leica DM IRE2 confocal microscope equipped with argon/krypton laser to excite coumarin-6 at λ = 488 nm. At least 5 fields per each sample of two biological replicates were taken.

1.2.16 Raman imaging

1.5×10^5 cells were seeded on poly-lysine coated CaF_2 disks used as optical substrate, grown 24 h, and incubated with 5 μM PNPs and 20 μM P-ASC-J9 for 24 h at 37 °C. Untreated cells were tested as a negative control. Cells were then washed with PBS and fixed for 30 min at 37 °C with 2% paraformaldehyde in PBS solution.

Raman imaging was performed using the same micro-Raman spectrometer of Raman spectroscopy analysis (2.8) utilizing the HeNe, 633 nm laser (power 20 mW), coupled with an immersion objective (63X/1.0 NA). Each cell was scanned with a step size of 700 nm over the entire cell area, for 1 s × 3 repetitions for each step, with the laser focused at 3.5 μm above the CaF_2 surface. The resulting Raman mapping images were then processed (spectral noise removal, baseline correction, unvaried imaging, RGB images manipulation, CLS (classical least squares) matching by using LabSpec6 (HORIBA scientific).

1.2.17 Statistical analysis

All biological data are expressed as mean ± SD. Data were analyzed by Student's *t*-test. Post hoc analysis was carried out when statistical significance, $P < 0.05$ (*), $P < 0.01$ (**) and $P < 0.001$ (***) was detected.

1.3 Results and Discussion

1.3.1 Preparation and characterization of P-ASC-J9 nanoformulation

Curcumin has been recently one of the most studied compounds among natural products because of its involvement in several bioactivities.[25] For this reason, a few analogues have been developed with the aim to increase both specificity and therapeutic action. In this work, we have focused our attention on the nanoformulation of a relatively new curcumin analogue, termed ASC-J9, possessing enhanced hormonal inhibitory activity against prostate cancer,[19,20] with the aim to test its efficacy against estrogen receptor-positive breast cancer cells (MCF-7 cell line) given the capability of ASC-J9 to interact with steroid receptors.

In order to encapsulate ASC-J9 inside the polymer matrix of PLGA NPs, the "single-emulsion" technique was picked out as the most accurate method for the preparation of water-dispersible P-ASC-J9 and the corresponding drug-free NP system, PNPs. This technique is the ideal method for the encapsulation of hydrophobic molecules and, at the same time, allows the best performances to obtain encapsulation efficiency together with homogeneous particle size distribution. During the formation of NPs, water-soluble PVA (5.0 and 0.3 wt %) is added to the emulsion as a surfactant to homogenize and stabilize the suspension, avoiding undesired NP agglomeration. Electron Microscopy (Transmission EM and Scanning EM) analysis of P-ASC-J9 showed that spherical NPs with diameter of 110 ± 14 nm were generated (Figure 1.5A). Mean size distribution recorded by NTA confirmed a NP size with a maximum in intensity of 131 ± 25 nm, with only a bigger subpopulation at 192 nm (Figure 1.5B). Analysis of PNPs was consistent with our previous reports.[15]

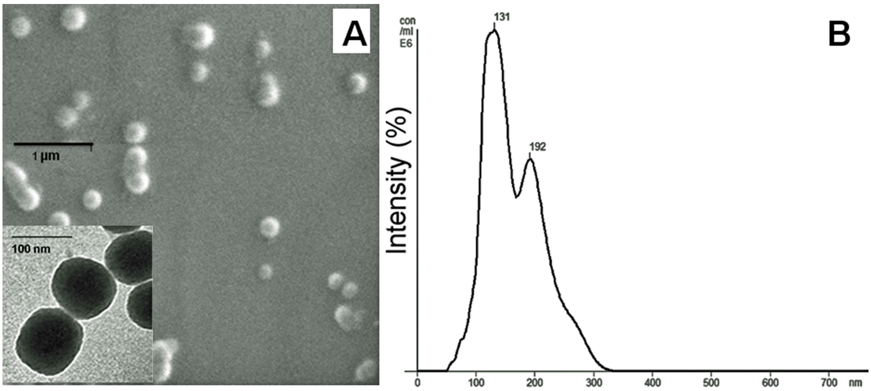

Figure 1.5. (A) SEM image (Inset: TEM magnification) of synthetized P-ASC-J9. (B) Nanosight distribution in deionized water of P-ASC-J9.

By DLS performed in 20 mM PBS at pH 7.2, we analyzed NPs suspension behavior in aqueous solution directly from the resuspension of the crude powder after lyophilization. From DLS analysis, the measured hydrodynamic diameters of P-ASC-J9 and PNPs were 145.6 ± 22 nm (PDI, 0.115) and 171.5 ± 15 nm (PDI, 0.095), respectively, showing a good particulate dispersion in the physiological milieu. In addition, the surface charges of P-ASC-J9 (−18.7 ± 2.9 mV) and PNPs (–21.4 ± 3.1 mV) were analyzed by ζ-potential in 1 mM NaCl solution at pH 7.2 and further through a pH titration from alkaline to acidic environment (pH range: 3-9, Figure 1.6. Both NP systems are strongly negatively charged in a broad pH range (4-9), except for pH 3, where the external carboxyl groups of PLGA are likely to be protonated.

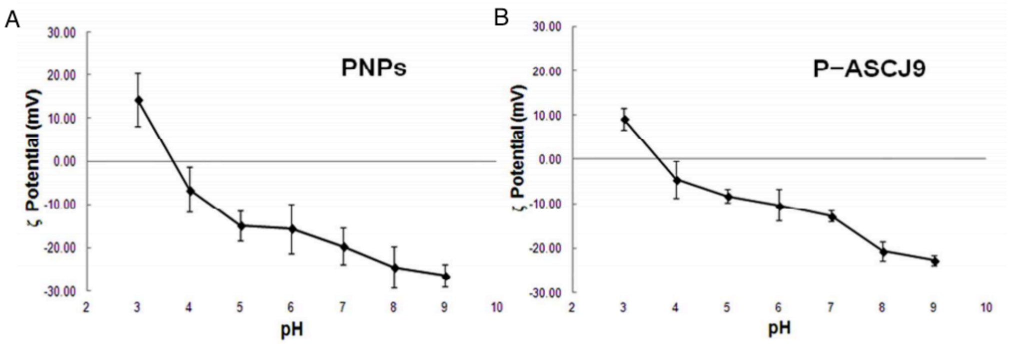

Figure 1.6. ζ-potential titration. NPs are suspended in 10 mM NaOH solution, pH 9 and the concentration of PNPs (A) or P-ASC-J9 (B) were 5 μg mL^{-1}. The titration profile from alkaline to acidic was monitored by dropwise addition of 0.1 N HCl; at fixed pH intervals, samples were withdrawn from the whole mixture and analyzed. All measures were performed in triplicate and the average values were taken.

Next, we assessed the propensity of our NP formulation to protect the incorporated drug from the external environment. For instance, our primary purpose was to evaluate if the synthetic process was suitable to gain a nanoformulation without altering the structural features of ASC-J9, which exploits its pharmacological activity. In addition, the maintenance of the polymer matrix plays a critical role avoiding drug degradation by the external environment until the nanocarrier reaches the target site of action.

Since curcumin and most of its analogues possess a green fluorescence emission under appropriate excitation wavelengths, a set of fluorescence analyses were performed (Figure 1.7) under physiological conditions, aiming to demonstrate the behavior of encapsulated ASC-J9 in terms of chemical properties inside the polymer matrix.

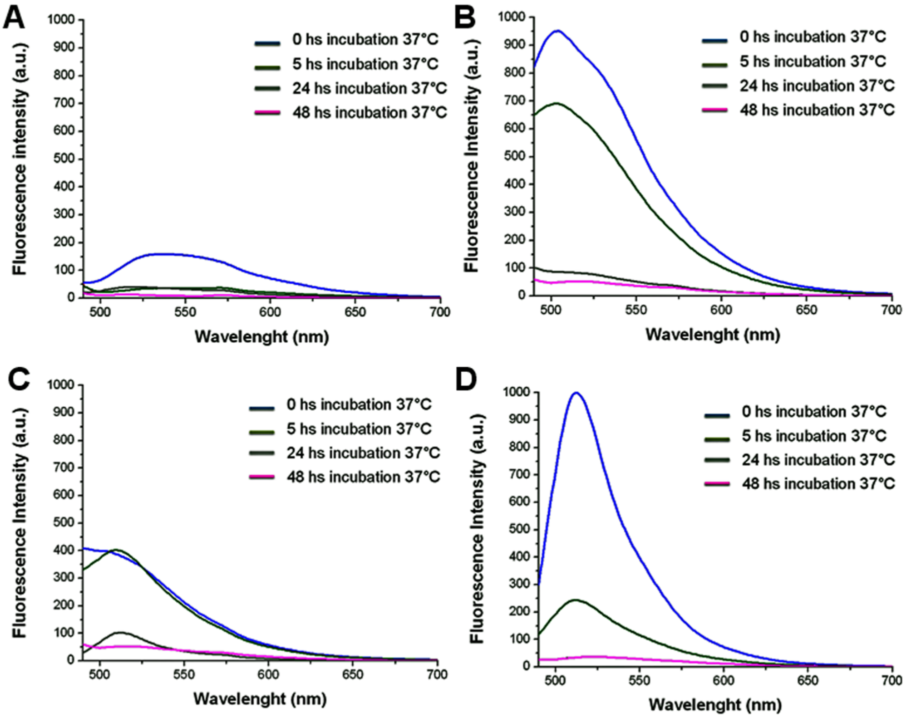

Figure 1.7. Drug structure preservation from external environment in biological milieu. Fluorescence emission spectra of 5 μM ASC-J9 (A,C) and equal amount of P–ASC-J9 (B,D) until 48 h of incubation at 37 °C. Blue line = time zero; green line = 5 h; grey line = 24 h; pink line = 48 h. Excitation wavelength was fixed at 420 nm for all measures.

This experiment was performed in 20 mM PBS, pH 7.4 (Figure 1.7A and B), and DMEM containing 10 wt.% serum, pH 7.4 (Figure 1.7C and D), checking the overall green fluorescence intensity up to 48 h of incubation at 37 °C.

At first glance, higher fluorescence intensities of P–ASC-J9 were detected in comparison with free drug in both solvents, showing broad fluorescence peaks, which became increasingly lower over time. We preliminarily excited PNPs at the same wavelength of other samples in order to check if empty NPs could interfere with the analysis. The same type of analysis was performed in other buffers commonly used in clinical treatments, to verify the maintenance of the polymer shell at acid and/or alkaline pHs for the whole time of incubation used previously (Figure 1.8). It is worth noting that similar behaviors were retained in the whole pH range, suggesting that our formulation was able to efficiently maintain its protective features up to 24 h of dissolution. However, later on, the polymer matrix began to destabilize, increasing drug exposure to the external environment.

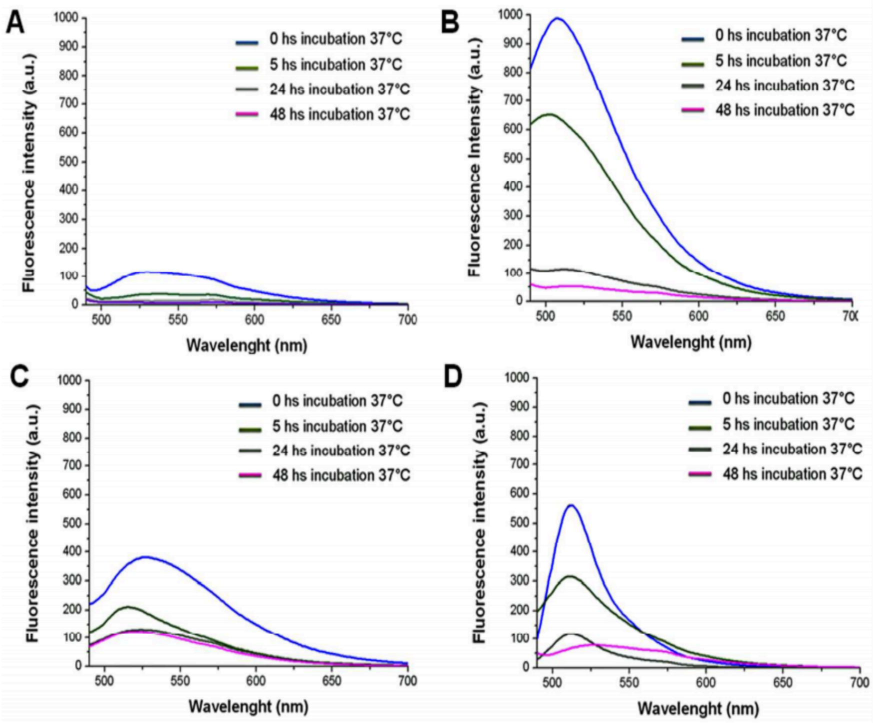

Figure 1.8. Fluorescence stability analysis. (A) 5 µM ASC-J9 solution in 20 mM acetate buffer, pH 4.75, compared with (B) P–ASC-J9 at the same drug concentration. (C) 5 µM ASC-J9 solution in 20 mM ammonium buffer, pH 9.25, compared with (D) P–ASC-J9 at the same drug concentration. Samples were excited at a fixed excitation wavelength of 420 nm and the emission spectra were recorded in the wavelength range 490-700 nm. The slit widths (for controlling magnitude and resolution of transmitted light) were standardized at 3 nm for both excitation and emission wavelengths.

Fluorescence results prompted us to apply Raman spectroscopy to confirm that ASC-J9 structure did not undergo alteration after encapsulation. Raman spectra of free ASC-J9, P–ASC-J9 and PNP were performed in order to confirm the encapsulation and the structural integrity of ACS-J9 inside PLGA. The Raman spectrum of P–ASC-J9 (Figure 1.9B) is basically given by the sum of the peaks present in the spectra of the ASC-J9 (Figure 1.9A) and of the empty PLGA

NPs (Figure 1.9C) with minor shifts. In particular, peaks at 1597 cm^{-1} and at 1635 cm^{-1} relative to the C=C aromatic stretching and to the C=O stretching, respectively, as well as the peak at 1158 cm^{-1} assigned to the C−OH stretching of ASC-J9, appear to be well conserved in the P−ASC-J9 spectra, suggesting that the molecule maintains its preference for the enolic conformation even when it is encapsulated in the polymer.

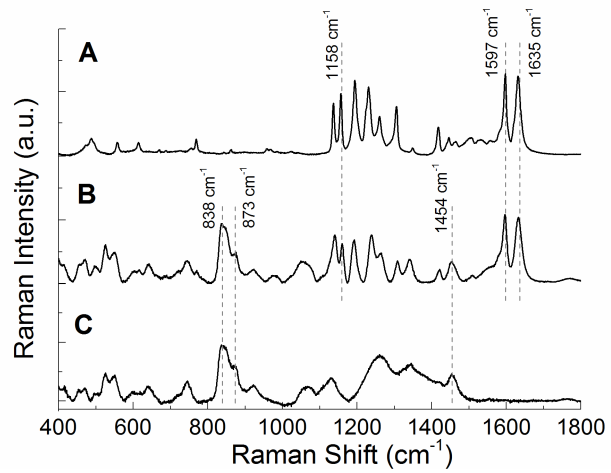

Figure 1.9. Raman spectra of (A) free ASC-J9, (B) P−ASC-J9, and (C) PNPs. The most distinctive peaks of ASC-J9 and PLGA are indicated by the dashed lines and compared with the spectra of the encapsulated drug.

Several computational chemistry works have confirmed that, in curcumin compounds, the energy of the enol form is 6.7 kcal mol^{-1} lower than the diketone tautomer.[26] There are several factors that likely contribute to this effect, including (i) the acidic nature of the protons on the central methylene carbon, (ii) the stabilization of the enol form via an intramolecular hydrogen bond, and (iii) the establishment of a fully conjugated system. This prediction was corroborated by X-ray crystal structures and more recently by NMR analysis of the solution structure of curcumin,[27] in which the compound existed solely in the enol form.

In the spectra of the encapsulated drug (Figure 1.9B), is even possible to recognize some of the bands relative to the lactic units of the polymer at 873 cm^{-1}

(relative to the C–COO stretching) and at 1454 cm^{-1} ($-CH_3$ asymmetric bending), and of the glycolic units at 838 cm^{-1} ($-CH_2$ rocking) as reported in a previous study.[28]

In this way we could demonstrate that P–ASC-J9 were able to efficiently encapsulate the drug, whereby the polymer matrix was able to protect ASC-J9 from the external environment. In addition, our study validates that the nanoencapsulation does not alter its chemical structure, which should be the optimal condition for drug activity.

1.3.2 *In vitro* drug release kinetics

Release kinetics is a fundamental study, which offers a plethora of information about drug diffusion timing and critical implications about the porosity of nanoformulations at the molecular level. Moreover, it allows researchers to find possible interactions between the drug–environment interface and the polymer matrix, which should affect the mechanism and rate of future sustained delivery *in vivo*.

We first estimated the amount of ASC-J9 in terms of loading capability of the PLGA nanosystem. A calibration curve in a mixture of vol.% 90:10 chloroform/ethanol of ASC-J9 was prepared for the analysis. Briefly, P–ASC-J9 were dispersed in aqueous solution and mixed with the organic chlorinated phase and incubated for 3 h, which is the time required to dissolve the drug in the organic solvent. ASC-J9 was detected by UV-vis and fluorescence spectroscopies. Drug loading, calculated by wt % difference, revealed that 65 ± 3 μg of drug for each mg of PLGA NPs (6.5 wt % of the polymer) was encapsulated. The initial amount of ASC-J9 was 10.0 wt %, so we achieved an average of 65% encapsulation efficiency into the polymer matrix (Equation 1).

After the estimation of drug loading, we tried to carefully determine the maximum solubility of ASC-J9 under all conditions previously tested for fluorescence studies (Figure 1.10). For instance, kinetic studies were performed in acidic acetate buffer, physiological phosphate buffer and alkaline ammonium buffer, each medium being supplemented with 2.0 wt.% bovine serum albumin (BSA) to increase ASC-J9 release, taking into account its strong hydrophobicity. Advisable to employ *sink* conditions during *in vitro* testing, the maximum solubility calculation allowed us to predict the smallest volume of media that could be used to ensure drug solubility maintaining *sink* conditions and preventing accumulation of polymer degradation products.

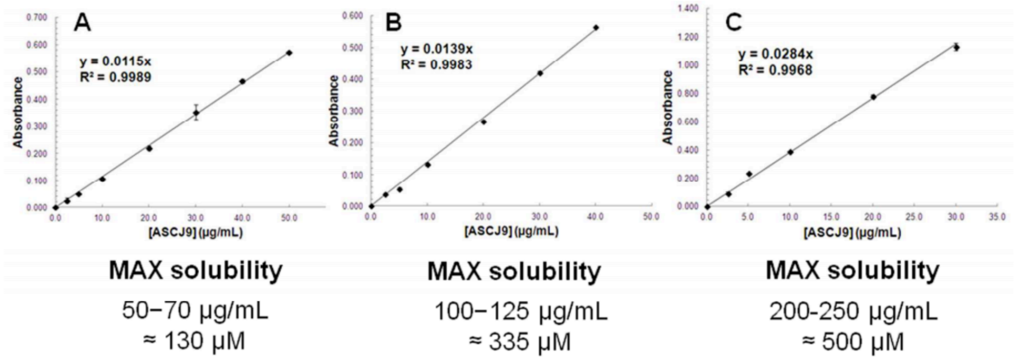

Figure 1.10. Estimation of maximum drug solubility in different buffer solutions. Maximum dissolution profile in (A) acetate buffer, pH 4.75; in (B) phosphate buffer, pH 7.40; in (C) ammonium buffer, pH 9.25.

Based on these calculations, our release study was performed at 37 °C in 20 mM PBS containing P−ASC-J9 suspension (Figure 1.11). Small amounts of sample were withdrawn at fixed times, and the NPs were separated by the supernatant; the sediment was redispersed in the same volume of fresh buffer and quickly replaced into the reactor. We observed an initial burst release during the first 8 h of incubation (75.3 ± 6.5%) and within the following 48 h this value rose to 92.1 ± 2.0%. Finally, the kinetics reached a plateau corresponding to a maximum after 3-4 days (very close to 100%), suggesting a continuous and prolonged release by our nanocarrier (Figure 1.11A). Kinetic elaboration was fitted according to the Korsmeyer–Peppas model.[29] We observed that the fractional amount of drug release log f_t versus log t was found to be 0.983. Meanwhile, the release exponent (n) and the release constant (k) were estimated around 0.517 and 0.619, respectively (Figure 1.11B). From this calculation, we could approximate that ASC-J9 release from our nanoconstruct followed a Fickian−law diffusion with a release exponent of 0.51.

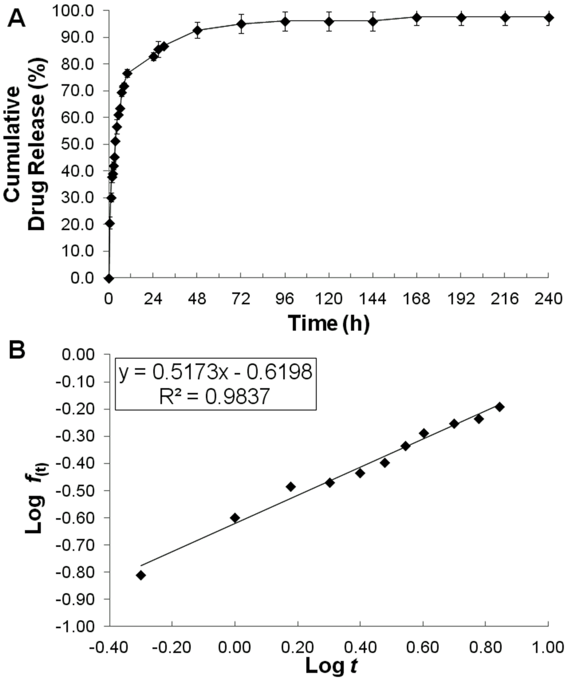

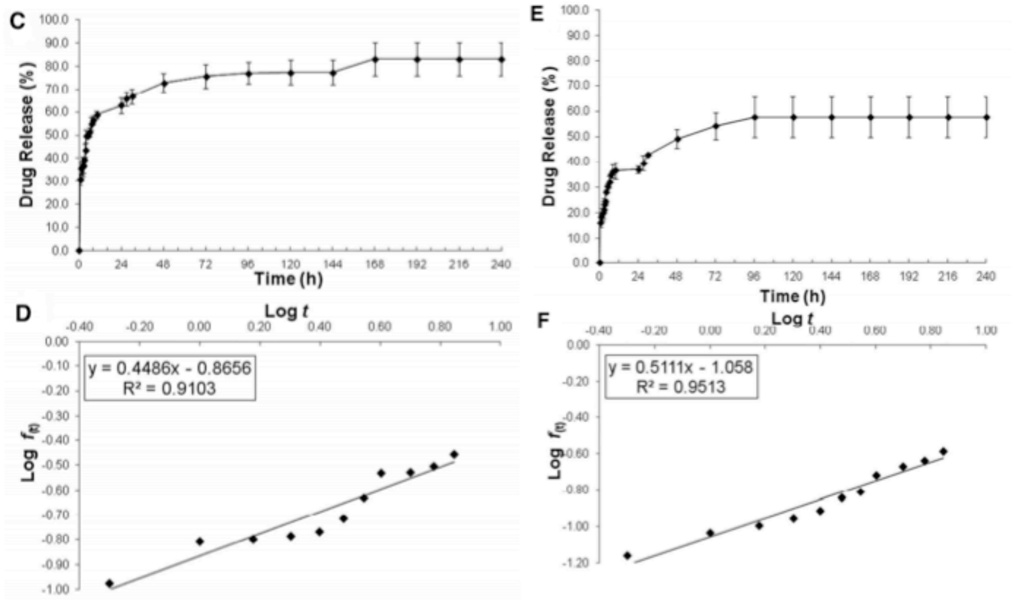

Figure 1.11. *In vitro* ASC-J9 release kinetics under different conditions. ASC-J9 dissolution profile from P–ASC-J9 using the dissolution technique in (A-B) 20 mM PBS (pH 7.4, supplemented with 2.0 wt % BSA), (C-D) in 20 mM acetate buffer (pH 4.75) and (E-F) in 20 mM ammonium buffer (pH 9.25). Values represent the average ± SD of three independent batches. (B, D and F) Elaboration of the kinetic rate keeping in consideration the Peppas–Korsmeyer model.

The same experiment was repeated in an acidic 20 mM acetate buffer (pH 4.75, supplemented with 2.0 wt % BSA, Figure 1.11C) and an alkaline 20 mM ammonium buffer (pH 9.25, supplemented with 2.0 wt % BSA, Figure 1.11E). Basically, the ASC-J9 release in acidic condition followed the same Fickian–law diffusion with a release exponent of 0.45 (Figure 1.11D). However, the lower solubility of the drug in this buffer reduced the overall release, which reached only a maximum level of 83.1 ± 3.2% within 4-5 days. On the contrary, despite the higher solubility ratio of ASC-J9 under alkaline conditions, the cargo release in ammonium buffer was drastically reduced, reaching a maximum of 59.0 ± 1.5%. This behavior should be correlated with the degradation of curcuminoids under alkaline conditions, where their hydrolytic degradation was decreased by the formation of several byproducts as reported in the literature.[30,31]

1.3.3 Internalization of P-ASC-J9 in MCF-7 cells

Next, we checked the propensity of our nanoformulation to be internalized into the cellular environment. To this aim, PNPs were first loaded with hydrophobic coumarin-6 and confocal laser scanning microscopy images were acquired to follow the time-dependent compartmentalization inside the cells (Figure 1.12). In this experiment, ASC-J9 was initially replaced by this dye because ASC-J9 exhibits a poor fluorescent intensity *in vitro* and the poor resolution of related images did not allow us to obtain a sufficient outcome. Figure 1.12 shows how there was a mild signal of NPs internalization in MCF-7 cells after 4 h which increase up to 48 h of treatment.

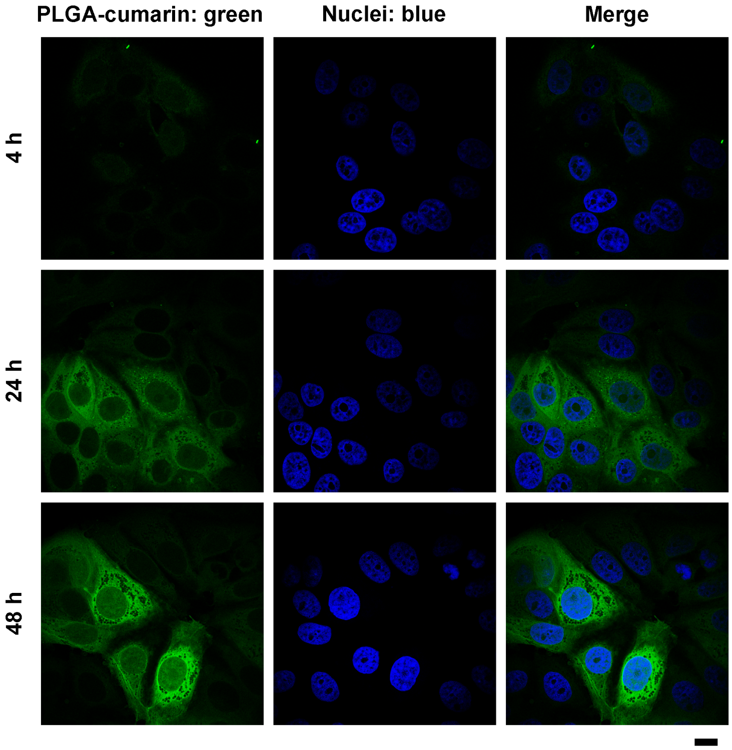

Figure 1.12. Confocal microscopy analysis. MCF-7 were grown on coverslips for 24 h and then exposed to 20 µM PLGA-coumarin-6 for 4, 24 and 48 h at 37 °C. Nuclei were stained with DAPI (blue). Scale bar = 10 µm.

To better verify the cellular internalization of P–ASC-J9, we took advantage of the typical Raman spectra of ASC-J9 (as illustrated in Figure 1.9) to monitor the internalization of P-ASC-J9 by means of a label-free confocal Raman imaging (Figure 1.13).

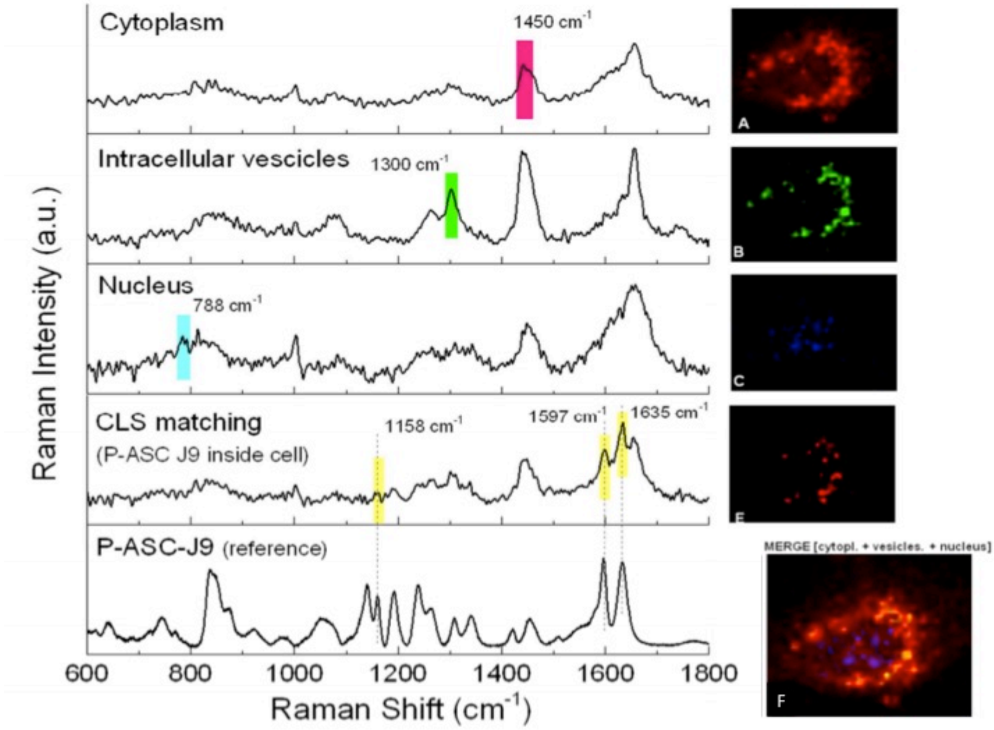

Figure 1.13. Confocal Raman imaging of MCF-7 cells treated with P–ASC-J9. Representative Raman spectra corresponding to cytoplasm, intracellular vesicles, nucleus and P–ASC-J9 are reported highlighting bands used for the determination of the spatial distribution represented with the relative color in the images in panels A, B, C, E, respectively. The reference spectrum of P–ASC-J9 is reported for comparison. In the area where the CLS (classical least squares) matching analysis suggest the presence of P–ASC-J9 (E) the distinctive ASC-J9 bands at 1158, 1597 and 1635 cm^{-1} are clearly recognizable and indicated by dashed lines. (F) Merging of bands described in panel B (intracellular vesicles) and ASC-J9 of panel E; in yellow the positions where the two signals colocalize (F); Scale bar = 4 µm for all images.

Raman images of cells (Figure 1.13) were obtained by integration of the Raman bands around 1450 cm^{-1}, assigned to proteins and lipids (C–H deformation) and mostly representing the cytoplasm (red in Figure 1.13A), the Raman bands around 1300 cm^{-1} related to fatty acids ($-CH_2-$ vibration) and generally colocalized with intracellular vesicles (green, Figure 1.13B) and the Raman band around 788 cm^{-1} assigned to DNA (O−P−O backbone stretch) representing the nucleus (blue, Figure 1.13C). Afterwards, the presence of the reference Raman spectrum of P−ASC-J9 was verified and localized over the entire cell area by classical least squares (CLS) spectral matching analysis (Figures 1.13E). The results of this analysis demonstrate that P−ASC-J9 were efficiently internalized by MCF-7 cells after 24 h of incubation. ASC-J9 bands, in particular those around 1158, 1597 and 1635 cm^{-1} (Figure 1.9 and 1.13), were mostly localized in the perinuclear region and sometimes in the nuclear region. Moreover, in some regions of the cell, these typical ASC-J9 bands colocalized with those related to intracellular vesicles (Figure 1.13F), indicating that ASC-J9 was transported or accumulated in intracellular vesicles, and suggesting a possible involvement of a controlled endosomal pathway for the internalization of P−ASC-J9.

1.3.4 Effects of P-ASC-J9 on cell viability

The cytotoxicity of free ASC-J9 and P−ASC-J9 toward MCF-7 estrogen dependent breast cancer cells were evaluated. First, we analyzed the effects of our nanoformulations on the overall cellular viability in comparison with the particle-free active compound (Figure 1.14).

In our previous work, we checked that PNPs did not affect MCF-7 cells viability, although a curcumin-based PLGA nanocarrier was efficiently able to inhibit the overall cellular growth in a dose− and time−dependent manner.[15] In the present study, MCF-7 cells were exposed up to 72 h with both ASC-J9 and P−ASC-J9 at three concentrations (5, 10 and 20 μM). The assay showed an almost identical dose- and time-dependent effect on cellular viability, thus suggesting a significant cytotoxic activity of the active compound due to its efficient release inside the cellular environment (Figure 1.14A and C). It should be emphasized that the encapsulation of ASC-J9 in PLGA NPs led to a remarkable decrease of cellular proliferation even at the minimal concentration of ASCJ-9 (5 μM) tested, which ameliorates the pharmacological profile of ASC-J9 and makes it possible to use effectively this compound at lower concentrations. Our result is confirmed by similar experiments performed by other authors,[32,33] in which a broad range of artificial curcuminoids were tested on MCF-7 and other breast cancer cells in order to calculate their IC_{50} concentration.

To assess the toxicity of P–ASC-J9 and ASC-J9 towards healthy cells, we used the fibroblast 3T3-L1 cell line, which is non-cancerous, estrogen dependent. Its viability was assessed by the MTT assay during exposure to the two treatments (Figure 1.14B and D).

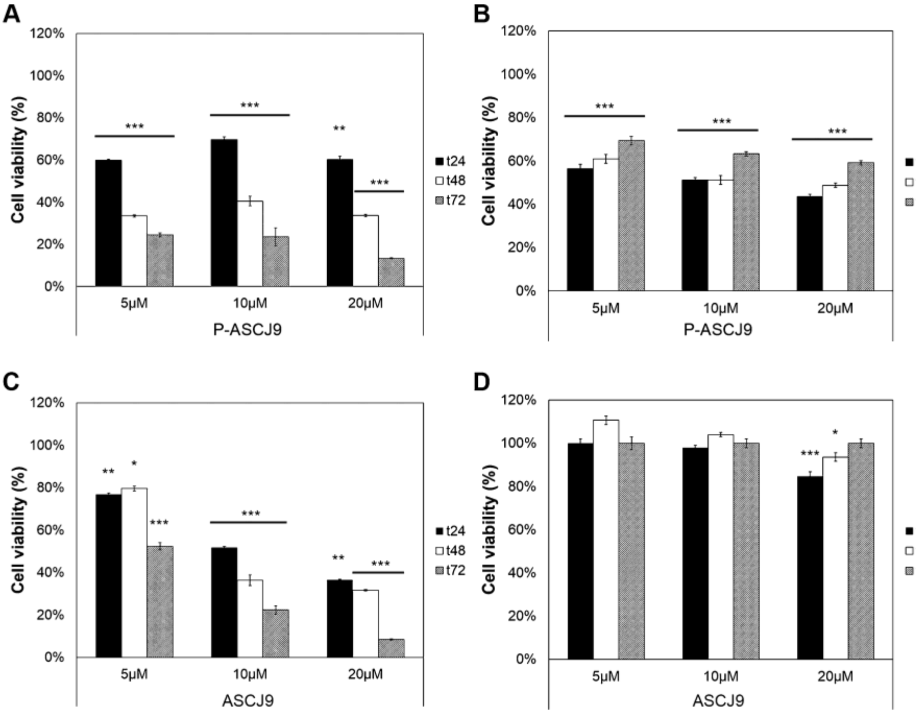

Figure 1.14 MTT assay on breast cancer cells. Effects on cell viability of MCF-7 (A, C) and 3T3-L1 (B, D) in the presence of P–ASC-J9 and free ASCJ-9 (5, 10, and 20 μM) at different times, as indicated. Viability is expressed as relative to untreated cells. Values are means ± SD of three independent sets of experiments. Samples show statistical differences from control at $p < 0.5$ (*), 0.01 (**), and 0.001 (***).

Although we were surprised to note a significant decrease in cell viability during the first 24 h of exposure, this value was slightly recovered up to 72 h, for the whole range of concentrations tested (Figure 1.14B), in contrast to what observed in the MCF-7 cell line.

In order to explore ASC-J9 and P–ASC-J9 cytotoxic activity, we investigated the causes of the decrease of MCF-7 viability. Therefore, we assessed the extent of apoptosis in the MCF-7 cellular population using an Annexin-V specific assay. This test is based on the observation that the phospholipid phosphatidylserine (PS) of the cell membrane could translocate from the inner face of the plasma membrane to the cell surface during the early stage of apoptosis.[34] Once on the cell surface, PS can be easily detected by Annexin V staining, a protein that has a strong natural affinity for PS. ASC-J9 and P–ASC-J9 (5, 10 and 20 μM) were incubated with MCF-7 cells for 3 and 24 h. Annexin V exposure on the cellular surface was checked by flow cytometry (Figure 1.15).

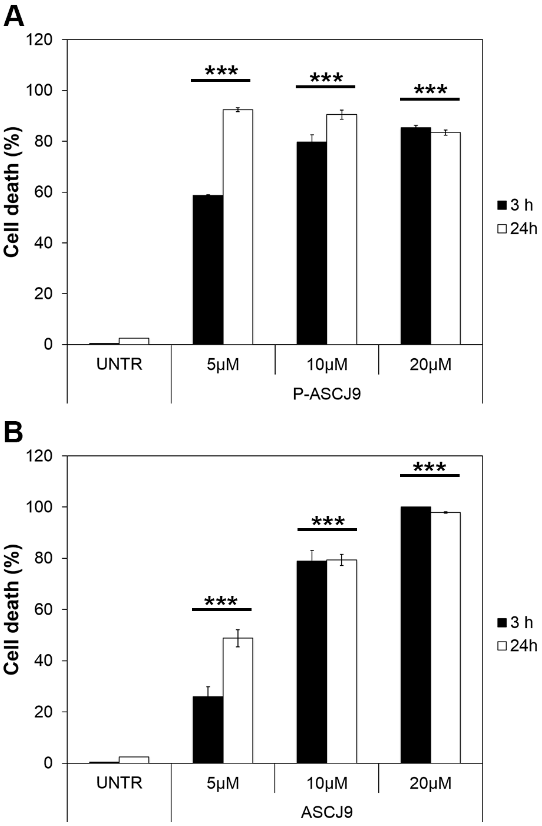

Figure 1.15. Assessment of apoptotic death of MCF-7 cells. The extent of apoptosis (%) was determined after 3- and 24 h-treatments with different concentrations of P–ASC-J9 (A) and free ASC-J9 (B). Data are represented as mean ± SD of three independent experiments, $p < 0.001$ (***) vs untreated cells.

The effect of P–ASC-J9 (Figure 1.15A) is more evident as compared to the pure compound (Figure 1.15B), even at the lowest concentration of 5 μM. These data suggest that the decrease in the overall MCF-7 cellular viability is mainly due to apoptotic events.

We hypothesized that ASC-J9 exploits the same pathway observed for the growth inhibition of prostate cancer cells.[35] In prostate cancer, ASC-J9 was assumed to bind and degrade the androgen receptor, thus suppressing cell growth and further leading to their apoptosis. Likewise, in this case ASC-J9 might be involved in blocking the estrogen receptor of MCF-7, thus leading to an apoptotic event. However, further investigations are required to provide further support to our hypothesis.

1.3.5 P-ASC-J9 induces cell cycle arrest

After establishing that particle-free ASC-J9 and its analogue encapsulated into PLGA could induce apoptotic events in MCF-7 cells, we tried to investigate their effect on the cell cycle. Indeed, there is evidence that similar curcumin-PLGA nanovectors are able to inhibit MCF-7 proliferation by blocking the cell cycle in G2/M phase.[15] This prompted us to check whether also a block of cell cycle could also affect cell viability besides the apoptotic events previously observed. Actually, no data are available on possible effects by ASC-J9 on cell cycle progression so we treated MCF-7 cells up to 72 h with 20 μM of P–ASC-J9 and ASC-J9 (Figure 1.16).

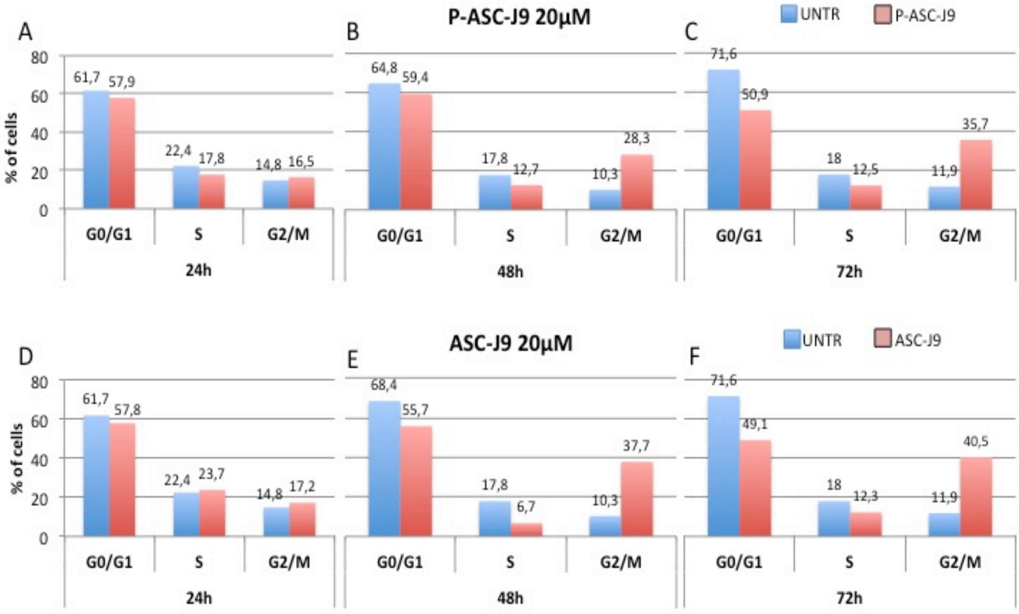

Figure 1.16. Cell cycle analysis. Percentage of cells in each phase of cell cycle of MCF-7 treated with 20 μM P–ASC-J9 (A-C) and ASC-J9 (D-F) compared with untreated cells (blue histograms).

To monitor cell cycle progression we labeled the cells with propidium iodide, a popular red-fluorescent nuclear and chromosome counterstain. This compound is able to intercalate in double stranded DNA, so that the DNA content can be quantified by flow cytometry in each phase of the cell cycle. The DNA content of NP-treated MCF-7 cells was compared with a cell population of untreated cells for the whole time of incubation. The analysis was repeated every 24 h of exposure. As hypothesized, our results show that, at the highest dosage of P−ASC-J9 (20 μM), the NP exposure leads to a significant accumulation of cells in G2/M phase, i.e., from 16.5% after 24 h to 35.7% after 72 h (Figure 1.16A-C). In contrast, the behavior of the G2/M phase of untreated cells remains essentially unaltered. This effect is similar to that observed by treatment with an equal concentration of free ASC-J9 (20 μM) (Figure 1.16D and F), thus confirming that the effect was correlated with the activity of ASC-J9, as a consequence of its time-dependent release from the nanovector.

1.3.6 Assessment of ASC-J9 and P−ASC-J9 effect on ROS levels

Free radicals are highly reactive chemicals endowed with high cytotoxicity. They are naturally formed in the body and in some cases control cellular processes. At high concentrations, however, free radicals can be hazardous for all major components of cells, including DNA, proteins, and cell membranes.[36] In particular, cellular DNA damage may play a role in cancer cell development. Intracellular free radicals are most often oxygen compounds, so they are also referred to as “reactive oxygen species” (ROS). Tightly regulated enzymes, such as NADPH oxidase isoforms, normally generate ROS, whose overproduction often resulting in oxidative stress. This deleterious process might be an important mediator in damaging cell structures. In contrast, beneficial effects of ROS occur at low/moderate concentrations, involving physiological roles in cellular defense against infectious agents and within the function of a number of cellular signaling pathways.[37]

The antioxidant effect is believed to be responsible for many biological activities of curcuminoids, and it is strictly related to their chemical structures. Accordingly, in previous works a plethora of different substituted curcumin analogues were investigated to explore the possibility that newly developed compounds maintained the antioxidant activity to eliminate free radicals.[23] For example, curcumin showed potent radical-scavenging activity, mainly attributed to its free phenoxyl group, whereas non-phenolic curcuminoids failed to reduce the amount of radicals even at high concentrations.[38] As this behavior is strictly related to their chemical structure, our expectation was that ASC-J9 could be less effective as antioxidant activity, which should result in enhanced antitumor effect.

For this purpose, we evaluated the ability of ASC-J9 and P–ASC-J9 to scavenge stable 2,2-diphenyl-1-picrylhydrazyl (DPPH) radical *in vitro*. DPPH assay is a widely used and is regarded as an accurate method to evaluate antioxidant activity.[23] Furthermore, we also checked if the observed cytotoxic effects (figure 14 and 15) correlated with enhancement of intracellular ROS levels, due to their implication in cell survival, as mentioned previously (Figure 1.17).

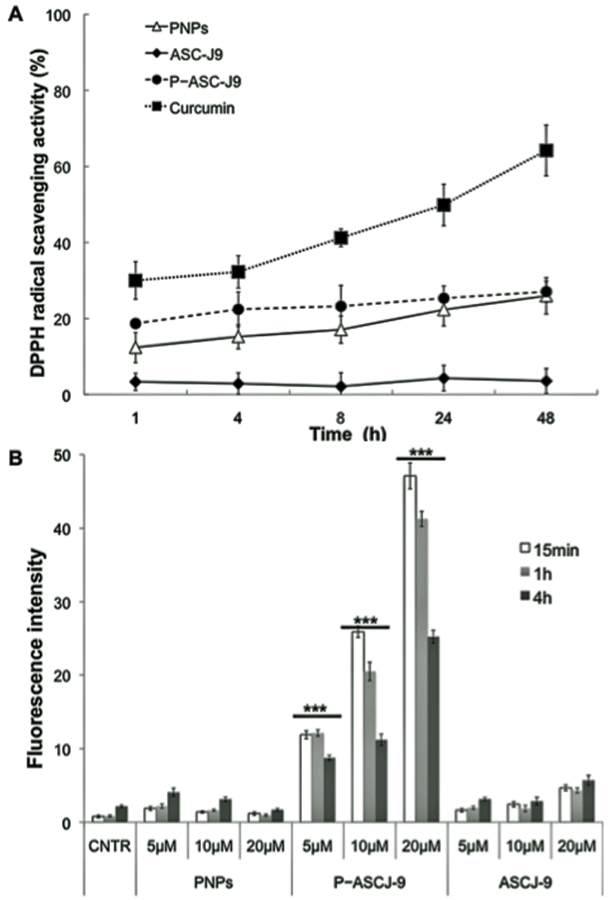

Figure 1.17. DPPH radical-scavenging activity and intracellular ROS levels. (A) DPPH radical scavenging activity after treatment with 10 μM ASC-J9, (tilted squares, solid line) and corresponding P–ASC-J9 (circles, dashed line), PNPs (triangles, solid line), and 10 μM curcumin (squares, dotted line) as a positive control. Data are expressed as relative to % of free radical scavenged compared to DPPH alone (B) MCF-7 cells were labeled with 25 μM DCFDA, cultured with PNPs, free ASC-J9, and P–ASC-J9, and then analyzed on a fluorescent plate reader. Results are expressed as mean ± SD for three replicates. p < 0.001 (***) vs untreated cells.

The radical–scavenging activity of 10 μM ASC-J9, P–ASC-J9, PNPs and curcumin (as a positive control) was evaluated by monitoring the reduction of light absorption at 520 nm by DPPH radical, upon reaction in methanol solution with our compounds in a time span between 1 h and 48 h (Figure 1.17A). As expected, ASC-J9 did not show any antioxidant activity quite likely due to the fact that the phenolic groups are completely methylated. In contrast curcumin was able to decrease more than 50% DPPH radicals after 48 h. Interestingly, PNPs and P–ASC-

J9 displayed similar but scanty scavenging activity (about 10%) after a few hours of incubation, but this effect did not increase critically within the following 2 days. We hypothesize that this behavior could be related to the polyol composition of our PLGA NPs (poly(vinyl alcohol)), which could interact with DPPH.

Next, we assessed the intracellular ROS levels in the presence of different concentrations of PNPs, free ASC-J9 and P–ASC-J9. Figure 1.17B illustrates that, when MCF-7 cells were exposed to P–ASC-J9 for 15 min, 1 and 4 h, the levels of ROS significantly increased compared to untreated cells. Free ASC-J9 did not alter ROS level, even if at 20 μM we noticed a mild increase, suggesting that the poor bioavailability, due to the intrinsic hydrophobic character of the molecule, did not allow the drug to alter the levels of ROS in such a short time. This result confirms that ASC-J9 does not possess antioxidant activity in MCF-7 breast cancer cells. In addition, the oxidative stress, generated by the efficient internalization with PLGA NPs might trigger apoptotic cancer cell death we have observed.

1.3.7 Conclusions

PLGA is a biocompatible member of the aliphatic polyester family of biodegradable polymers. For this reason, it has long been a fashionable choice for drug delivery applications, particularly since it has been FDA-approved for administration in humans under different pharmaceutical formulations.

In this context, PLGA-based nanovectors present well-documented advantages for drug delivery purposes, as their self-assembled matrix enhances drug stability and protection from degradation induced by the external environment. Moreover, nanoparticles can easily penetrate cancer tissues through the “enhanced permeation and retention” (EPR) effect; in this way, the sustained release of the cargo from the polymer matrix could enhance therapies improving the drug pharmacodynamics profiles.

Here, we have encapsulated the artificial curcuminoid ASC-J9 in spherical PLGA nanoparticles, investigating their properties and release kinetics *in vitro* and studying the effects of the sustained release in breast cancer cells. In literature, several works report on the clinical utilization of ASC-J9 for the treatment of several estrogen- and androgen receptor mediated diseases both *in vitro* and *in vivo*. In spite of this, no attempt to employ PLGA nanoparticles as vectors of the drug for breast cancer therapy has been so far reported.

This study demonstrates that PLGA nanospheres are able to efficiently release ASC-J9 intracellularly, thus inducing time- and dose-dependent inhibition of estrogen-dependent MCF-7 cancer cells. The antiproliferative effect is mediated by a G2/M cell cycle arrest and apoptosis even at low drug concentrations; in addition, a high level of ROS was observed in response to the cell treatment with ASC-J9-bearing PLGA NPs (P−ASC-J9). The intracellular release was assessed using a combination of techniques, including confocal laser scanning microscopy performed on a dye-enriched drug analogue and a properly optimized Raman imaging, the latter now emerging as a useful tool to localize poorly fluorescent nanoconstructs inside the cellular compartment. This study clearly indicates that PLGA-based nanoformulation could strongly improve the ASC-J9 administration for the treatment of estrogen-dependent cancer diseases, a goal hampered thus far by its poor bioavailability.

1.4 References

---

[1] International Agency for Research of Cancer – EUCAN: http://eco.iarc.fr/eucan

[2] Levaggi A. et al. The burden of breast cancer from China to Italy*. J Thorac Dis.* 2014 Jun; 6(6): 591–594.

[3] Malhotra GK. et al. Histological, molecular and functional subtypes of breast cancers. *Cancer Biol. Ther*. 2010; 10: 995-960.

[4] Holliday DL. and Speirs V. Choosing the right cell line for breast cancer research. *Breast Cancer Res.* 2011, 13: 215.

[5] Hayes EL. and Lewis-Wambi JS. Mechanism of endocrine resistance in breast cancer: an overview of the proposed roles of noncoding RNA. *Breast Cancer Res.* 2015, 17:40.

[6] Ren X. et al. Iron oxide nanoparticle-based theranostics for cancer imaging and therapy. *Front. Chem. Sci. Eng.* 2014, Vol.8: 253-264.

[7] Danhier F. et al. PLGA-based nanoparticles: an overview of biomedical applications. *J. Control. Release*. 2012, 161: 505-522.

[8] Dinarvand R. et al. Polylactide-co-glycolide nanoparticles for controlled delivery of anticancer agents. *Int. J. Nanomedicine*. 2011; 6: 877-895.

[9] Acharya S. and Sahoo SK. PLGA nanoparticles containing various anticancer agents and tumor delivery by EPR effects. *Adv. Drug Deliv. Rev.* 2011, 63: 170–183.

[10] Fonseca C. et al. Paclitaxel-loaded PLGA nanoparticles: preparation, physicochemical characterization and in vitro anti-tumoral activity. *J. Control. Release.* 2002; 83: 273-286.

[11] Danhier F. et al. Paclitaxel-loaded PEGylated PLGA-based nanoparticles: *In vitro* and *in vivo* evaluation. *J. Control. Release.* 2009; 133: 11-17.

---

[12] Musumeci T. et al. PLA/PLGA nanoparticles for sustained release of docetaxel. *Int. J. Pharm*. 2006; 325: 172-179.

[13] Yoo H.S. et al. Biodegradable nanoparticles containing doxorubicin-PLGA conjugate for sustained release. *Pharm.Res*. 1999; 16: 1114-1118.

[14] Yallapu MM. et al. Fabrication of curcumin encapsulated PLGA nanoparticles for improved therapeutic effects in metastatic cancer cells. *J. Coll. Int. Sci*. 2010; 351: 19-29.

[15] Anand P. et al. Design of Curcumin Loaded PLGA Nanoparticles Formulation with Enhanced Cellular Uptake, and Increased Bioactivity *in vitro* and Superior Bioavailability *in vivo. Biochem Pharmacol.* 2010; 79(3): 330–338.

[16] Verderio P. et al. Intracellular drug release from curcumin-loaded PLGA nanoparticles induces G2/M block in breast cancer cells. *Biomacromol*. 2013 Mar 11; 14(3):672-82.

[17] Asher GN. et al. Clinical utility of curcumin extract. *Altern. Ther. Health Med*. 2013, 19: 20-22.

[18] Kanai M. et al. A phase I study investigating the safety and pharmacokinetics of highly bioavailable curcumin (Theracurmin) in cancer patients. *Cancer Chemother. Pharmacol*. 2013, 71: 1521-1530.

[19] Anand P. et al. Bioavailability of curcumin: problems and promises. *Mol. Pharmaceutics.* 2007, 4: 807-818.

[20] Yamashita S. et al. ASC-J9 suppresses castration-resistant prostate cancer growth through degradation of full-length and splice variant androgen receptors. *Neoplasia* 2012, 14: 74-83.

[21] Yang Z. et al. ASC-J9 ameliorates spinal and bulbar muscular atrophy phenotype via degradation of androgen receptor. *Nat. Med*. 2007, 13: 348-353.

---

[22] Keum CG. et al. Practical preparation procedures for docetaxel-loaded nanoparticles using polylactic acid-co-glycolic acid. *Int. J. Nanomed.* 2011, 6: 2225-2234.

[23] D'Souza SS. et al. Methods to assess *in vitro* drug release from injectable polymeric particulate systems. *Pharm. Res*. 2006, 23: 460-474.

[24] Kim MK. et al. Significant enhancement in radical-scavenging activity of curcuminoids conferred by acetoxy substituent at the central methylene carbon. *Bioorg. Med. Chem.* 2011, 19: 3793-3800.

[25] Fuchs JR. et al. Structure-activity relationship studies of curcumin analogues. *Bioorg. Chem. Med. Lett.* 2009, 19: 2065-2069.

[26] Balasubramanyam K. et al. Molecular orbital basis for yellow curry spice curcumin's prevention of Alzheimer's disease. *J. Agric. Food Chem*. 2006, 54: 3512-3520.

[27] Payton F. et al. NMR study of the solution structure of curcumin. *J. Nat. Prod.* 2007, 70: 143-146.

[28] Mohan PRK. et al. Water soluble complexes of curcumin with cyclodextrins: characterization by FT-Raman spectroscopy. *Vib. Spectrosc*. 2012, 62: 77-84.

[29] Costa P. et al. Modeling and comparison of dissolution profiles. *Eur. J. Pharm. Sci*. 2001, 13: 123-133.

[30] Wang YJ. et al. Stability of curcumin in buffer solutions and characterization of its degradation products. *J. Pharm. Biomed. Anal*. 1997, 15: 1867-1876.

[31] Tonnesen HH. et al. Chemistry of curcumin and curcuminoids. *ACS Symposium Series*. 1992, Chapter 11: 143-153.

---

[32] Qiu X. et al. Synthesis and identification of new 4-arylidene curcumin analogues as potential anticancer agents targeting nuclear factor-kB signaling pathway. *J. Med. Chem.* 2010, 53: 8260-8273.

[33] Ohtsu H. et al. Antitumor agent 222. Synthesis and anti-androgen activity of new diarylheptanoids. *Bioorg. Med. Chem*. 2003, 11: 5083-5090.

[34] Koopman G. et al. Annexin-V for flow cytometry detection of phosphatydilserine expression on B cells undergoing apoptosis. *Blood*, 1994, 84: 1415-1420.

[35] Jiang Q. et al. Targeting androgen receptor leads to suppression of prostate cancer via induction of autophagy. *J. Urol.* 2012, 188: 1361-1368.

[36] Valko M. et al. Free radicals and antioxidants in normal physiological functions and human disease. *Int. J. Biochem. Cell Biol.* 2007, 39: 44-84.

[37] Hancock JT. et al. Role of reactive oxygen species in cell signaling pathways. *Biochem. Soc. Trans.* 2001, 29: 345-350.

[38] Fang X. et al. Design and synthesis of dimethylaminomethyl-substituted curcumin derivatives/analogues: potent antitumor and antioxidant activity, improved stability and aqueous solubility compared with curcumin. *Bioorg. Med. Chem. Lett*. 2013, 23: 1297-1301.

molecular pharmaceutics

Article

pubs.acs.org/molecularpharmaceutics

Antiproliferative Effect of ASC-J9 Delivered by PLGA Nanoparticles against Estrogen-Dependent Breast Cancer Cells

Paolo Verderio,[†,‡,§] Laura Pandolfi,[†,§,∥] Serena Mazzucchelli,[∥] Maria Rosaria Marinozzi,[†] Renzo Vanna,[⊥] Furio Gramatica,[⊥] Fabio Corsi,[∥] Miriam Colombo,[†] Carlo Morasso,[*,⊥] and Davide Prosperi[*,†,∥,⊥]

[†] Dipartimento di Biotecnologie e Bioscienze, Università di Milano-Bicocca, Piazza della Scienza 2, 20126 Milano, Italy

[∥] Dipartimento di Scienze Biomediche e Cliniche "Luigi Sacco", Università di Milano, Ospedale L. Sacco, Via G.B. Grassi 74, 20157 Milano, Italy

[⊥] LABION - Laboratory of Nanomedicine and Clinical Biophotonics, Fondazione Don Carlo Gnocchi ONLUS, Piazzale R. Morandi 6, 20121 Milano, Italy

[‡] Nerviano Medical Sciences s.r.l., Viale Pasteur 10, 20014 Nerviano, Italy

Supporting Information

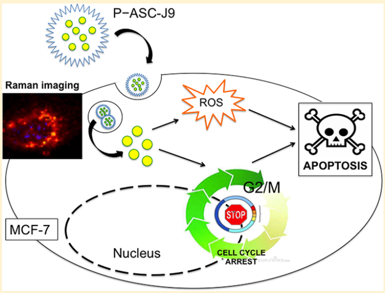

ABSTRACT: Among polymeric nanoparticles designed for cancer therapy, PLGA nanoparticles have become one of the most popular polymeric devices for chemotherapeutic-based nanoformulations against several kinds of malignant diseases. Promising properties, including long-circulation time, enhanced tumor localization, interference with "multidrug" resistance effects, and environmental biodegradability, often result in an improvement of the drug bioavailability and effectiveness. In the present work, we have synthesized 1,7-bis(3,4-dimethoxyphenyl)-5-hydroxyhepta-1,4,6-trien-3-one (ASC-J9) and developed uniform ASC-J9-loaded PLGA nanoparticles of about 120 nm, which have been prepared by a single-emulsion process. Structural and morphological features of the nanoformulation were analyzed, followed by an accurate evaluation of the *in vitro* drug release kinetics, which exhibited Fickian law diffusion over 10 days. The intracellular degradation of ASC-J9-bearing nanoparticles within estrogen-dependent MCF-7 breast cancer cells was correlated to a time- and dose-dependent activity of the released drug. A cellular growth inhibition associated with a specific cell cycle G2/M blocking effect caused by ASC-J9 release inside the cytosol allowed us to put forward a hypothesis on the action mechanism of this nanosystem, which led to the final cell apoptosis. Our study was accomplished using Annexin V-based cell death analysis, MTT assessment of proliferation, radical scavenging activity, and intracellular ROS evaluation. Moreover, the intracellular localization of nanoformulated ASC-J9 was confirmed by a Raman optical imaging experiment designed *ad hoc*. PLGA nanoparticles and ASC-J9 proved also to be safe for a healthy embryo fibroblast cell line (3T3-L1), suggesting a possible clinical translation of this potential nanochemotherapeutic to expand the inherently poor bioavailability of hydrophobic ASC-J9 that could be proposed for the treatment of malignant breast cancer.

KEYWORDS: *PLGA nanoparticles, ASC-J9, breast cancer cells, drug delivery system, chemotherapy*

INTRODUCTION

Breast cancer is one of the leading causes of death for cancer in human females, characterized by a high degree of recurrence after surgical removal and first-line treatment with chemotherapeutics.[1] Despite strong efforts to drive the research toward newly designed strategies to fight cancer, only a few drugs have proved effective in addressing primary tumors and metastases thus reaching the marketplace and an established clinical practice. These include cytotoxic agents directed toward cellular DNA (e.g., doxorubicin and cisplatin), mitotic inhibitors, such as the family of taxanes, and, more recently, targeted therapeutics (e.g., trastuzumab, pertuzumab, and gefetinib as growth factor inhibitors).[2−4] At present, a major problem related to resilience of breast cancer and its recurrence in treated patients is multidrug resistance (MDR), which often leads to chemotherapy treatment failures especially in metastatic cancers.[1,5] It was found, indeed, that some cancer cells can develop resistance to multiple drugs resulting in a significant reduction of the diffusion of the cytotoxic agent into the cytoplasm combined with a rapid efflux from cell mediated by a specific class of proteins termed ATP-binding cassette (ABC) transporters that include P-glycoprotein (P-gp).[6] Recently, it has been suggested that the conjugation of existing drugs with nanoparticles and high-MW polymers may evade MDR.[7] For example, using doxorubicin-conjugated poly(glutamic acid) (PGA), a significant reduction of P-gp-

Received: March 25, 2014
Revised: June 4, 2014
Accepted: June 19, 2014
Published: June 19, 2014

mediated drug inactivation was demonstrated in resistant colon cancer cells,[8] while liposomal formulations of cytotoxic agents have been introduce into the marketplace (e.g., doxil, calyx, and myocet).[7]

In the last few years, novel therapeutics based on polymeric nanoparticle conjugates have led to promising results in the treatment of several diseases, including malignant cancers, due to the flexibility with which their characteristics can be tailored in terms of their chemical composition and physical properties.[9,10] Recent progress in polymerization chemistry and the advances in site-selective and oriented chemical ligation reactions have provided researchers with new possibilities for the assembly of multifunctional polymeric nanovehicles with well-defined architectures.[11] The capability to control the structural features of polymers allowed for polymer self-assembly and consequent conversion into properly sized nanoparticles, with sophisticated morphologies, tunable surface charges, and functionalities.[12] In particular, significant efforts continue to be exerted toward the design and development of polymeric nanocarriers (PNCs) with tailored physical, chemical, and biological properties, which can be capitalized in healthcare clinical applications.[13] Indeed, PNCs can be derivatized with a plethora of terminations, including hydrophobic, hydrophilic, small molecules and bioactive macromolecules, to amplify their delivery beyond certain biological barriers, such as skin, tissues, and blood, cellular and intracellular compartments.[14] For instance, cellular uptake is highly challenging, especially for hydrophobic drugs: the interactions of nanoparticles at the nano−bio interface with components of the outer cellular membranes, followed by their internalization into vesicles, are the initial steps for endocytosis processes.[15]

Poly(lactide-*co*-glycolide) (PLGA) has been reported as an attractive solution to develop nanoformulations for cancer treatment.[16] Increasing experience in the field of preparation, characterization, and *in vivo* application of chemotherapeutic compounds carried by PLGA nanoparticles has provided the necessary driving force to move toward promising clinical use of these agents in cancer treatment, with higher efficacy and fewer side effects.[17] For this reason, PLGA has been recently approved by international medicine agencies for some parenteral administration formulations.[18] In a recent work, we have demonstrated the potential activity of intracellular drug release from curcumin-loaded PLGA nanoparticles in breast cancer cells, which resulted in tumor growth inhibition induced by a cell cycle arrest in G2/M phase.[19] The medicinal properties of curcumin, a natural product obtained from the rhizome of *Curcuma longa*, have been shown to include a wide range of pharmacological activities, including chemotherapeutic properties.[20,21] As a consequence, a broad range of curcumin analogues have been synthesized with the aim to improve the pharmacological profile of the natural product, as the poor solubility combined with low stability and bioavailability limit its use in clinical practice. These compounds have been further tested investigating their activity against known and specific biological targets.[22]

Among these synthetic derivatives, in recent years, *in vivo* and *in vitro* studies have demonstrated that 1,7-bis(3,4-dimethoxyphenyl)-5-hydroxyhepta-1,4,6-trien-3-one, commonly referred to as ASC-J9, held great promise in the treatment of prostate cancer cells. ASC-J9 is able to bind the androgen receptor (AR) thus leading to a decreased AR transactivation, resulting in the suppression of AR-mediated cell proliferation, angiogenesis, and tumor growth.[23] In other works, ASC-J9 showed also effects on other steroid receptors.[24] In addition, ASC-J9 has been suggested as a possible therapeutic agent for the treatment of AR-dependent neurodegenerative disorders; for example, the development of spinal and bulbar muscular atrophy (SBMA) is correlated to a motor neuron degeneration resulting from the aggregation of the AR with an expanded polyglutamine tract (AR-polyQ). ASC-J9 has been also demonstrated to increased cell survival by decreasing AR-polyQ nuclear aggregation through their degradation *in vitro* and *in vivo*.[24] Structurally, ASC-J9 possesses a chemical structure very similar to that of curcumin as olefin bonds, indeed the β-diketone moiety, is intact. Nevertheless, ASC-J9 presents a variation on the aromatic substituents, where the two hydroxyls, present on curcumin, are completely methylated. This small difference, however, makes ASC-J9 extremely hydrophobic (more than curcumin), and this hurdle limits its administrable dosage far more than other curcuminoids under investigation for cancer therapy.[25]

Considering that aggressive breast cancer cell populations are generally estrogen-dependent,[26,27] and based on the promising data collected from previous *in vivo* investigations on androgen receptor in prostate cancer, in the present work, we have developed ASC-J9-loaded PLGA nanocarriers in order to improve the drug solubility and investigated their effect on the growth inhibition of MCF-7 breast cancer cells, an estrogen-dependent human line that has proved the capability to develop MDR.[28,29] In particular, we have characterized our nanoconstruct and estimated its drug loading capability and *in vitro* release profile. In addition, the drug local release inside the cytoplasm of MCF-7 breast cancer cells has been assessed by confocal microscopy and by a label-free Raman imaging experiment optimized *ad hoc* for this purpose. This nanoconstruct led to the inhibition of cell proliferation induced by ASC-J9, triggering cycle arrest and eventually apoptosis.

EXPERIMENTAL SECTION

Materials and Methods. 50:50 PLGA (poly(lactic-*co*-glycolic acid), acid terminated, M_w = 45−60 kDa with an inherent viscosity of 0.59 dL g^{-1}); poly(vinyl alcohol) (PVA, M_w = 9−10 kDa, 80% hydrolyzed) was purchased from Sigma-Aldrich (St. Louis, MO) and used as received. Other chemicals and solvents were supplied by Sigma-Aldrich (St. Louis, MO), Fluka (St. Gallen, Switzerland), and Riedel-de Haen (Seelze, Germany) and used as received. Water was deionized and ultrafiltered by a Milli-Q apparatus (Millipore Corporation, Billerica, MA). ^{1}H NMR spectra were recorded on a Bruker 400 MHz spectrometer (Bruker, Leipzig, Germany), and chemical shifts (δ) are reported in parts per million (ppm) relative to the solvent peak; internal standard was tetramethylsilane (TMS).

ASC-J9-Loaded PLGA Nanoparticles (P−ASC-J9). P−ASC-J9 were prepared using the "solvent−evaporation" process,[19,30] (also termed the single-emulsion process), which is the gold standard technique for the encapsulation of hydrophobic compounds. The procedure for our standardized nanoformulation followed the same synthetic steps of the previously published preparation with curcumin.[19] The reagents used here were PLGA polymer (50 mg, 1 μmol) and freshly prepared ASC-J9 (5 mg, 12.5 μmol), corresponding to 10 wt % polymer. Nanoparticle characterization, drug content evaluation, morphology, Raman spectroscopy, dynamic light scattering (DLS) distribution, ζ-potential, nanoparticle tracking analysis (NTA, NanoSight distribution), fluorescence analyses, and kinetics of drug release were evaluated following nanoparticle synthesis.

Drug Loading and Encapsulation Efficiency (EE %). UV−vis and fluorescence spectroscopy were used to determine the amount of drug encapsulated in P–ASC-J9. P–ASC-J9 powder (500 μg) was dispersed in water and mixed with a chloroform/ethanol solution 90:10. After stirring (3 h), the extracted ASC-J9 from nanoparticles was determined in the organic phase by UV–vis (424 nm) and fluorescence emission (λ_{exc} = 420 nm; λ_{emi} = 522 nm). Pure PLGA and PVA did not interfere in the analysis of ASC-J9. The encapsulation efficiency was calculated (eq 1) as

$$\mathrm{EE}\,(\%) = \frac{\mathrm{drug}_{\mathrm{loaded}}(\mu \mathrm{g}_{\mathrm{drug}}\cdot \mathrm{mg}_{\mathrm{NPs}}{}^{-1})}{\mathrm{drug}_{\mathrm{initial}}(\mu \mathrm{g}_{\mathrm{drug}}\cdot \mathrm{mg}_{\mathrm{NPs}}{}^{-1})} \times 100 \qquad (1)$$

UV–vis quantification was recorded with the same method previously published by using a Nanodrop 2000C spectrophotometer from Thermo Fisher Scientific (Wilmington, Germany) and a Fluoromax-4P spectrofluorometer from Horiba Scientific (New Jersey, USA), respectively.[19]

Morphology. SEM images of nanoparticles were obtained by a Zeiss EM-109 microscope (Oberkhochen, Germany) operating at 80 kV. For analyses, nanoparticles were dispersed under sonication in water (5 μg mL^{-1}) and a drop of the resulting solution was placed on a Formvar/carbon-coated copper grid and air-dried.

Particle Size and Surface Charge Analyses. P–ASC-J9 and PNPs were dispersed in the solvent until a final sample concentration of 5 μg mL^{-1}. Dynamic light scattering (DLS) measurements were performed at 90° using a 90 Plus Particle Size Analyzer from Brookhaven Instrument Corporation (Holtsville, NY). ζ-Potential measurements were elaborated on the same instrument equipped with an AQ-809 electrode soaked in 10 mM NaCl aqueous solution (pH 7.25, σ = 14.2 mS cm^{-1}); data were processed by Zeta-Plus software. Sight distribution spectra were collected (at 23 °C) by NanoSight LM10 from NanoSight Limited (Amesbury, U.K.) and analyzed with Nanoparticle Tracking Analysis (NTA) software.

Fluorescence Stability Analysis of Drug Encapsulated. Fluorescence emission of free and encapsulated ASC-J9 was recorded in a range from 490 to 700 nm (λ_{ex} = 420 nm). Buffers used: 20 mM acetate buffer (pH = 4.75), 20 mM phosphate buffer (pH = 7.40), 20 mM ammonium buffer (pH = 9.25), and cell culture Dulbecco's modified Eagle's medium (DMEM) (pH = 7.40). Free ASC-J9 (5 mM in DMSO stock solution) was diluted in all buffers at a final concentration of 5 μM; however, P–ASC-J9 were dispersed directly in the medium at the same drug content. PNPs at the same concentration were demonstrated in a previous work not to interfere in the analysis.[19]

***In Vitro* Drug Release Profiles.** *In vitro* ASC-J9 release from PCNPs was evaluated by the dissolution technique.[19,31] ASC-J9 release was performed at 37 °C in all buffers used for fluorescence analyses (from acidic to alkaline pH), supplemented with 2 wt % bovine serum albumin (BSA) to mimic a biological environment and to enhance drug dissolution in these solvents. Maximum drug solubility was preliminary estimated in order to calculate the necessary amount of solvent to perform kinetics in *sink* conditions. Briefly, a nanoparticulate dispersion of P–ASC-J9 (1 mg mL^{-1}) in corresponding buffer was maintained at 37 °C in a closed container, to prevent evaporation of the solvent, under mild stirring. Samples (1 mL) were withdrawn at regular time intervals, and nanoparticles were separated from the supernatant by centrifugation (8000*g*). The nanoparticulate deposit was resuspended in fresh medium (1 mL) and replaced in the kinetic batch. Every 24 h all the solvent was completely replaced with fresh medium. After centrifugation, solubilized ASC-J9 in each particle-free supernatant was analyzed spectrophotometrically at 424 nm. All kinetic measurements were performed in triplicate, and the average values were taken. The kinetic analysis of the release data was elaborated using the Peppas–Korsmeyer model (eq 2).[32]

$$f_t = kt^n$$
$$\log f_t = \log k + n\cdot\log(t) \qquad (2)$$

where f_t is the fractional amount of drug release, k is the release constant, n is the release exponent and t is the time of release. For the determination of the exponent (n), we decided to investigate the linear portion of the kinetic curve until the fractional release amount reached 70%.

Raman Spectroscopy. The Raman analysis of free ASC-J9, P–ASC-J9, and PNP was performed using an Aramis Horiba Jobin-Yvon micro-Raman spectrometer equipped with a HeNe laser operating at 633 nm and a solid state near-infrared laser operating at 785 nm. Briefly, a small amount of powder was deposited on a silica slide and measured without other preparation. Spectra were collected using the 785 nm laser line with an output power of 50 mW focused on the sample through a 10× objective. Data were obtained averaging 3 different measurements of 20 s each.

Radical Scavenging Efficiency. 2,2-Diphenyl-2-picrylhydrazyl (DPPH) was used as the source of free radicals.[33] Stock solution of free ASC-J9 (5 mM in DMSO) was further diluted to reach the same amount of drug in the nanoformulation. P–ASC-J9 and PNPs corresponding to 10 μM drug content were suspended in water (4 mL) and used for the analysis. To the aqueous reaction mixture, a methanolic solution of DPPH (5 mM) was added to reach a final concentration of 100 μM DPPH; dark colored solutions were kept in the dark at 37 °C for 1, 4, 8, 24, and 48 h, respectively. For each time, the DPPH scavenging activity was determined spectrophotometrically at 520 nm against untreated DPPH solution as control. All results correspond to ± standard deviation (SD) of 5 individual readings for each sample. The antioxidant activity was calculated (eq 3) as percentage of DPPH that was decreased in comparison with the untreated sample (100%):

$$\text{antioxidant activity}\,(\%) = \frac{\mathrm{Abs}_{\mathrm{untreated}} - \mathrm{Abs}_{\mathrm{treated}}}{\mathrm{Abs}_{\mathrm{untreated}}} \times 100 \qquad (3)$$

Cell Cultures and *in Vitro* Experiments. MCF-7 human breast cancer cells were maintained in 50 vol % Dulbecco's modified Eagle's medium (DMEM) and 50 vol % F-12 supplemented with 10 vol % fetal bovine serum (FBS), L-glutamine (2 mM), penicillin (50 UI mL^{-1}), and streptomycin (50 mg mL^{-1}). 3T3-L1 mouse embryo fibroblasts were maintained in the same medium of MCF-7 with the exception of F12. Both cell lines were grown at 37 °C in a humidified 5 vol % CO$_2$ incubator. Cell culture medium and biological chemicals were purchased from EuroClone. For each *in vitro* test, P–ASC-J9 or PNPs were resuspended in complete culture medium to a final drug concentration of 5 μM, 10 μM, and 20 μM. Stock solutions of free ASC-J9 (5 mM) were diluted with the culture medium to get the same amount of drug carried by P–ASC-J9.

Cell Viability. To test P–ASC-J9 or PNPs toxicity, MTT assay was performed. MCF-7 and 3T3-L1 were seeded (5 × 10^3 cells per well) in a 96-well plate and grown for 24 h. The cells were then treated with different ASC-J9 concentrations (5, 10, and 20 μM) of PNPs, free ASC-J9, and P−ASC-J9. After 24, 48, and 72 h of exposure at 37 °C, the cellular viability was monitored according to the manufacturer's instructions (Cell Titer 96 Non-Radioactive Cell Proliferation Assay, Promega), and absorbance of formazan product was read immediately by an ELISA plate reader using a test wavelength of 570 nm and a reference wavelength of 620 nm. The results are expressed as means ± standard deviation (SD) of 3 individual experiments for each cell line.

Cell Death Analysis. MCF-7 cells were seeded in 6-well plate at a concentration of 1.5×10^5 per well and were grown for 24 h. Then cells were incubated for 3 and 24 h at 37 °C with 5, 10, and 20 μM of PNPs, free ASC-J9, and P−ASC-J9, respectively. After exposure, floating cells were collected in FACS tubes; otherwise, adherent cells were washed twice with phosphate buffer solution (PBS), trypsinized, and gathered up in the same FACS tube within previous prepared samples; all collected cells were treated for FACS analysis according to Annexin V-PE-Cy5 Apoptosis detection kit (BioVision Inc.). Sample acquisition (at least 20 thousand events) was performed by FACS Calibur flow cytometer (Becton Dickinson) and analyzed by CellQuest Pro Software (BD).

Cell Cycle Analysis. MCF-7 were seeded in a 6-well plate (10^5 cells per well) and after 24 h were incubated with 5, 10, and 20 μM free ASC-J9 and P−ASC-J9 for 24, 48, and 72 h at 37 °C. Once collected and fixed (70% ethanol), cellular DNA was stained at 4 °C with a mixture of propidium iodide (10 μg mL^{-1}) and RNase A (18 μg mL^{-1}). Sample acquisition was performed using flow cytometry equipped with a doublet discriminator module (FACS Calibur; Becton Dickinson, San Jose, CA, U.S.A.), and the DNA content was analyzed by Flowjo software (TreeStar Inc., OR, U.S.A.).

Measurement of Intracellular Level of Reactive Oxygen Species. Reactive oxygen species (ROS) were measured using DCFDA Cellular ROS detection assay kit (abcam—MitoSciences), according to the manufacturer's instruction. MCF-7 were seeded in a 96-well plate at a concentration of 5×10^3 cells per well and grew for 24 h. Then cells were washed with supplied buffer followed by incubation with 100 μL well^{-1} of DCFDA (25 μM) for 45 min at 37 °C; next cells were incubated with PNPs, free ASC-J9, and P−ASC-J9 at a drug concentration corresponding to 5, 10, and 20 μM for 15 min, 1 h, and 4 h at 37 °C. Untreated cells were used as a negative control. Fluorescence was measured in triplicate by Fluoromax-4P spectrofluorometer (λ_{ex} = 485 nm; λ_{em} = 535 nm).

Confocal Laser Scanning Microscopy. Cells were grown on a coverslip and seeded in 6-well plates (10^5 cells), and the same experimental procedure for FACS analysis was followed. Images were obtained with Leica DM IRE2 confocal microscope equipped with an argon/krypton laser to excite coumarin-6 at λ = 488 nm. At least 5 fields per each sample of two biological replicates were taken.

Raman Imaging. 1.5×10^5 cells were seeded on poly lysine coated CaF_2 disks used as optical substrate, grown for 24 h, and incubated for 24 h at 37 °C with 5 μM PNPs and 20 μM P−ASC-J9. Untreated cells were tested as a negative control. Cells were then washed with PBS and fixed for 30 min at 37 °C with 2 vol % paraformaldehyde−PBS solution. Raman imaging was performed using the Aramis Horiba Jobin-Yvon micro-Raman spectrometer utilizing the HeNe, 633 nm laser (power 20 mW), coupled with an immersion objective (63×/1.0 NA). Each cell, immersed in PBS, was scanned with a step size of 700 nm over the entire cell area, for 1 s × 3 repetitions for each step, with the laser focused at 3.5 μm above the CaF_2 surface. The resulting Raman mapping images were then processed (spectral noise removal, baseline correction, univariate imaging, RGB images manipulation, CLS (classical least squares) matching) by using LabSpec6 (HORIBA Scientific).

Statistical Analysis. All biological data are expressed as mean ± SD. Data were analyzed by Student's *t*-test. Post hoc analysis was carried out when statistical significance $P < 0.05$ (*), $P < 0.01$ (**), and $P < 0.001$ (***) was detected.

■ RESULTS AND DISCUSSION

Preparation and Characterization of P−ASC-J9 Nanoformulation. Curcumin has been recently one of the most studied compounds among natural products, which has demonstrated involvement in several bioactivities:[34] for this reason, a few analogues have been developed with the aim to increase both its specificity and therapeutic action. In this work, we have focused our attention on the synthesis and nanoformulation of a relatively new curcumin analogue, named ASC-J9, possessing enhanced hormonal inhibitory activities against prostate cancer,[23,24] with the aim to test its efficacy toward an estrogen receptor-positive breast cancer cell line. The general procedure for synthesizing ASC-J9 is summarized in the Supporting Information (Scheme S1), where the backbone starting material, 2,4-pentanedione, has been condensed with the 3,4-dimethoxybenzaldehyde in dimethylformamide (DMF) at 65 °C using a slight modification of the Pabon method.[34,35] The main steps involved in this process are basically two: (i) The protection of the active methylene group with a boron complex, which is necessary in order to avoid Knoevenagel condensation at C-3 of 2,4-pentanedione, is given by reacting acetylacetone in the presence of boric oxide (B_2O_3). (ii) The acetyl acetone−boric oxide stable intermediate complex reacts through with less reactive methyls, within the appropriate 3,4-dimethoxybenzaldehyde using 1,2,3,4-tetrahydroquinoline (THQ) as catalyst. At the end of the reaction, the boron complex is completely cleaved by acidic hydrolysis, giving the desired product in 55% yield. The excellent product quality derived from this synthetic schedule, as checked from ^{1}H NMR analysis, was consistent with recorded data (Figure S1 in the Supporting Information).

Later on, with the aim to efficiently encapsulate ASC-J9 inside the polymer matrix of PLGA nanoparticles, "single-emulsion" technique was picked out as the most accurate method for the preparation of water-dispersible P−ASC-J9 and the corresponding drug-free nanoparticle system, PNPs. This technique, indeed, is the ideal method for the encapsulation of hydrophobic molecules; as, at the same time, it allows the best performances to be obtained in terms of encapsulation efficiency within homogeneous particle size distribution.

During the formation of nanoparticles, water-soluble PVA (5.0 and 0.3 wt %) is added to the emulsion as a surfactant to homogenize and stabilize the suspension, avoiding undesired nanoparticle agglomeration. Electron microscopy (TEM and SEM) analyses of P−ASC-J9 (Figure S2 in the Supporting Information) showed that the generated nanoparticles are spherical with a diameter of 110.0 ± 14 nm. Mean size distribution recorded by NTA confirmed a nanoparticle size with a maximum in intensity of 131 ± 25 nm, with only a bigger subpopulation at 192 nm. In the same way, analysis of PNPs was consistent with reported data.[19]

With DLS performed in 20 mM PBS at pH 7.2, we analyzed nanoparticle suspension behavior in aqueous solution directly from the resuspension of the crude powder after lyophilization

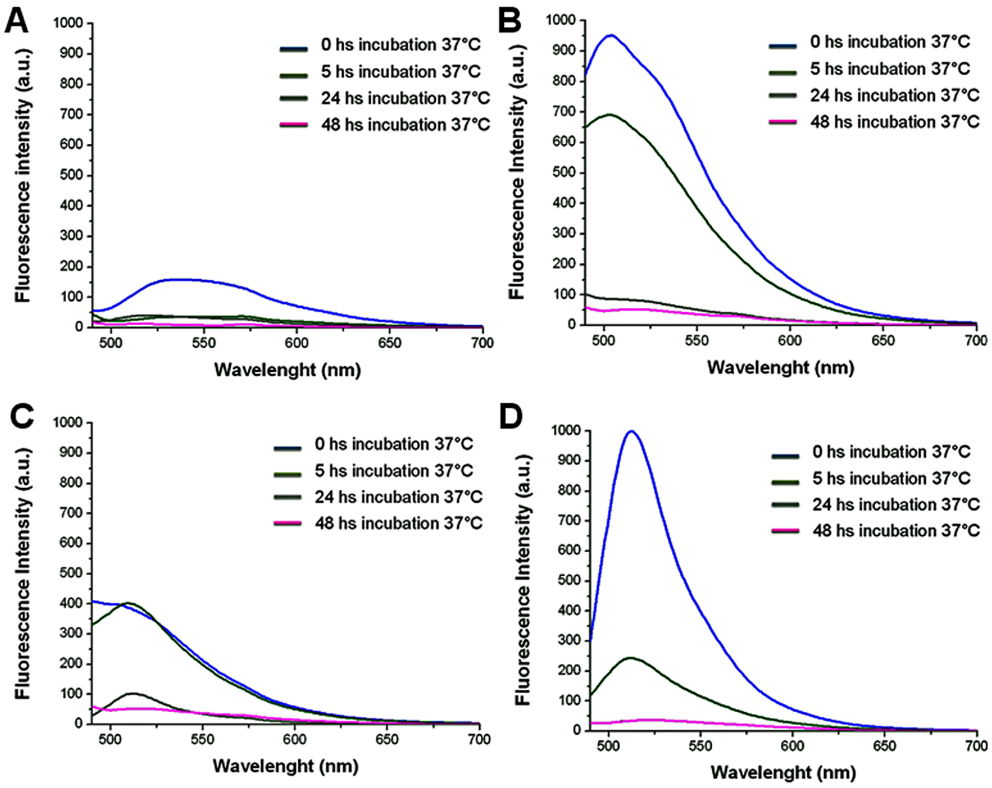

Figure 1. Drug structure preservation from external environment in biological milieu. Fluorescence emission spectra of 5 μM ASC-J9 (A, C) and equal amount of P−ASC-J9 (B, D) until 48 h of incubation at 37 °C. Blue line (time zero); green line (5 h); gray line (24 h); pink line (48 h). Excitation wavelength was fixed at 420 nm for all measures. In summary: (A, B) ASC-J9 and P−ASC-J9 dispersion in 20 mM phosphate buffer, pH 7.40; (C, D) ASC-J9 and P−ASC-J9 dispersion in DMEM cell culture medium, pH 7.40.

(details are summarized in Table S1 in the Supporting Information). From DLS analyses, hydrodynamic diameters of 145.6 ± 22 nm (PDI, 0.115) and 171.5 ± 15 nm (PDI, 0.095) were measured for P−ASC-J9 and PNPs, respectively, showing a good particulate dispersion in the physiological milieu, without observing micellar aggregation after cryodesiccation. Simultaneously, the surface charges of P−ASC-J9 (−18.7 ± 2.9, Table S1 in the Supporting Information) and PNPs (−21.4 ± 3.1, Table S1) were analyzed by ζ-potential in 1 mM NaCl solution at pH 7.25 (σ = 14.2 mS cm^{-1}) and further through a pH titration from alkaline to acidic environment (pH range, 3−9), as shown in Figure S3 in the Supporting Information. Both nanoparticle systems are strongly negatively charged among almost the whole pH range (4−9), except for pH 3 where the external carboxyl groups of PLGA are likely to be protonated.

Next, we assessed the propensity of our nanoparticle formulation to protect the incorporated drug from the external environment. For instance, our primary purpose was to evaluate if the synthetic process was suitable to gain a nanoformulation without altering the structural features of ASC-J9, which exploits its pharmacological activity. In addition, the maintenance of the polymer matrix plays a critical role because it should avoid drug degradation from the external environment until the nanocarrier reaches the target site of action. Since curcumin and most of its analogues possess a green fluorescence emission under appropriate excitation wavelengths (Figure S4 in the Supporting Information), a series of fluorescence analyses were performed at physiological conditions with the aim to demonstrate the behavior of encapsulated ASC-J9 in terms of chemical properties inside the polymer matrix (Figure 1).

This experiment was performed in 20 mM PBS, pH 7.40 (panels A, C), and DMEM containing 10 wt % serum, pH 7.40 (panels B, D), checking the overall green fluorescence intensity up to 48 h of incubation at 37 °C. At a first impression, higher fluorescence intensities of P−ASC-J9 were detected in comparison with free drug in both solvents, showing broad fluorescence peaks, which became increasingly lower over time. We checked preliminarily that PNPs at the same concentration did not interfere with the analysis. The same type of analysis was performed in other buffers commonly used in clinical treatments, to verify the maintenance of the polymer shell at acid and/or alkaline pHs for the whole time of incubation used previously (Figure S5 in the Supporting Information). It was worth noting that similar behaviors were maintained throughout the overall pH range, suggesting that our formulation was able to efficiently maintain its protecting features up to 24 h of dissolution. However, later on, the polymer matrix began to destabilize, increasing the drug exposure toward the external environment and the relevant solvent effects.

According to this result, we tried to apply Raman spectroscopy to validate our hypothesis. Raman spectra of free ASC-J9, P–ASC-J9, and PNP were performed in order to confirm the encapsulation and the structural integrity of ACS-J9 inside PLGA. The Raman spectrum of P–ASC-J9 (Figure 2B) is basically given by the sum of the peaks present in the spectra of the ASC-J9 (Figure 2A) and of the empty PLGA nanoparticles (Figure 2C) with minor shifts. In particular, peaks at 1597 cm^{-1} and at 1635 cm^{-1} relative to the C═C aromatic stretching and to the C═O stretching, respectively, as well as the peak at 1158 cm^{-1} assigned to the C–OH stretching of ASC-J9, appear to be well conserved in the P–ASC-J9 spectra, suggesting that the molecule maintains its preference for the enolic conformation even when it is encapsulated in the polymer. Several computational chemistry works have confirmed that, in curcumin compounds, the energy of the enol form is 6.7 kcal mol^{-1} lower than that of the diketone tautomer.[36] There are several factors that likely contribute to this effect, including (i) the acidic nature of the protons on the central methylene carbon, (ii) the stabilization of the enol form via an intramolecular hydrogen bond, and (iii) the establishment of a fully conjugated system. This prediction was corroborated by X-ray crystal structures and more recently by NMR analysis of the solution structure of curcumin,[37] in which the compound existed solely in the enol form.

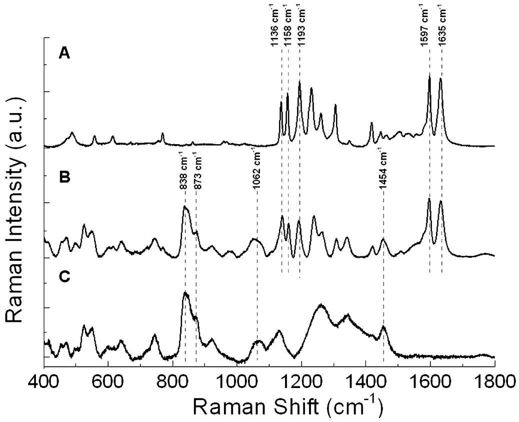

Figure 2. Raman spectra of free ASC-J9 (A), P–ASC-J9 (B), and PNPs (C). The most distinctive peaks of ASC-J9 and PLGA are indicated by the dashed lines and compared with the spectra of the encapsulated drug.

In the spectra of the encapsulated drug (Figure 2B), it is even possible to recognize some of the bands relative to the lactic units of the polymer at 873 cm^{-1} (relative to the C–COO stretching) and at 1454 cm^{-1} (–CH_3 asymmetric bending), and of the glycolic units at 838 cm^{-1} (–CH_2 rocking) as reported in a previous study.[38]

In this way we could demonstrate that P–ASC-J9 were able to efficiently encapsulate the drug and, simultaneously, the polymer matrix was able to protect ASC-J9 from the external environment. In addition, our study validates that the nanoencapsulation does not alter its chemical structure, which should be the optimal condition for drug activity.

***In Vitro* Drug Release Kinetics.** Release kinetics is a fundamental study, which offers a plethora of information about drug diffusion timing and critical implications about the porosity of nanoformulations at the molecular level. Moreover, it allows researchers to find possible interactions between the drug–environment interface and the polymer matrix, which should affect the mechanism and rate of future sustained delivery *in vivo*.

At first, we estimated the amount of ASC-J9 in terms of loading capability of PLGA nanosystem. A calibration curve in a mixture of vol % 90:10 chloroform/ethanol of as synthesized ASC-J9 was prepared for analyses. Briefly, P–ASC-J9 were dispersed in aqueous solution and added to the organic chlorinated phase for 3 h, just the time necessary to dissolve the drug into the organic solvent. ASC-J9 was detected by UV–vis and fluorescence spectroscopies. The drug loading, calculated by wt % differences, revealed that 65 ± 3 μg of drug was encapsulated for each mg of PLGA nanoparticles (6.5 wt % of the polymer). The initial amount of ASC-J9 was 10.0 wt %, so that we could achieve an average of 65% encapsulation efficiency into the polymer matrix (eq 1).

After the estimation of the drug loading, we tried to carefully calculate the maximum solubility of ASC-J9 in all conditions previously tested for fluorescence studies (Figure S6 in the Supporting Information). For instance, kinetics studies were performed in acidic acetate buffer, physiological phosphate buffer, and alkaline ammonium buffer; each medium was supplemented with 2.0 wt % bovine serum albumin (BSA) with the aim to improve ASC-J9 dissolution, due to its strong hydrophobic behavior in pure buffer. Since it is wise to employ *sink* conditions during *in vitro* testing, the maximum solubility calculation allowed us to predict the small volume of medium that could be used to ensure drug solubility maintaining *sink* conditions and preventing accumulation of polymer degradation products.

Based on these calculations, our release study was performed at 37 °C in 20 mM PBS containing P–ASC-J9 suspension (Figure 3).

Small amounts of sample were withdrawn at fixed times, and the nanoparticles were separated by the supernatant; the sediment was redispersed in the same volume of fresh buffer and quickly replaced into the reactor. We observed an initial burst release during the first 8 h of incubation (75.3 ± 6.5%); within the following 48 h, this value rose to 92.1 ± 2.0%. Finally, the kinetics reached a plateau corresponding to a maximum after 10 days (very close to 100%), suggesting a continuous and prolonged release by our nanocarrier. Kinetic elaborations were fitted according to the Korsmeyer–Peppas model.[32] We observed that the fractional amount of drug release log f_t versus log t was found to be 0.983. Meanwhile, the release exponent (n) and the release constant (k) were estimated around 0.517 and 0.619, respectively. From this calculation, we could approximate that ASC-J9 release from our nanoconstruct followed a Fickian law diffusion with a release exponent of 0.51.

The same experiment was repeated in an acidic 20 mM acetate buffer (pH 4.75, supplemented with 2.0 wt % BSA) and an alkaline 20 mM ammonium buffer (pH 9.25, supplemented with 2.0 wt % BSA), as shown in Figures S7 and S8 in the Supporting Information. Basically, the ASC-J9 release in acidic condition followed the same Fickian law diffusion with a release exponent of 0.45; however, the lower solubility of the drug in this buffer reduced the overall release, which reached only a maximum level of 83.1 ± 3.2% within 10 days. On the contrary, despite the higher solubility ratio of ASC-J9 in alkaline condition, the cargo

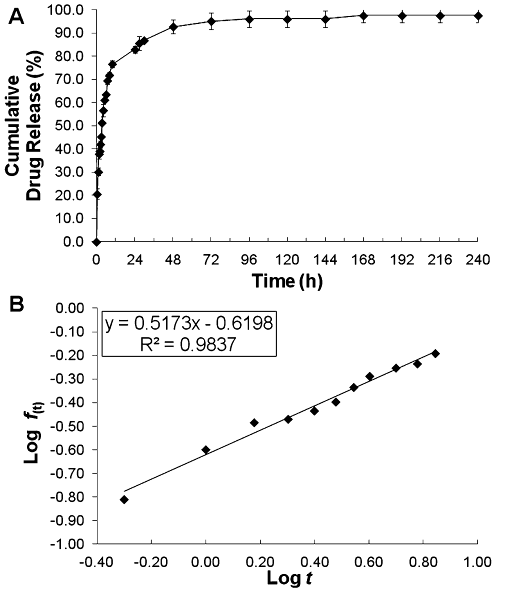

Figure 3. *In vitro* ASC-J9 release kinetics. (A) ASC-J9 dissolution profile from P−ASC-J9 using the dissolution technique in 20 mM PBS (pH 7.4, supplemented with 2.0 wt % BSA); values represent the average ± SD of three independent batches. (B) Elaboration of the kinetic rate keeping in consideration the Peppas−Korsmeyer model.

release in ammonium buffer was drastically reduced, reaching a maximum of 59.0 ± 1.5% within 10 days. This behavior should be correlated to the degradation of curcuminoids in alkaline conditions, where their hydrolytic degradation was decreased by the formation of several byproducts as reported in the literature.[39,40]

Effects of P−ASC-J9 on Cell Viability. The cytotoxicity of free ASC-J9 and P−ASC-J9 was evaluated toward MCF-7 estrogen dependent breast cancer cells. First, we analyzed the effects of our nanoformulations on the overall cellular viability in comparison with the particle-free active compound (Figure 4).

In our previous work, we checked that PNPs did not affect MCF-7 cell viability, although a curcumin-based PLGA nanocarrier was efficiently able to inhibit the overall cellular growth in a dose- and time-dependent manner.[19] In the present study, MCF-7 cells were exposed up to 72 h within both ASC-J9 and P−ASC-J9 at three increasing concentrations (5, 10, and 20 μM). The assay showed an almost identical dose- and time-dependent behavior toward the cellular viability, thus suggesting a relevant cytotoxic activity of the active compound upon its efficient release inside the cellular environment (Figure 4A,C). It should be emphasized that the encapsulation of ASC-J9 in PLGA nanoparticles led to a relevant decrease of cellular proliferation even at the minimal concentration of ASCJ-9 (5 μM) tested; this fact ameliorates the pharmacological profile of ASC-J9 and, moreover, the possibility to use actively this compound at lower concentrations. Our result finds confirmations in similar experiments performed by other authors,[25,41] in which a broad range of artificial curcuminoids were tested within MCF-7 and other breast cancer cells to calculate their IC_{50} concentration.

With the aim to correlate their toxicity toward breast cancer and non-cancerous cells, estrogen-dependent healthy cells were exposed to P−ASC-J9 and ASC-J9 in parallel. Therefore, we performed MTT assay using a fibroblast 3T3-L1 cell line expressing the estrogen receptor (Figure 4B,D). Although we have surprisingly noticed a significant decrease of cell viability during the first 24 h of exposure, this value was slightly recovered over time, for the whole range of concentrations tested (Figure 4B), in contrast to what was observed in the MCF-7 cell line.

Once a cytotoxic effect was observed, we decided to check the propensity of our nanoformulation to be internalized inside the cellular environment. To this aim, PNPs were first loaded with hydrophobic coumarin-6 and confocal laser scanning microscopy images were acquired to follow the time-dependent compartmentalization inside the cells (Figure S10 in the Supporting Information). In this experiment, ASC-J9 was initially replaced by this dye because ASC-J9 exhibits a poor fluorescent intensity *in vitro* and the poor resolution of related images did not allow us to obtain a sufficient outcome. To better verify the cellular internalization of P−ASC-J9, we took advantage of the typical Raman spectra of ASC-J9 (as illustrated in Figure 2) to monitor the internalization of P−ASC-J9 by means of label-free confocal Raman imaging (Figure 5).

Raman images of cells (Figure 5 and Figure S13 in the Supporting Information) were obtained by integration of the Raman bands around 1450 cm^{-1}, assigned to proteins and lipids (C−H deformation) and mostly representing the cytoplasm (red in Figure 5A), the Raman bands around 1300 cm^{-1} related to fatty acids (CH_2 vibration) and generally colocalized with intracellular vesicles (green, Figure 5B), and the Raman band around 788 cm^{-1} assigned to DNA (O−P−O backbone stretch) representing the nucleus (blue, Figure 5C). Afterward, the presence of the reference Raman spectrum of P−ASC-J9 (Figure 2) was verified and localized over the entire cell area by classical least-squares (CLS) spectral matching analysis (Figure 5E and Figure S13 in the Supporting Information). The results of this analysis demonstrate that P−ASC-J9 were efficiently internalized by MCF-7 cells after 24 h of incubation. ASC-J9 bands, in particular those around 1158, 1597, and 1635 cm^{-1} (Figure 2), are mostly localized in the perinuclear region and sometimes in the nuclear region. Moreover, in some positions of the cell, these typical ASC-J9 bands and the band related to intracellular vesicles colocalized (Figure 5F), indicating that ASC-J9 was transported or accumulated in intracellular vesicles, thus suggesting a possible involvement of a controlled endosomal pathway for the internalization of P−ASC-J9. Untreated cells were analyzed in the same way as negative control (Figure S14 in the Supporting Information).

In order to explore the ASC-J9 and P−ASC-J9 cytotoxic activity, we investigated the causes of the decrease of MCF-7 viability. Therefore, we carried out a study of the apoptotic level in the MCF-7 cellular population using an Annexin-V-PE-Cy5 specific assay. This test is based on the observation that, in many cell types, the phospholipid phosphatidylserine (PS) could translocate from the inner face of plasma membrane to the cell surface during the early stage of apoptosis.[42] Once on the cell surface, PS can be easily detected by a simple staining with a fluorescent conjugate of Annexin V, a protein that possesses a strong natural affinity for PS. ASC-J9 and P−ASC-J9 (5, 10, and 20 μM) were incubated with MCF-7 cells for 3 and 24 h. Annexin V exposure on cellular surface was checked by flow cytometry (Figure 6).

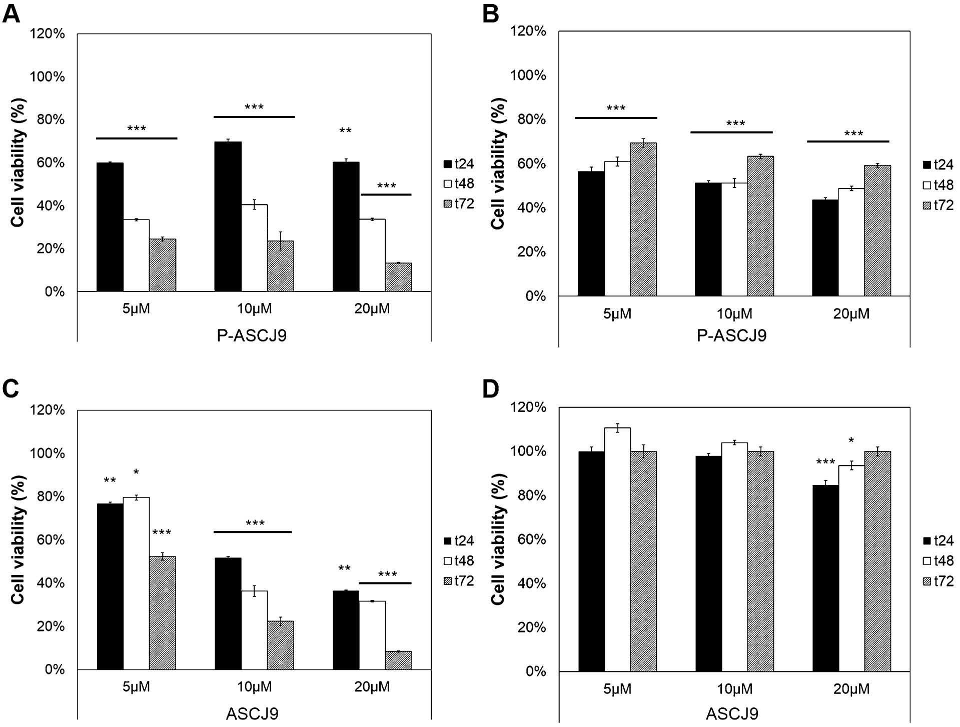

Figure 4. MTT assay on breast cancer cells. Effects on cell proliferation of MCF-7 (A, C) and 3T3-L1 (B, D) in the presence of P−ASC-J9 and free ASC-J9 (5, 10, and 20 μM) at different times, as indicated. Untreated cells represent 100% of viability. Values are means ± SD of three independent sets of experiments. Samples show statistical differences from control at $p < 0.5$ (*), 0.01 (**), and 0.001 (***).

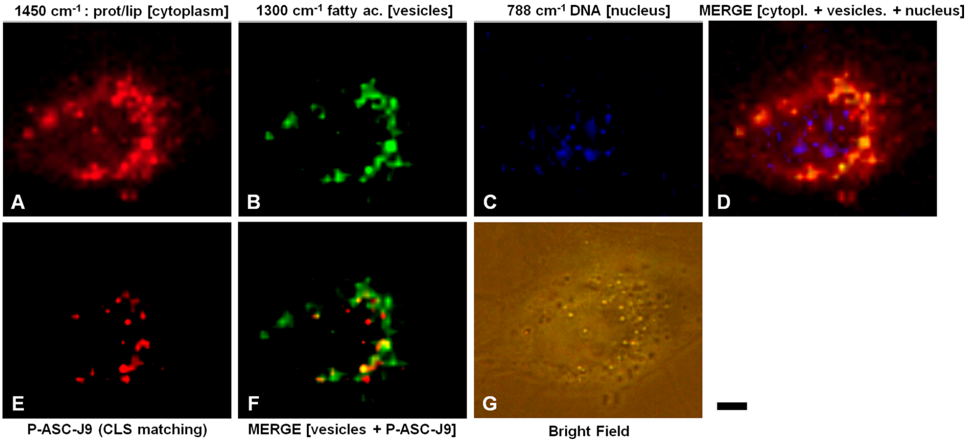

Figure 5. Confocal Raman imaging of MCF-7 cells treated with P−ASC-J9. After treating cells with P−ASC-J9 for 24 h, Raman images were obtained integrating a specific Raman band of interest: 1450 cm^{-1}, C−H groups in both proteins and lipids, related to cytoplasm (red, panel A); 1300 cm^{-1}, $-CH_2$ of fatty acids, mostly concentrated in intracellular vesicles (green, panel B); 788 cm^{-1}, O−P−O in DNA, related to nucleus (blue, panel C). Merging of bands described in panels A (cytoplasm), B (intracellular vesicles), and C (DNA) (panel D). Cellular regions related to the presence of ASC-J9 Raman bands (red, panel E); merging of bands described in panel B (intracellular vesicles) and ASC-J9 of panel E (ASC-J9), in yellow the positions where the two signals colocalize (panel F); bright field (panel G). Scale bar = 4 μm for all images.

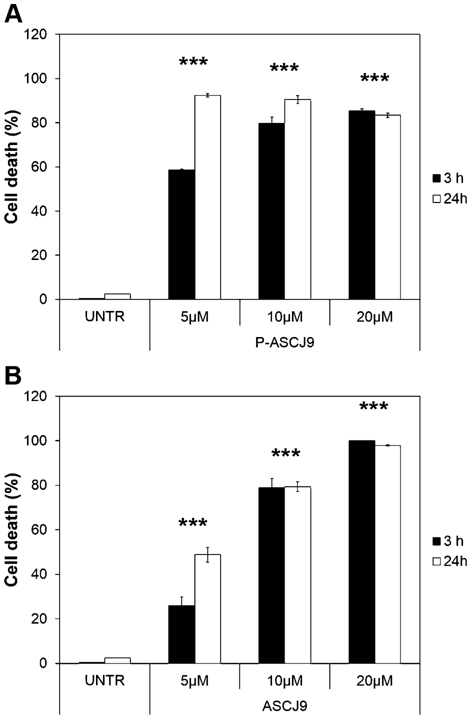

Figure 6. Cell death analysis. Percentage of apoptotic MCF-7 cells treated with different concentrations of P−ASC-J9 (A) and free ASC-J9 (B) for 3 and 24 h. Data are represented as mean ± SD of three independent experiments, $p < 0.001$ (***) vs untreated cells.

The effect of P−ASC-J9 (Figure 6A) is more evident compared to the pure compound (Figure 6B), even at the lowest concentration of 5 μM. These data suggest that the decrease of the overall MCF-7 cellular viability is mainly due to apoptotic events caused by the presence of ASC-J9. We hypothesized that ASC-J9 exploited the same pathway observed for the growth inhibition of prostate cancer cells.[43] In prostate cancer, ASC-J9 was assumed to bind and degrade androgen receptor, thus suppressing cell growth and further leading to their apoptosis. Analogously, in this case, ASC-J9 is supposed to be involved in blocking the estrogen receptor of MCF-7, consequently leading to an apoptotic event. However, as a thorough disclosure of the mechanism of action was not strictly related to the goal of this work, further investigations would be necessary in the future to find confirmation to our hypothesis.

P−ASC-J9 Induces Cell Cycle Arrest. Once assessed that particle-free ASC-J9 and its analogue encapsulated into PLGA could induce apoptotic events in MCF-7 cells, we tried to investigate their effect on the cell cycle. Indeed, we had evidence that similar curcumin-PLGA nanovectors were able to inhibit MCF-7 proliferation by blocking the cell cycle in G2/M phase.[19] Our idea was to find if, in this case, a relevant block of cell cycle could be added to apoptotic events previously observed. Actually, we did not find any references about the investigation of this effects as strictly correlated to ASC-J9 activity. Therefore, this study provides new information to elucidate the molecular mechanism of action of the drug toward this cancer cell line. MCF-7 cells were treated up to 72 h with different concentrations of P−ASC-J9 (Figure 7 and Figure S11 in the Supporting Information) and ASC-J9 (Figure S12 in the Supporting Information).

The analysis involves the labeling with propidium iodide, a popular red-fluorescent nuclear and chromosome counterstain. This compound is able to interpose itself between double stranded DNA, so that DNA content could be quantitatively analyzed by flow cytometry in each phase of the cell cycle. The DNA content of nanoparticle-treated MCF-7 cells was compared with a cell population of untreated cells for the whole time of incubation. DNA analysis was repeated every 24 h of exposure. As hypothesized, results show that, at the highest dosage of P−ASC-J9 (20 μM), the nanoparticle exposure rises to a significant accumulation of cells in G2/M phase from 16.5% after 24 h to 35.7% after 72 h (Figure 7A−C). In contrast, the behavior of the G2/M phase of untreated cells remains essentially unaltered (Figure 7D). This effect reflects the treatment with ASC-J9 at equal nanoparticle concentrations (20 μM) (Figure S11 in the Supporting Information), thus confirming that the effect was correlated to the activity of ASC-J9, timely released from the nanovector.

Implications in Intracellular ROS Levels. Free radicals are highly reactive chemical species that have the potential to harm cells. They are naturally formed in the body and control many cellular processes. At high concentrations, however, free radicals can be hazardous for all major components of cells, including DNA, proteins, and cell membranes.[44] In particular, cellular DNA damage may play a role in cancer cell development. Intracellular free radicals, which usually contain oxygen and thus are also referred to as “reactive oxygen species” (ROS), are the most common type of radicals produced in living tissues. ROS are normally generated by tightly regulated enzymes, such as NADPH oxidase isoforms; their overproduction (arising either from mitochondrial electron-transport chain or excessive stimulation of NADPH) often results in an oxidative stress. This deleterious process might be an important mediator in damaging cell structures. In contrast, beneficial effects of ROS occur at low/moderate concentrations, involving physiological roles in cellular defense against infectious agents and within the function of a number of cellular signaling pathways.[45]

The antioxidant effect is believed to be responsible for many biological activities of curcuminoids, and it is strictly related to their chemical structures. According to this, in previous works a plethora of different substituted curcumin analogues were investigated to explore the possibility that the target compounds maintained the antioxidant activity to eliminate free radicals.[33,46] For example, curcumin showed potent radical-scavenging activity, mainly attributed to its free phenoxyl group, whereas nonphenolic curcuminoids failed to reduce the amount of radicals even at high concentrations.[46] As this behavior is strictly related to their chemical structure, we evaluated the ability of ASC-J9 and of P−ASC-J9 to scavenge stable 2,2-diphenyl-1-picrylhydrazyl (DPPH) radical *in vitro*. DPPH assay is a widely used and accurate method to evaluate antioxidant activity.[33] Hence, we tried to correlate the result obtained with drug activity toward intracellular ROS levels, due to their implication in cell survival, as mentioned previously (Figure 8).

In our study, the radical−scavenging activity of 10 μM ASC-J9, P−ASC-J9, PNPs, and curcumin (as positive control) was evaluated by monitoring the reduction of light absorption at 520 nm by DPPH radical, upon reaction in methanol solution with our compounds in a time window between 1 and 48 h (Figure

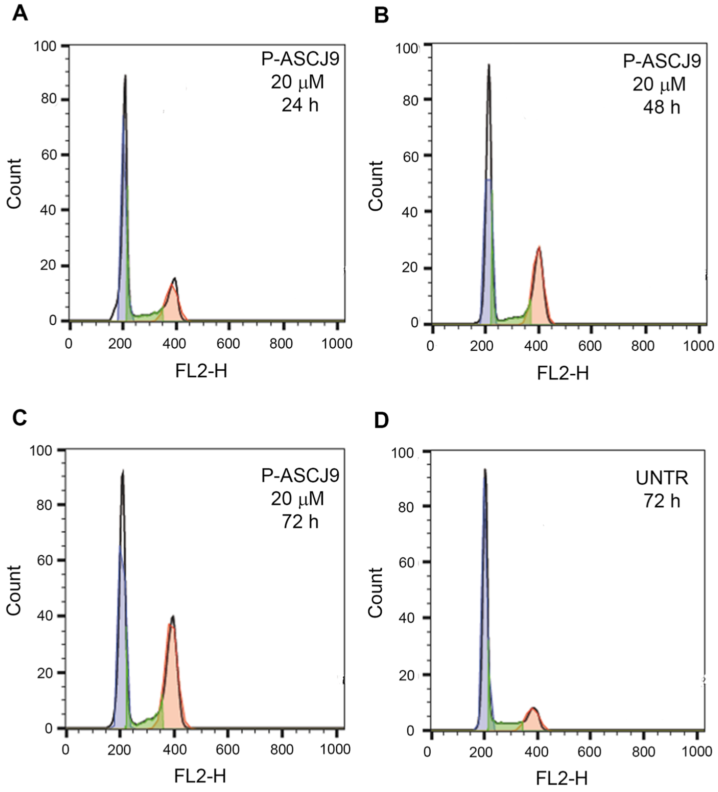

Figure 7. Cell cycle analysis. (A–C) Cell counts in each phase of cell cycle (blue gate = G0/G1; green gate = S; red gate = G2/M) versus DNA content (FL2-H) of MCF-7 treated with 20 μM P–ASC-J9 at 72 h. (D) Cell cycle analysis of untreated cells.

8A). As expected, ASC-J9 did not show any antioxidant activity because phenolic groups are completely methylated, while curcumin was able to decrease more than 50% DPPH radicals after 48 h. Interestingly, PNPs and P–ASC-J9 possessed similar but only small amount of scavenging activity (nearby 10%) after a few hours of incubation, but these values did not increased critically within the following 2 days. We hypothesized that this behavior could be related to the polyol composition of the polymer, which could interact with DPPH.

Next, we assessed the intracellular ROS levels in the presence of PNPs, free ASC-J9, and P–ASC-J9 at different concentrations. Figure 8B illustrates that, when MCF-7 cells were exposed to P–ASC-J9 for 15 min, 1 h, and 4 h, the levels of ROS significantly increased compared to untreated cells. Free ASC-J9 did not alter ROS level, even if at 20 μM we noticed a mild increase suggesting that the poor bioavailability, due to the intrinsic hydrophobic character of the molecule, did not allow the drug to alter the levels of ROS in such a short time. This result confirmed that ASC-J9 does not possess antioxidant activity for MCF-7 breast cancer cells. In addition, the oxidative stress, generated by the ASC-J9 efficient internalization with PLGA nanoparticles, triggered the degeneration of cancer cells and, together with the other cytotoxic effects observed, led to cell death.

■ CONCLUSIONS

PLGA is a biocompatible member of the aliphatic polyester family of biodegradable polymers. For this reason, it has long been a fashionable choice for drug delivery applications, particularly since it has been FDA-approved for administration in humans under different pharmaceutical formulations. In this context, PLGA-based nanovectors present well-documented advantages for drug delivery purposes, as their self-assembled matrix enhances drug stability and protection from degradation induced by the external environment. Moreover, nanoparticles can easily penetrate cancer tissues through the “enhanced permeation and retention” (EPR) effect; in this way, the sustained release of the cargo from the polymer matrix could enhance therapies improving the drug pharmacodynamic profiles. In this paper, we have encapsulated the artificial curcuminoid ASC-J9 in spherical PLGA nanoparticles, investigating their properties and release kinetics *in vitro* and studying the effects of the sustained release in breast cancer cells. In literature, several works have carried out the clinical utilization of ASC-J9 for the treatment of several estrogen- and androgen-receptor mediated diseases both *in vitro* and *in vivo*. Despite this fact, no evidence about its encapsulation in PLGA nanoparticles for breast cancer therapy have been found so far. This study demonstrates how PLGA nanospheres are able to efficiently release ASC-J9 intracellularly inducing time- and dose-depend-

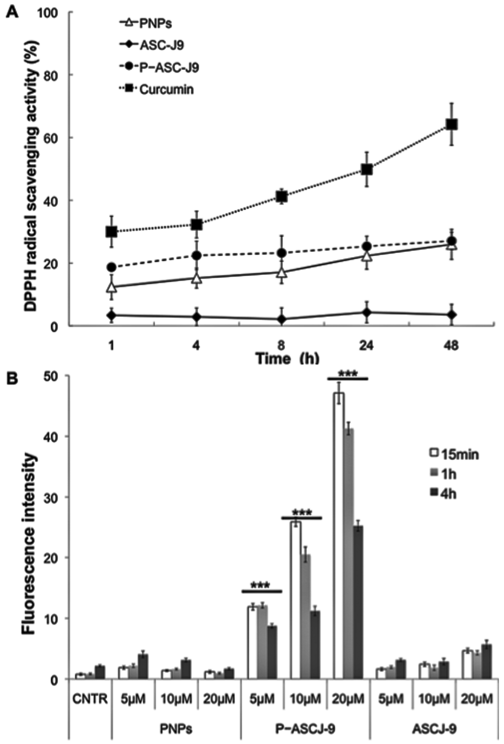

Figure 8. DPPH radical-scavenging activity and intracellular ROS levels. (A) DPPH radical scavenging activity after treatment with 10 μM of ASC-J9, (tilted squares, solid line) and corresponding P–ASC-J9 (circles, dashed line), PNPs (triangles, solid line), and 10 μM curcumin (squares, dotted line) as a positive control. Data are expressed as relative % of free radical scavenged respect to DPPH untreated samples. (B) MCF-7 cells were labeled with 25 μM DCFDA, cultured with PNPs, free ASC-J9, and P–ASC-J9, and then analyzed on a fluorescent plate reader. Results are expressed as mean ± SD for three replicates. $p < 0.001$ (***) vs untreated cells.

ent inhibition of estrogen-dependent MCF-7 cancer cells. The antiproliferative effect is induced by a G2/M cell cycle arrest and apoptosis even at low drug concentrations; in addition, a high level of ROS was observed in response to the cell treatment with ASC-J9-bearing PLGA nanoparticles (P–ASC-J9). The intracellular release was assessed using a combination of techniques, including confocal laser scanning microscopy performed on a dye-enriched drug analogue and a properly optimized Raman imaging, the latter now emerging as a useful tool to localize poorly fluorescent nanoconstructs inside the cellular compartment.

This study clearly indicates how PLGA-based nanoformulation could strongly improve the ASC-J9 administration for the treatment of estrogen-dependent cancer diseases, as nowadays several hurdles are obstructing its clinical employment due to a poor bioavailability of this molecule.

■ ASSOCIATED CONTENT

Ⓢ Supporting Information

Experimental details, dynamic light scattering and ζ-potential, fluorescence spectra, *in vitro* drug release kinetics, toxicity and cell cycle assays, confocal images, and confocal Raman images. This material is available free of charge via the Internet at http://pubs.acs.org.

■ AUTHOR INFORMATION

Corresponding Authors

*Phone: +39 02 64483302. Fax: +39 02 64483565. E-mail: davide.prosperi@unimib.it. Website: http://www.nanobiolab.btbs.unimib.it.
*Phone: +39 02 40308533. Fax: +39 02 4048919. E-mail: cmorasso@dongnocchi.it. Website: http://www.labion.eu.

Author Contributions

§P.V. and L.P. contributed equally to the work.

Notes

The authors declare no competing financial interest.

■ ACKNOWLEDGMENTS

This work was supported by Fondazione Regionale per la Ricerca Biomedica (FRRB), NanoMeDia Project (Regione Lombardia and "L. Sacco" Hospital), and Cariplo Foundation ("The MULAN program", Project N. 2011-2096). L.P. acknowledges a research fellowship of Fondazione "Romeo ed Enrica Invernizzi" and CMENA (University of Milan). A special mention is dedicated to Dr. Luca Palugan (Department of Pharmaceutical Sciences, University of Milan, Italy) for his valuable help and professional suggestions in drug release kinetics.

■ REFERENCES

(1) Ananthakrishnan, P.; Balci, F. L.; Crowe, J. P. Optimizing surgical margins in breast conservation. *Int. J. Surg. Oncol.* **2012**, *2012*, 585670.

(2) Chan, C. T.; Metz, M. Z.; Kane, S. E. Differential sensitivities of trastuzumab (Herceptin)-resistant human breast cancer cells to phosphoinositide-3 kinase (PI-3K) and epidermal growth factor receptor (EGFR) kinase inhibitors. *Breast Cancer Res. Treat.* **2005**, *91*, 187–201.

(3) Gianni, L.; Lladò, A.; Bianchi, G.; Cortez, J.; Kellokumpu-Lehtinen, P. L.; Cameron, D. A.; Miles, D.; Salvagni, S.; Wardley, A.; Goeminne, J. C.; Hersberger, V.; Baselga, J. Open-label, phase II, multicenter, randomized study of the efficacy and safety of two dose levels of Pertuzumab, a human epidermal growth factor receptor 2 dimerization inhibitor, in patients with human epidermal growth factor receptor 2-negative metastatic breast cancer. *J. Clin. Oncol.* **2010**, *28*, 1131–1137.

(4) Block, M.; Gründker, C.; Fister, S.; Kubin, J.; Wilkens, L.; Mueller, M. D.; Hemmerlein, B.; Emons, G.; Günthert, A. R. Inhibition of the AKT/mTOR and erbB pathways by gefitinib, perifosine and analogs of gonadotropin-releasing hormone I and II to overcome tamoxifen resistance in breast cancer cells. *Int. J. Oncol.* **2012**, *41*, 1845–1854.

(5) Wang, H.; Vo, T.; Hajar, A.; Li, S.; Chen, X.; Parissenti, A. M.; Brindley, D. N.; Wang, Z. Multiple mechanisms underlying acquired resistance to taxanes in selected docetaxel-resistant MCF-7 breast cancer cells. *BMC Cancer* **2014**, *14*, 14–37.

(6) Chen, J.; Lu, L.; Feng, Y.; Wang, H.; Dai, L.; Li, Y.; Zhang, P. PKD2 mediates multi-drug resistance in breast cancer cells through modulation of P-glycoprotein expression. *Cancer Lett.* **2011**, *300*, 48–56.

(7) Kievit, F. M.; Wang, F. Y.; Fang, C.; Mok, H.; Wang, K.; Silber, J. R.; Ellenbogen, R. G.; Zhang, M. Doxorubicin loaded iron oxide nanoparticles overcome multidrug resistance in cancer in vitro. *J. Controlled Release* **2011**, *152*, 76–83.

(8) Yan, Y.; Bjoernmalm, M.; Caruso, F. Particle carriers for combating multidrug-resistant cancer. *ACS Nano* **2013**, *7*, 9512−9517.

(9) Eldar-Boock, A.; Polyak, D.; Scomparin, A.; Satchi-Fainaro, R. Nano-sized polymers and liposomes designed to deliver combination therapy for cancer. *Curr. Opin. Biotechnol.* **2013**, *24*, 682−689.

(10) Akther, S.; Ahmad, I.; Ahmad, M. Z.; Ramazani, F.; Singh, A.; Rahman, Z.; Ahmad, F. J.; Storm, G.; Kok, R. J. Nanomedicines as cancer therapeutics: current status. *Curr. Cancer Drug Targets* **2013**, *13*, 362−368.

(11) Cheng, R.; Meng, F.; Deng, C.; Klok, H. A.; Zhong, Z. Dual and multi-stimuli responsive polymeric nanoparticles for programmed site-specific drug delivery. *Biomaterials* **2013**, *34*, 3647−3657.

(12) Mukerjee, A.; Ranjan, A. P.; Vishwanatha, J. K. Combinatorial nanoparticles for cancer diagnosis and therapy. *Curr. Med. Chem.* **2012**, *19*, 3714−3721.

(13) Elsabathy, M.; Wooley, K. L. Design of polymeric nanoparticles for biomedical delivery applications. *Chem. Soc. Rev.* **2012**, *41*, 2545−2561.

(14) Laquintana, V.; Denora, N.; Lopalco, A.; Lopedota, A.; Cutrignelli, A.; Lasorsa, F. M.; Agostino, G.; Franco, M. Translocator protein ligand−PLGA conjugated nanoparticles for 5-fluorouracil delivery to glioma cancer cells. *Mol. Pharmaceutics* **2014**, *11* (3), 859−871.

(15) Verderio, P.; Avvakumova, S.; Alessio, G.; Bellini, M.; Colombo, M.; Galbiati, E.; Mazzucchelli, S.; Avila, J. P.; Santini, B.; Prosperi, D. Delivering Colloidal Nanoparticles to Mammalian Cells: A Nano−Bio Interface Perspective. *Adv. Healthcare Mater.* **2014**, DOI: 10.1002/adhm.201300602.

(16) Acharya, S.; Sahoo, S. K. PLGA nanoparticles containing various anticancer agents and tumour delivery by EPR effect. *Adv. Drug Delivery Rev.* **2011**, *63*, 170−183.

(17) Dinarvand, R.; Sepehri, N.; Manoochehri, S.; Rouhani, H.; Atyabi, F. Polylactide-co-glycolide nanoparticles for controlled delivery of anticancer agents. *Int. J. Nanomed.* **2011**, *6*, 877−895.

(18) Danhier, F.; Ansorena, E.; Silva, J. M.; Coco, R.; LeBreton, A.; Preat, V. PLGA-based nanoparticles: an overview of biomedical applications. *J. Controlled Release* **2012**, *161*, 505−522.

(19) Verderio, P.; Bonetti, P.; Colombo, M.; Pandolfi, L.; Prosperi, D. Intracellular drug release from curcumin-loaded PLGA nanoparticles induces G2/M block in breast cancer cells. *Biomacromolecules* **2013**, *14*, 672−682.

(20) Asher, G. N.; Spelman, K. Clinical utility of curcumin extract. *Altern. Ther. Health Med.* **2013**, *19*, 20−22.

(21) Kanai, M.; Otsuka, Y.; Otsuka, K.; Sato, M.; Nishimura, T.; Mori, Y.; Kawaguchi, M.; Hatano, E.; Kodama, Y.; Matsumoto, S.; Murakami, Y.; Imaizumi, A.; Chiba, T.; Nishihira, J.; Shibata, H. A phase I study investigating the safety and pharmacokinetics of highly bioavailable curcumin (Theracurmin) in cancer patients. *Cancer Chemother. Pharmacol.* **2013**, *71*, 1521−1530.

(22) Anand, P.; Kunnumakkara, A. B.; Newman, R. A.; Aggarwal, B. B. Bioavailability of curcumin: problems and promises. *Mol. Pharmaceutics* **2007**, *4*, 807−818.

(23) Yamashita, S.; Lai, K. P.; Chuang, K. L.; Xu, D.; Miyamoto, H.; Tochigi, T.; Pang, S. T.; Li, L.; Arai, Y.; Kung, H. J.; Yeh, S.; Chang, C. ASC-J9 suppresses castration-resistant prostate cancer growth through degradation of full-length and splice variant androgen receptors. *Neoplasia* **2012**, *14*, 74−83.

(24) Yang, Z.; Chang, Y. J.; Yu, I. C.; Yeh, S.; Wu, C. C.; Miyamoto, H.; Merry, D. E.; Sobue, G.; Chen, L. M.; Chang, S. S.; Chang, C. ASC-J9 ameliorates spinal and bulbar muscular atrophy phenotype via degradation of androgen receptor. *Nat. Med.* **2007**, *13*, 348−353.

(25) Qiu, X.; Du, Y.; Lou, B.; Zuo, Y.; Shao, W.; Huo, Y.; Huang, J.; Yu, Y.; Zhou, B.; Du, J.; Fu, H.; Bu, X. Synthesis and Identification of New 4-Arylidene Curcumin Analogues as Potential Anticancer Agents Targeting Nuclear Factor-κB Signaling Pathway. *J. Med. Chem.* **2010**, *53*, 8260−8273.

(26) Soule, H. D.; Vasquez, J.; Long, A.; Albert, S.; Brennan, M. A human cell line from a pleural effusion derived from a breast carcinoma. *J. Natl. Cancer Inst.* **1973**, *51*, 1409−1416.

(27) Horwitz, K. B.; Costlow, M. E.; McGuire, W. L. MCF-7; a human breast cancer cell line with estrogen, androgen, progesterone, and glucocorticoid receptors. *Steroids* **1975**, *26*, 785−795.

(28) Daschner, P. J.; Ciolino, H. P.; Plouzek, C. A.; Yeh, G. C. Increased AP-1 activity in drug resistant human breast cancer MCF-7 cells. *Breast Cancer Res. Treat.* **1999**, *53*, 229−240.

(29) Doyle, L. A.; Yang, W.; Abruzzo, L. V.; Krogmann, T.; Gao, Y.; Rishi, A. K.; Ross, D. D. A multidrug resistance transporter from human MCF-7 breast cancer cells. *Proc. Natl. Acad. Sci. U.S.A.* **1998**, *95*, 15665−15670.

(30) Keum, C. G.; Noh, Y. W.; Baek, J. S.; Lim, J. H.; Hwang, C. J.; Na, Y. G.; Shin, S. C.; Cho, C. W. Practical preparation procedures for docetaxel-loaded nanoparticles using polylactic acid-co-glycolic acid. *Int. J. Nanomed.* **2011**, *6*, 2225−2234.

(31) D'Souza, S. S.; DeLuca, P. P. Methods to assess in vitro drug release from injectable polymeric particulate systems. *Pharm. Res.* **2006**, *23*, 460−474.

(32) Costa, P.; Lobo, J. M. S. Modeling and comparison of dissolution profiles. *Eur. J. Pharm. Sci.* **2001**, *13*, 123−133.

(33) Kim, M. K.; Jeong, W.; Kang, J.; Chong, Y. Significant enhancement in radical-scavenging activity of curcuminoids conferred by acetoxy substituent at the central methylene carbon. *Bioorg. Med. Chem.* **2011**, *19*, 3793−3800.

(34) Fuchs, J. R.; Pandit, B.; Bhasin, D.; Etter, J. P.; Regan, N.; Abdelhamid, D.; Li, C.; Lin, J.; Li, P. K. Structure-activity relationship studies of curcumin analogues. *Bioorg. Chem. Med. Lett.* **2009**, *19*, 2065−2069.

(35) Pabon, H. J. J. A synthesis of curcumin and related compounds. *Recl. Trav. Chim. Pays-Bas* **1964**, *83*, 379−386.

(36) Balasubramanyam, M. J. Molecular orbital basis for yellow curry spice curcumin's prevention of Alzheimer's disease. *J. Agric. Food Chem.* **2006**, *54*, 3512−3520.

(37) Payton, F.; Sandusky, P.; Alworth, P. L. NMR study of the solution structure of curcumin. *J. Nat. Prod.* **2007**, *70*, 143−146.

(38) Krishna Mohan, P. R.; Sreelakshmi, G. V.; Muraleedharan, C. V.; Joseph, R. Water soluble complexes of curcumin with cyclodextrins: Characterization by FT-Raman spectroscopy. *Vib. Spectrosc.* **2012**, *62*, 77−84.

(39) Wang, Y.; Pan, M.; Cheng, A.; Lin, L.; Ho, Y.; Hsieh, C.; Lin, J. Stability of curcumin in buffer solutions and characterization of its degradation products. *J. Pharm. Biomed. Anal.* **1997**, *15*, 1867−1876.

(40) Tønnesen, H. H. Chemistry of curcumin and curcuminoids. In *Phenolic compounds in food and their effects on Health I*; Ho, C., Lee, C., Huang, M., Eds.; ACS Symposium Series; American Chemical Society: Washington, DC, 1992; pp 143−153.

(41) Ohtsu, H.; Itokawa, H.; Xiao, Z.; Su, S.; Shih, C.; Chiang, T.; Chang, E.; Lee, Y.; Chiu, S.; Chang, C.; Lee, K. Antitumor agents 222. Synthesis and anti-androgen activity of new diarylheptanoids. *Bioorg. Med. Chem.* **2003**, *11*, 5083−5090.

(42) Koopman, G.; Reutelingsperger, C. P.; Kujten, G. A.; Keehnen, R. M.; Pals, S. T.; van Oers, M. H. Annexin V for flow cytometric detection of phosphatidylserine expression on B cells undergoing apoptosis. *Blood* **1994**, *84*, 1415−1420.

(43) Jiang, Q.; Yeh, S.; Wang, X.; Xu, D.; Zhang, Q.; Wen, X.; Xia, S.; Chang, C. Targeting androgen receptor leads to suppression of prostate cancer via induction of autophagy. *J. Urol.* **2012**, *188*, 1361−1368.

(44) Valko, M.; Leibfritz, D.; Moncol, J.; Cronin, M. T.; Mazur, M.; Telser, J. Free radicals and antioxidants in normal physiological functions and human disease. *Int. J. Biochem. Cell Biol.* **2007**, *39*, 44−84.

(45) Hancock, J. T.; Desikan, R.; Neill, S. J. Role of reactive oxygen species in cell signaling pathways. *Biochem. Soc. Trans.* **2001**, *29*, 345−350.

(46) Fang, X.; Fang, L.; Gou, S.; Cheng, L. Design and synthesis of dimethylaminomethyl-substituted curcumin derivatives/analogues: Potent antitumor and antioxidant activity, improved stability and aqueous solubility compared with curcumin. *Bioorg. Med. Chem. Lett.* **2013**, *23*, 1297−1301.

Chapter 2

Engineered gold nanoparticles targeted to mesenchymal cells from patients with bronchiolitis obliterans syndrome do not elicit inflammatory response and can be safely inhaled in rodents

2.1. Introduction

2.1.1 Bronchiolitis obliterans syndrome

Bronchiolitis obliterans syndrome (BOS) is the most frequent chronic lung allograft dysfunction phenotype affecting up to 70% of recipients who survive 5 years after surgery and remains the major impediment to long-term success after lung transplantation. BOS diagnosis relies upon sustained (≥3 weeks) decline in expiratory flow rates, provided that other pulmonary dysfunctions have been excluded; its classification upon the percentage of reduction of forced expiratory volume (FEV), ranging from BOS 0 to BOS 3 rates (Table 1).[1,2,3,4]

Table 1: BOS classification system.[1]

	2003 classification
BOS 0	FEV > 90% of baseline
BOS 0p	FEV 81-90% of baseline
BOS 1	FEV 66-80% of baseline
BOS 2	FEV 51-65% of baseline
BOS 3	FEV < 50%

Histologically, BOS is characterized by a patchy sub-mucosal fibrosis causing total occlusion of tracts of bronchiolar lumen and deterioration of graft function.[2,5] Unfortunately, this disease is very heterogeneous, varying both in timing of onset after transplantation and in aggressiveness of its clinical course. What accounts for this significant interindividual variation is not fully explained, but it is likely related to the range of insults and immunological mechanisms underlying the pathogenesis of BOS.[5] It is believed that the trigger of BOS is due to alloimmune (acute cellular rejection or lymphocytic bronchitis) and non-alloimmune (e.g., allograft infection or gastroesophageal reflux) dependent responses that act alone or in combination, but the rarity of BOS in patients without transplantation emphasizes the fundamental role of alloimmune reactivity.[1,5]

Plenty of studies on this pathology have provided evidence that chronic or recurrent exposure to inflammatory signals unbalances the innate and adaptive local responses against graft, neutrophils playing in particular a significant role in the pathogenesis of BOS.[6,7] The recruitment of these polymorphonuclear cells (PMNs) to the lung is due to the high level of Interleukin-8 (IL-8), the most potent neutrophil chemokine secreted by macrophages and by bronchial epithelium and pulmonary endothelial cells. Neutrophilic inflammation can further damage the epithelium, releasing reactive oxygen species (ROS), chemokines and metalloproteinases.[7,8] The link between innate and adaptive immune response are the active T helper type 17 cells (Th17) that secrete Interleukin-17 (IL-17), a potent inducer of IL-8 released by lung endothelial and epithelial cells so as to create a chemotactic gradient towards airways lumen does giving rise to a vicious circle.[6-9]

This inflammatory phase is ultimately followed by fibroblast accumulation in the bronchiolar tissue, which might stem from: (a) recruitment to the injured area of circulating precursors, such as fibrocytes, whose amount is increased in lung transplant recipients and could therefore contribute to the fibrotic process; (b) differentiation of airway epithelial cells to mesenchymal cells (MCs), thanks to the epithelial mesenchymal transition (EMT) process; and (c) amplification of a local pool of fibroblasts and MC precursors.[10] Lama and coworkers demonstrated that MCs can be isolated from bronchoalveolar lavage (BAL, fluid obtained by injecting saline into an entire region of the lung and then aspirating that saline) of lung transplanted patients, that express embryonic lung mesenchyme-associated transcription factors and moreover the measurements of BAL MCs is predictive for the development of BOS.[11] Although MCs proliferation and extracellular matrix deposition are physiological processes in the reparative course, they appear excessive and uncontrolled in transplanted lungs, thus leading to irreversible obliteration of airway lumen.[12,13]

Current standard BOS therapies are based on anti-inflammatory or immunosuppressive medications, like cyclosporine, azythromycin and methylprednisolone, for which one of the main problems is that functional diagnosis is made in an advanced stage of the disease, the so-called fibroproliferative stage.[14,15] For this reason, the most sensitive and useful approach could be the combination of immunosuppression and antimitogen action. A promising agent in this field is everolimus (EV), an inhibitor of mammalian target of rapamycin (mTOR), also endowed with potent immunosuppressive activities, which has been demonstrated to suppress the *in vitro* proliferation of fibroblasts isolated from BOS patients.[16,17,18]

Nevertheless, both therapeutic strategies (i.e., prevention of inflammatory phase and antiproliferative action) have shown poor clinical response, partly because of systemic drug toxicity and insufficient drug accumulation at target sites. The ultimate treatment of BOS remains therefore retransplantation.

2.1.2 Gold NPs

Gold NPs (GNPs) are among the most extensively studied nanomaterials due to their unique size-dependent electronic and optical properties combined with a great potential in a broad range of biomedical applications.[19,20] Indeed, GNPs exhibit multiple different properties of the gold core at the nanoscale, which render them suitable tools for medical imaging and therapy as contrast agents, targeted diagnostic tool, radio-/photo-thermal therapeutics. So they can be employed as drug/gene delivery vehicles.[21,22,23,24]

Hydrophobic GNPs are produced by chemical reduction of gold salts to colloidal gold in the presence of a capping ligand in non-polar solvents, thus obtaining highly stable NPs, usually ranging in size from 1 to 5 nm.[25] However, further surface functionalization is needed to ensure high biocompatibility and low cytotoxicity, which is normally obtained by amphiphilic coating with polyethylene glycol (PEG). This functionalization prevents nonspecific protein adsorption on NPs *in vivo*, undesired uptake by the reticuloendothelial system (RES) and prolonged half-life in the circulation.[26,27,28]

In addition, when targeting to specific cell types is required, antibodies, peptides, aptamers and small molecule can be easily attached to their surface with different methods.[29]

2.1.3 Aim of the work

In a previous work,[30] we designed a new nanovehicle-based treatment to specifically target MCs (Figure 2.1), with the purpose to administer them by the inhalatory route.

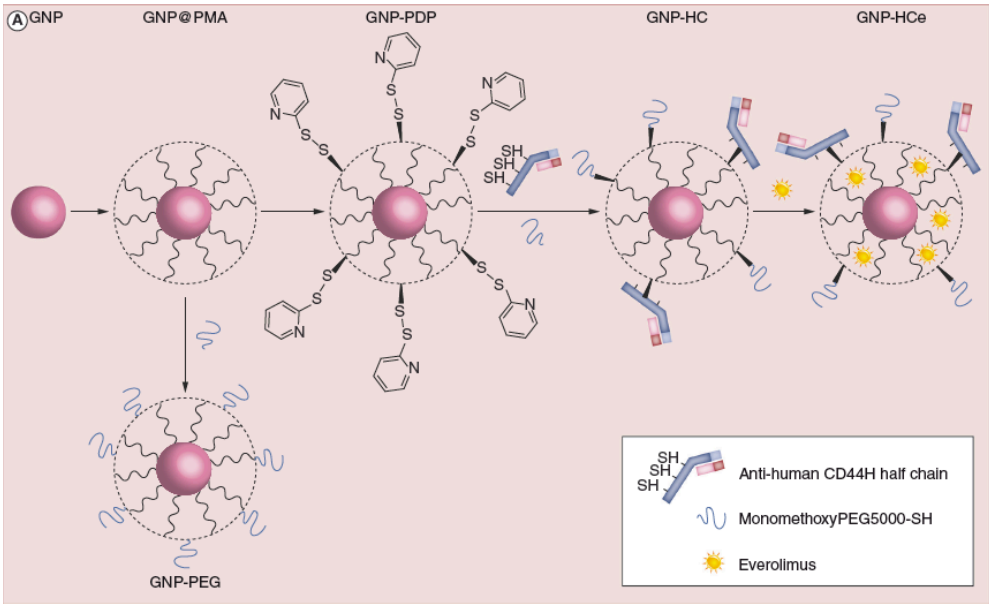

Figure 2.1. Synthesis of fully armed half-chain gold NPs with everolimus, and PEGylated gold NPs. Hydrophobic GNPs were synthesized and coated with an amphiphilic polymer PMA. The resulting GNP@PMA were functionalized with *N*-succinimidyl-3-[2-pyridyldithio]-propionate (GNP-PDPs). The thiol-reactive PDP functionalities were exploited for the immobilization of heavy-chain CD44 monoclonal antibodies (GNP-HC) labeled with Alexa® (Invitrogen; CA, USA) Fluor 488 dye. As a

control, we also synthesized fluorescently labeled, PEGylated GNPs. Finally, GNP-HCs were loaded with everolimus (GNP-HCe).[30]

To fulfill our aim, GNPs were loaded with EV in order to inhibit mTOR, leading an alteration in cell growth and metabolism of MCs (2.1.1). To make GNPs targeting more specific, we functionalized the NPs surface with a monoclonal antibody against CD44, a glycoprotein highly expressed by MC cells derived from BAL (Figure 2.2) and in fibroblast *foci* typically found in the lung tissue of BOS patients.

We demonstrated that GNPs targeted to MCs significantly inhibited their proliferation *in vitro* without affecting alveolar epithelial cell viability, thus enabling local treatment in BOS. However, taking into account that the trigger of BOS is an alteration in the inflammatory process, it is important to understand if our nanoconstructs could potentially enhance the activity of immune-effectors, increasing the inflammatory response and oxidative stress in BOS patients.

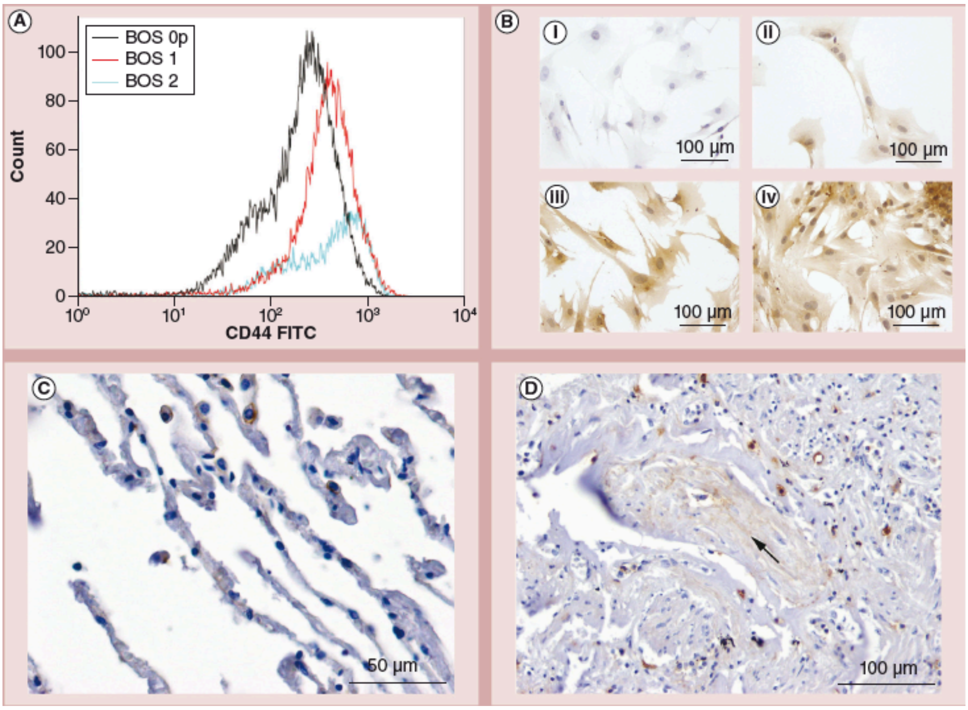

Figure 2.2. CD44 expression on mesenchymal cell surface, in normal and bronchiolitis obliterans syndrome epithelia. CD44 was detected by (A) flow cytometry and (B) immunocytochemistry on the three cell lines used in the experiments; (i) negative control, (ii) BOS 0 P, (iii) BOS 1 and (iv) BOS 2. Immunohistochemistry procedure demonstrated that (C) normal alveolar epithelia did not express CD44, (D) while cells invading bronchiolar lumen, indicated by the arrow, from a patient retransplanted for BOS, were positive to CD44 monoclonal antibody.[30]

For this reason, our aim was to determine the *in vitro* effect of drug-loaded GNPs on macrophages, neutrophils and lymphocytes activation by assessing different parameters such as cytokine secretion, cell apoptosis and ROS production. In addition, we studied the potential impact of NPs delivery by aerosolization on normal mice, evaluating their localization.

2.2 Materials and methods

2.2.1 NP preparation

Water-soluble GNPs functionalized with anti-human CD44 antibody half-chain and loaded with everolimus (GNP-HCe) were prepared according to a previously published protocol.[30] Briefly, 6 nm-diameter organic GNPs were synthesized following the Brust protocol[25] and transferred to water solution, whereby they were subjected to a coating procedure with the amphiphilic polymer (PMA) obtained by reaction of 75% reacting groups of poly(isobutylene-*alt*-maleic anhydride) with dodecylamine (GNP@PMA). GNP@PMA (500 μL of a 4 μM solution), were reacted with 2,2-(ethylenedioxy)bis(ethylamine) (EDBE, 80 μL 0.05 M in deionized water) in the presence of 1-Ethyl-3-(3-dimethylaminopropyl)carbodiimide (1 M EDC in deionized water, 20 μL) for 2 h. The resulting NPs were stirred for 4 h with 5 mg of N-succinimidyl-3-[2-pyridyldithio]-propionate (SPDP).

Next, the half chain of monoclonal anti-human CD44 (400 μg), obtained by reduction of the interchain disulfide bridges of the entire IgG, and MeO-PEG500-SH were added and incubated at room temperature for 1 h. Everolimus dissolved in ethanol (50 μL, 10 μg mL^{-1}) was added to 1 mg of the washed and collected GNP-HC solution and incubated overnight at 4 °C.

PEG-functionalized GNP were synthesized by reacting GNP@PMA (250 μL of 4 μM solution) with O-(2-aminoethyl)-O'-methyl-polyethylene glycol ($PEG2000\text{-}NH_2$, MW 2000, 27 μL in 0.1 M water) in the presence of 1.0 M EDC (9.5 μL) as previously reported[19]. Dye-labeled NPs were obtained using 0.5 M PMA labeled with Alexa Fluor-488 for cell treatment or with IR-820 dye for mice inhalation.

2.2.2 Cell isolation

Macrophages were isolated from patients' BAL by the adhesion procedure. Briefly, cells recovered from BALs were seeded in 24-well plates at concentration of 5×10^5 cells/well in RPMI medium containing 10% heat-inactivated Fetal Bovine Serum (FBS) for 2 h at 37 °C to allow macrophage adhesion. After isolation, macrophages were cultured in RPMI medium with 10% FBS and 1 U/L penicillin/streptomycin solution.

To isolate neutrophils and lymphocytes, we used peripheral blood of healthy donors and cultured in RPMI medium. In particular, neutrophils were isolated from buffy coat sample separated by gradient stratification with Lympholyte (Cedarlane Laboratories, Ontario, Canada) and $CD3^+$ T cells were purified by magnetic beads separation with $CD3^+$ T cells Isolation Kit (Miltenyi Biotec, Germany).

For all experiments 25μg mL^{-1} GNPs and 3 ng mL^{-1} everolimus
based on Kovarik et al 2006 work were used.[31]

2.2.3 NPs uptake

Uptake by macrophages, neutrophils and lymphocytes of functionalized (GNP-HC) and un-functionalized (GNP-PEG) NPs marked with Alexa Fluor-488, was evaluated by flow cytometry. Uptake of GNP-HC and GNP-PEG was evaluated after 2 h incubation at 37 °C in complete medium.

2.2.4 Viability and apoptosis assessment

Apoptosis rate was evaluated by Annexin-V (Molecular Probes, Life Technologies, Milan, Italy) by flow cytometry at 8 and 24 h after treatments with GNP-HC, GNP-HCe and EV. Neutrophils' apoptosis was assayed after 4 h of incubation.

MTT (3-(4,5-dimethylthiazol-2-yl)-2,5-diphenyltetrazolium bromide) assay (Sigma-Aldrich) was used to evaluate macrophage viability at 24, 48 and 72 h incubation and expressed as percentage of variation vs. untreated cells (100%).

2.2.5 IL-8, INF-γ, IL-17, IL-10 and elastase release

The experiments on macrophages were performed by incubating cells for 2 h with 25 μg/ml of antiCD44-functionalized NPs loaded (GNP-HCe) or not with everolimus (GNP-HC). The effect of NPs was assayed by evaluating viability and IL-8 release in both un-stimulated and stimulated macrophages. Stimulation of macrophages was obtained by adding to cells 0.01 mg/ml Lipopolysaccharides (LPS, Sigma-Aldrich) for 2 h, previously treated with NPs. IL-8 production by macrophages in the presence of GNP-HC and GNP-HCe was evaluated by the ELISA technique at 24 and 48 h after incubation with different NPs. All culture supernatants were collected and centrifuged at 1000 x g for 10 min to remove cell debris and stored at –80 °C until analysis.

The effect of GNP-HC and GNP-HCe on neutrophils was evaluated by quantifying elastase release into the culture medium by an enzymatic assay. Briefly, 2 x 10^7 neutrophils were treated with 5 μg/ml cytochalasin B (Sigma-Aldrich) for 10 min at room temperature. Afterwards, cells were seeded in a 96-well plate and treated for 20 min at 37°C with different NPs and N-Formyl-L-methionyl-L-leucyl-L-phenylalanine (FMLP, 10^{-4} M), as a positive control. The plate was then centrifuged at 1000 x g for 10 min at 4 °C and the supernatants were transferred in new wells previously filled with the substrate solution (N-Succinyl-Ala-Ala-Ala-p-nitroanilide, 1 mM in phosphate buffer). The plate was incubated for 1 h at 37 °C and the colorimetric reaction was read at 405 nm. The data were expressed as % vs. untreated neutrophils.

Isolated CD3$^+$ T lymphocytes were incubated with functionalized NPs (GNP-HC and GNP-HCe) evaluating the effect on the release of INF-γ, IL-17 and IL-10 in both un-stimulated and stimulated conditions. Stimulated lymphocytes were obtained by adding to the culture medium 0.15 mg/ml phytohaemagglutinin (PHA) before treating cells with NPs. For INF-γ, IL-17 and IL-10 detection, isolated lymphocytes were seeded in 24-wells plates and incubated in the presence of the selected NPs (GNP-HC and GNP-HCe) and analyzed by the ELISPOT procedure for INF-γ detection, evaluated at 24 h after incubation, and IL-10 and IL-17 dosage, performed after 48 h. Spots were counted by an image analyzer (A-EL-VIS, Hannover, Germany). As controls, in all experiments untreated cells and cells treated with standalone everolimus were used.

2.2.6 Identification and enumeration of CD3$^+$CD4$^+$, CD3$^+$CD8$^+$ populations and CCR7 expression

Isolated CD3$^+$ T lymphocytes were incubated with GNP-HC, GNP-HCe and EV alone for 72 h. Subsequently they were washed and immunodecorated with monoclonal antibodies (mAbs) against CD8, CD3, CD4 and CCR7 (Beckman Coulter) according to the manufacturer's instructions. The mAb were labeled with the fluorescent dyes PE-Texas Red, fluorescein isothiocyanate (FITC), allophycocyanin (APC) and phycoerythrin (PE), respectively. Cells were analyzed by a FACScan flow cytometer (Beckman Coulter) using forward- and side-scatter signals to establish the lymphocyte gate and exclude unwanted events from cell evaluation.

2.2.7 Reactive Oxygen Species (ROS) detection

ROS generation, in culture medium and inside the cells was detected at t_0 (baseline) and after 4 h of incubation with NPs for neutrophils or 24 and 48 h for macrophages by Electron Paramagnetic Resonance (EPR) spectroscopy (EPR spectrometer, Bruker, Germany) operating at the common X-Band microwave frequency (~9.8 GHz). For ROS trapping, culture medium and cells were incubated with 1 mM CMH (1-hydroxy-3-methoxycarbonyl-2,2,5,5-tetramethylpyrrolidine) probe prepared in Krebs-Hepes buffer (KHB) containing 25 µM deferroxamine methane-sulfonate salt (DF) chelating agent and 5 µM sodium diethyldithio-carbamate trihydrate (DETC) at pH 7.4. Spectra were recorded and analyzed by using a standard software (Win EPR 2.11 version) supplied by Bruker. Neutrophils were centrifuged (1000 rpm, 10 min), re-suspended in 250 µL of CMH probe (1:1) and incubated for 30 min at 37 °C. Macrophages were trypsinized, centrifuged (1000 rpm, 10 min), twice washed in PBS and re-suspended in 250 µl of PBS. An equal volume of CMH probe (1:1) was added and cells were incubated for 30 min at 37 °C. Afterwards, cell sample was frozen at -190 °C before being placed inside the cavity of the EPR spectrometer for data acquisition. Protocol adopted to detect ROS production rate in extracellular media was previously described (Mrakic-Sposta et al, 2012). [32]

2.2.7 Mitochondrial Membrane Potential assessment

Measurement of mitochondrial membrane potential ($\Delta\psi m$) was performed with the JC-1 tracker. JC-1 dye exhibits potential-dependent accumulation in mitochondria, indicated by a fluorescence emission shift from green (~529 nm) to red (~590 nm). Consequently, mitochondrial depolarization is indicated by a decrease in the red/green fluorescence intensity ratio, used as an indicator of cell health. Neutrophils and macrophages were plated at a density of

1 x 10^5 in 96-well black plates and incubated for 4 and 48 h respectively with GNP-HC and GNP-HCe. At the end of the treatment, 10 μl of JC-1 staining solution (JC-1 reagent diluted 1:10 in culture medium) were added to the cells. After rinsing with PBS, the plates were read using a fluorescent plate reader (Fluostar Omega, BMG Labtech GmbH, Ortenberg, Germany) with the excitation and emission wavelengths set respectively at 540 and 595 nm, for red fluorescence, and 485 and 540 nm for green fluorescence.

2.2.8 Mice strain and treatments

This study was conducted under EU guidelines for the care and use of laboratory animals in accordance with Italian and European legislation (D.lgs. 116/92, European Directives 86/609/EE for the protection of animals used in scientific and experimental studies and 2010-63UE) and was approved by Ethical Committee recognized from University of Pavia. Fifteen C57/BL6 mice were purchased from Charles River (Charles River laboratories, Lecco, Italy) and housed in polycarbonate cages for 10 days after arrival. Subsequently, mice were divided in three groups: the first composed by 4 mice living in normal conditions for 2 weeks; the second composed by 8 mice subjected to an aerosol treatment using a home-made aerosol trap for 2 weeks, 30 min/day with 50 μg/mouse of GNP-HCe (4 mice) or GNP-HC (4 mice) diluted in PBS. In the third group, three mice inhaled GNP-HC marked with IR-820 dye to assess NPs localization in lungs, kidneys, spleen and liver. At the end of the experiment, mice were anesthetized with intraperitoneal injection of 0.5 mg g^{-1} of Avertin (2, 2, 2-Tribromoethanol) and were sacrificed by cervical dislocation. The dose of NPs administered to mice by inhalation (50 μg/mice/inhalation) was chosen according to the *in vitro* data, in which we selected 25 μg/ml as the more effective concentration[30] and taking in account mice lung volume. The characteristics of inhaled NPs are reported in table 2.

Table 2. characteristics of inhaled NPs

Parameter	Value
Aerosol concentration (ng/cm^3)	50
Inhalation period (min)	30
Tidal volume (cm^3)	0.18
Breathing frequency (1/min)	165
NPs inhaled (µg/mL)	44.5
Inhaled volume (cm^3/30min)	891
Diameters of GNPs (nm)	47

2.2.9 Near-infrared light microscopy technology (NIR)

After sacrifice, mice treated with IR-820-labeled GNP-HC were perfused with cold PBS and then with 4% paraformaldehyde solution. Organs were removed and left for 24 h in paraformaldehyde. Then, tissues were rinsed in saline solution and dried. For relative quantification of signal intensity, images were obtained using the Odyssey® Infrared Imaging System (LI-COR Biosciences, Lincoln, NE, USA). Briefly, isolated organs were placed on the surface of the imager and high-resolution scans were performed with the following parameters: near-infrared 700 and near-infrared 800 scan intensity 3, resolution 21 µm, and focus 2.5 mm. For quantitative evaluation, five regions of interest was traced in the organs, and near-infrared 700 signal intensity values were recorded using Odyssey® software.

2.2.11 Transmission electron microscopy

Samples obtained from lungs of mice treated with GNP-HC were fixed by 2.5% glutaraldehyde in phosphate buffer. After three washes with the same buffer, the samples were post-fixed for 2 h with 1.5 % osmium tetroxide in phosphate buffer, dehydrated by a rising alcohol scale and included in epoxy resin. Ultrathin slices (70/80 nm) were cut and stained with uranyl acetate and lead citrate.

2.2.12 Statistical analysis

Statistical differences between untreated cells, cells treated with different NPs and everolimus alone were evaluated using ANOVA analysis. All analyses were carried out with the Graph Prism 5.0 statistical program. A P value < 0.05 was considered statistically significant.

2.3 Results and discussion

The use of colloidal NPs as drug delivery systems is particularly attractive for the possibility to combine diagnosis and specific target treatment to avoid excessive systemic toxicity and increase the therapeutic effectiveness. In this perspective, great attention has been addressed to gold NPs that have been considered "safe" colloids.[28]

The favorable outcome of lung transplantation is compromised by the onset of chronic lung allograft dysfunction, which affects about 50% of patients after 5-year transplantation. More than 70% of patients show a characteristic obliteration of the small airways (OB) characterized by intraluminal fibroproliferation and neutrophilic airway inflammation. The current therapeutic approaches are ineffective probably due to the inability of the drug to effectively reach the site of constriction without excessively increasing systemic toxicity (2.1.1).

Searching for new therapeutic strategy, in a previous work,[30] we engineered gold NPs loaded with a proliferation inhibitory drug (everolimus) specifically targeted to the MCs responsible for the fibroproliferative process.[30] The pathogenesis of BOS is a multifactorial disease, which includes a primary damage to the epithelia, caused by several inflammatory insults such as ischemia-reperfusion, rejection, and infection. In this perspective, outer factors stimulating the inflammatory response could increase the reactive local milieu with production of chemo- and cytokines by epithelial cells, smooth muscle cells, lymphocytes, macrophages and neutrophils, favoring MCs overproliferation and thus creating a vicious cycle with inflammatory and immune response. For these reasons it is mandatory that the treatment with NPs must not enhance the inflammatory response activation.

In this work, we first assayed the effect of our NPs on isolated inflammatory cells, lymphocytes, macrophages and neutrophils *in vitro*. The experiments were performed under both basal and stimulated conditions of cells, in order to simulate a clinical situation in which the drug administration could occur either in already immunoreactive environment or not.

2.3.1 Internalization of GNPs by inflammatory cells

We first determined the capability of macrophages, lymphocytes and neutrophils to internalize our nanoconstruct. For this purpose, we incubated the three cell types with GNPs functionalized (GNP-HC) or not (GNP-PEG) with antibody against CD44, in order to evaluate if the presence of anti-CD44 could enable the internalization of NPs by inflammatory cells.

By flow cytometry, we observed that the presence of the anti-CD44 antibody was required for internalization only in the case of lymphocytes (Figure 3C), in keeping with previous data showing the role of CD44 on T cells in regulating tethering and rolling interactions with vascular endothelial cells.[33,34] Macrophages and neutrophils were able to incorporate GNP-PEG and GNP-HC at the same extent (Figure 2.3A and B) because of the phagocytic ability of these innate immune cells.[35] Our results regarding the capability of macrophages to internalize GNPs were confirmed by Geiser and colleagues in *in vivo* experiments by treating mice with inhalative gold NPs.[36]

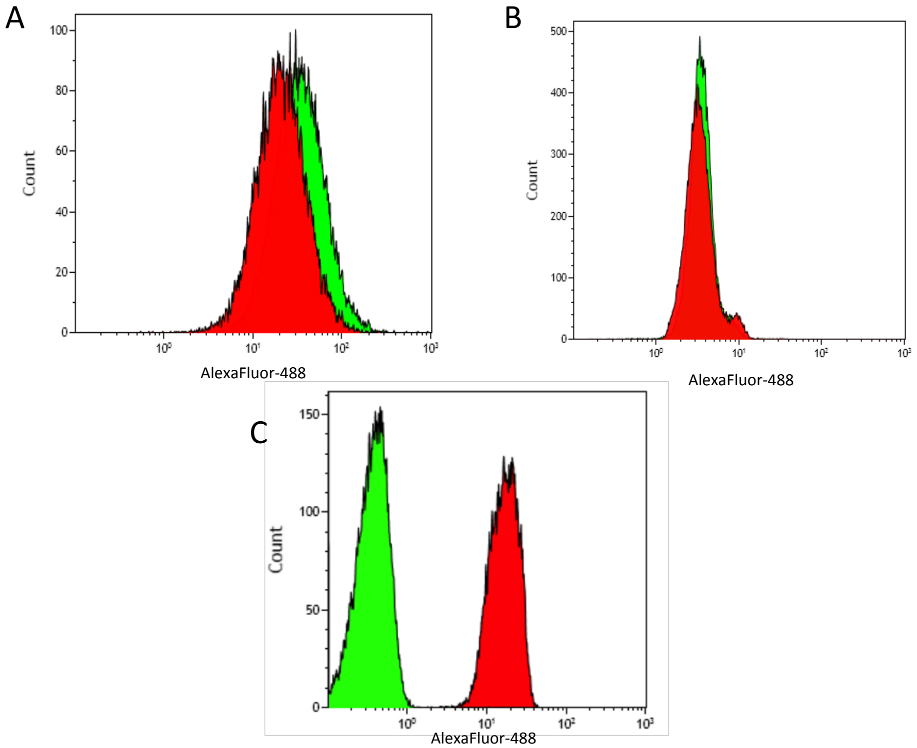

Figure 2.3. Uptake of GNP-PEG (green) and GNP-HC (red) by inflammatory cells. Alexa Fluor 488-marked NPs with (GNP-HC) or without (GNP-PEG) anti-CD44 antibody were incubated for 2 h at 37 °C in complete medium with macrophages (A), neutrophils (B) and lymphocytes (C). Internalization was detected by flow cytometry by analyzing the fluorescence of single event.

2.3.2 Response of macrophages to GNPs treatment

Experiments performed with NPs labeled with Alexa Fluor-488 fluorochrome showed that macrophages incorporated NPs both functionalized and non-functionalized with anti-CD44 (Figure 2.3A). Next, we evaluated cell viability by MTT test, to assess whether GNPs modified with anti-CD44 and loaded with everolimus (GNP-HCe) could alter macrophage metabolic activity under basal and LPS-stimulated conditions, being LPS a potent activator of macrophages. As controls, we used GNP-HC and everolimus (EV) alone (Figure 2.4).

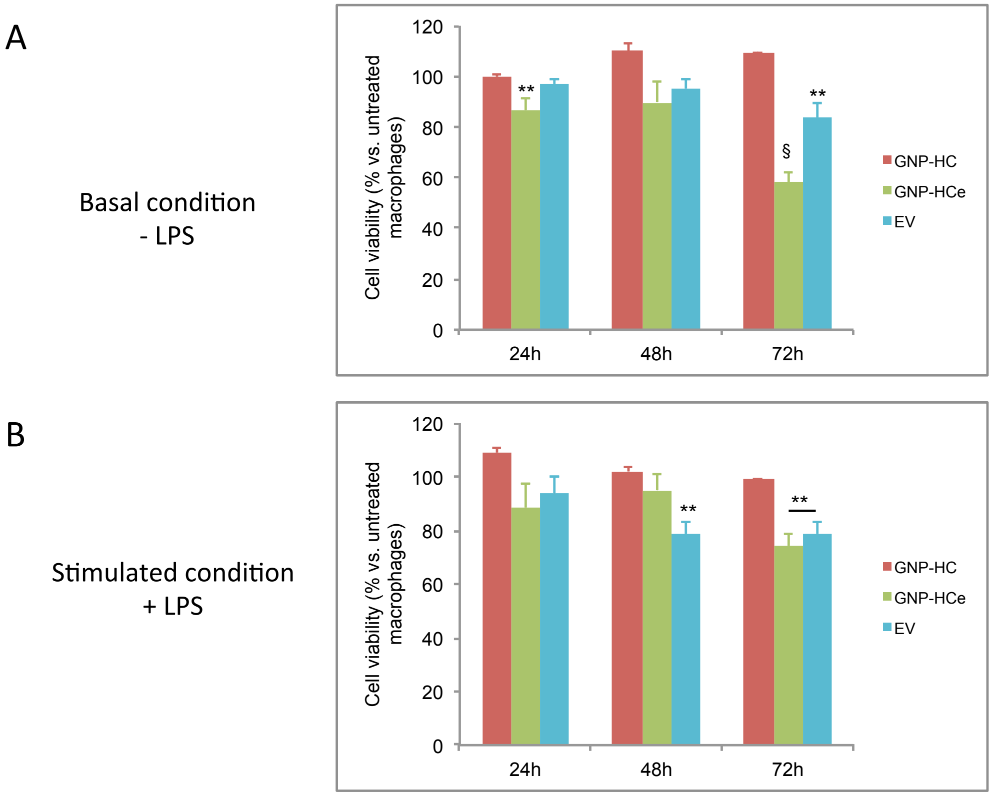

Figure 2.4. Effect of GNP-HCe on macrophages viability. The viability rate was evaluated by MTT test, at 24, 48 and 72 h after 2 h incubation with GNP-HCe, GNP-HC and EV in unstimulated (A) and stimulated condition (B) with 0.01 mg/ml LPS. GNP-HCe and GNP-HC do not stimulate macrophages in basal condition bringing a inhibit effect on their metabolic activity at 24 h and 72 h after incubation (A, B). Untreated represents the 100%. Histograms are obtained from the means ± standard error of three experiments. The error bars represent the standard error. **, $P<0.05$ vs. untreated; §, $P<0.01$ vs. untreated, EV, GNP-HC.

Under unstimulated conditions (no LPS, Figure 2.4A), we observed that GNP-HCe significantly decreased the metabolic activity of macrophages after 72 h of treatment compared to EV and GNP-HC, suggesting that the encapsulation of EV inside GNPs enhanced the anti-inflammatory activity against bronchoalveolar macrophages already present in the lungs but not yet stimulated. In contrast, under LPS-stimulated conditions (Figure 2.4B) we noticed that GNP-HCe slightly decreased the viability of stimulated macrophages, but with no significantly difference from EV alone.

As high IL-8 levels, the major cytokine secreted by stimulated macrophages, are found in BAL of patients suffering from BOS;[37] it is very important to define the impact of GNP-HCe on IL-8 release by macrophages treated or not with LPS. This should provide a clearer understanding of the effect of our nanovehicles on the release of this cytokine from macrophages in view of a possible treatment of BOS patients. For instance, a reduced IL-8 release might mitigate inflammation as well. We measured IL-8 in the media after 24 and 48 h of incubation with GNP-HCe, using as controls EV alone and GNP-HC (Figure 2.5).

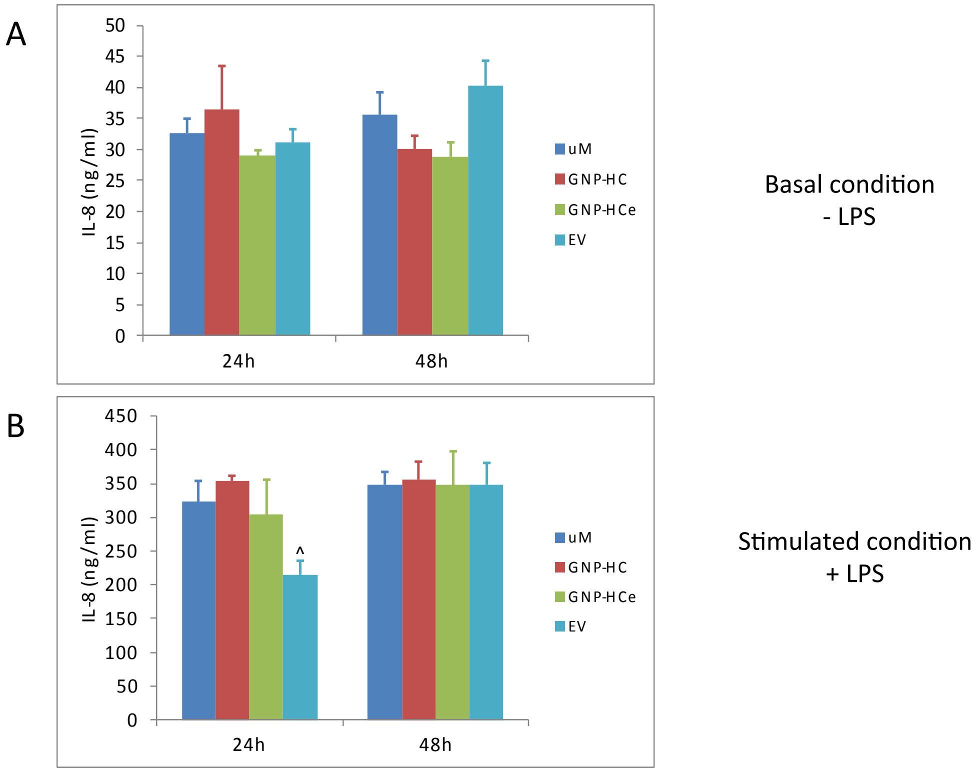

Figure 2.5. IL-8 macrophages production. Treatment with GNPs did not improve IL-8 secretion in basal condition (A) and stimulated macrophages (B). Histograms are obtained from the means ± standard error of three experiments. The error bars represent the standard error. ^, $P<0.05$ vs. untreated macrophages (uM).

The treatment with both NPs used in this study did not alter IL-8 secretion in both conditions of experiments (Figure 2.5A and B). Treating stimulated macrophages with EV alone led to a significant decrease in IL-8 release after 24 h, which is not surprising given the documented immunosuppressive effect of everolimus.[38,39,40]

The impairment of cell viability by GNP-HCe was confirmed by measurements of the mitochondrial membrane potential (Δψm). Figure 2.6 shows that GNP-HCe induced mitochondrial membrane depolarization, as shown by the significant decrease in red/green fluorescence intensity ratio of JC-1. In unstimulated macrophages, the decrease in Δψm by GNP-HCe was much more evident compared to other treatments, whereas in stimulated macrophages the different treatments resulted in comparable effects. When assessing GNP-HC toxicity by MTT and JC-1 assays we did not obtained comparable results. We hypothesize that JC-1 maybe is a much more sensitive assay than MTT, but further investigation are underway to better understand this discrepancy.

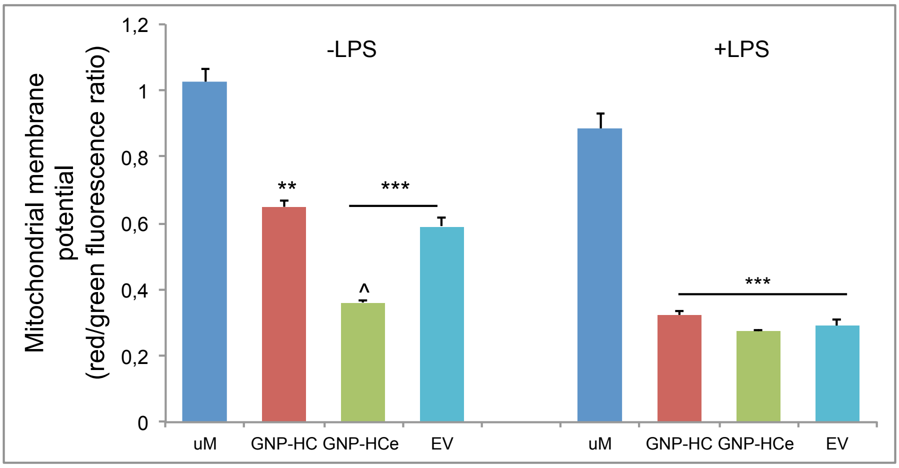

Figure 2.6. Effect of GNPs and EV on mitochondrial membrane potential. After 48 h of treatment with GNP-HCe, GNP-HC and EV, we stained un-stimulated and stimulated macrophages with JC-1 dye. Histograms represent the red/green fluorescent ratio obtained from the means ± standard error of three experiments. **, $P<0.05$ vs. untreated macrophages (υM); ***, $P<0.01$ vs. untreated (υM); ^, $P<0.01$ vs. GNP-HC, EV.

Next, using EPR spectroscopy in collaboration with Mrakic-Sposta (Institute of Bioimaging and Molecular Physiology of CNR), we evaluated if the presence of GNP-HCe, GNP-HC and everolimus alone could alter the intracellular and extracellular levels of ROS in macrophages (Figure 2.7).

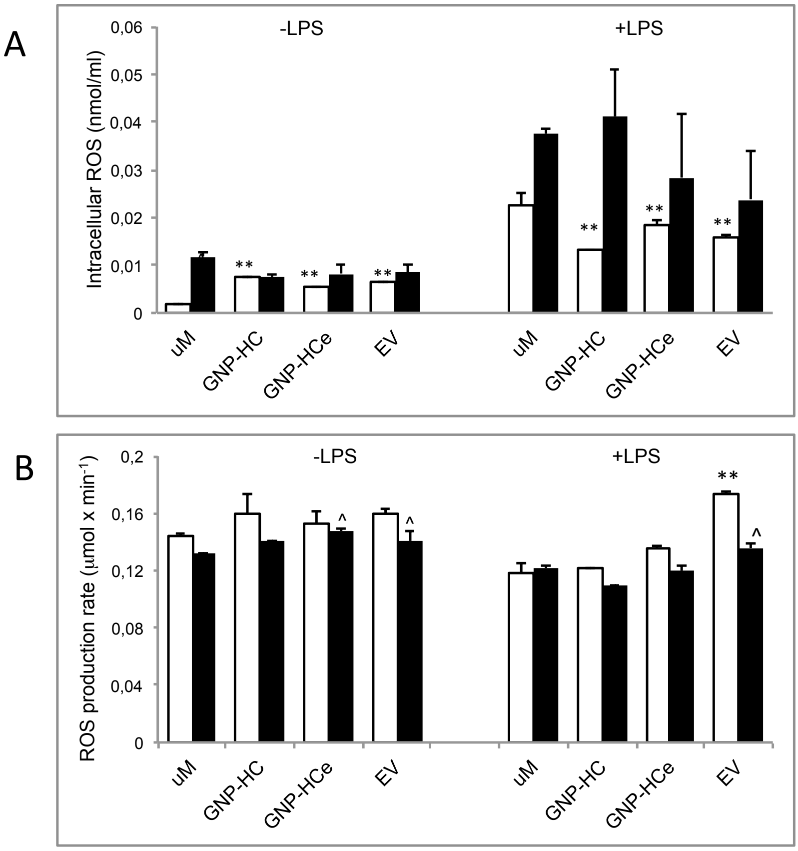

Figure 2.7. Analysis of ROS levels. Intracellular (A) and extracellular (B) ROS levels were calculated by EPR acquisition after 24 (white) and 48 (black) h of treatment with GNPs and EV. Histograms were obtained from the means ± standard error of three experiments **, P<0.01 vs. untreated (uM); ^, P<0.05 vs. untreated macrophages (uM).

When we analyzed the intracellular levels under basal conditions (–LPS), we noticed that GNP-HCe caused a slight increase in ROS compared to untreated cells after 24 h of treatment, which was reflected in extracellular environment after 48 h (Figure 2.7B, –LPS). Under stimulated conditions (+LPS), GNP-HCe slightly decreased the intracellular levels of ROS after 24 h, with no alteration in extracellular ROS (Figure 2.7A, +LPS). It is worth noting that under both conditions GNP-HCe did not elicit additional oxidative stress inducing extracellular secretion of ROS. This is an important aspect because the stimulation of ROS by macrophages enhances the recruitment of lymphocytes at the site of injury, prolonging a profibrotic inflammatory response.[41]

In the case of EV, under LPS$^+$-conditions even if we observed a decrease in intracellular ROS, we noticed an increase in the extracellular environment after 24 and 48 h. These results suggest that EV might enhance the secretion of ROS produced by LPS-stimulation in extracellular environment maybe leading to oxidative stress.

The discrepancy between effect GNP-HCe and EV alone could be possible assigned to the presence of anti-CD44 antibody on GNP surface; in fact, GNP-HC had the same effect of GNP-HCe on ROS levels suggesting that antibody against CD44 could be an important element in ROS secretion pathway by macrophages. In literature, there are no data about the role of CD44 in macrophages ROS production and secretion, but is known that CD44 could be involved in ROS defense pathway.[42,43]

2.3.2 Neutrophil response to GNPs treatment

Flow cytometry experiments showed that, like in the case of macrophages, PMNs were able to uptake both functionalized and non-functionalized NPs (Figure 2.3B), given their phagocytic nature due to the key microbicidal function of neutrophils.[44] These innate immune cells have a very short half-life (6-8 h), which is even shorter if they are stimulated.[45] For this reason we could only analyze the effects of GNP-HCe under the basal condition of PMNs isolated from peripheral blood, using as a positive control neutrophils stimulated with N-formyl-Met-Leu-

Phe (fMLP), a naturally occurring bacterial peptide that stimulates PMNs through a specific membrane receptor.[46]

First, we assessed the effect of GNP-HCe, GNP-HC and everolimus alone on the secretion of elastase, a potent serine proteinase released during phagocytosis and cell death.[47]

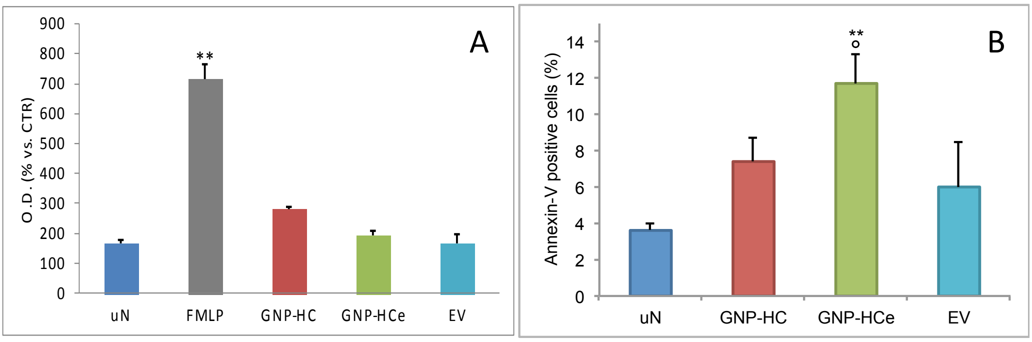

Figure 2.8. Effect of GNPs and EV neutrophil (A) elastase secretion and (B) apoptosis. (A) Elastase secretion was not modified by any treatment (GNP-HCe, GNP-HC and EV) unlike the positive control FMLP. (B) A slightly significant increase in apoptotic rate is induced by GNP-HCe compared to other conditions. **, $P<0.001$ vs. other conditions; °, $P<0.01$ GNP-HCe vs. EV.

Figure 2.8A shows that our nanoconstruct did not induce elastase secretion from neutrophils, which was instead elicited by fMLP, as expected.

Next, we evaluated the propensity of GNP-HCe to induce apoptosis in neutrophils by incubating cells with NPs for 4 h. Cells were stained with fluorocrome-labeled Annexin-V, which was specifically designed for the identification of apoptotic cells because this molecule can bind phosphatidylserine during apoptosis, translocating to the external side of the cell membrane. We found that a slight increase in apoptotic rate was induced by GNP-HCe compared to other conditions (Figure 2.8B) even if the relevant percentage was rather low (11.7 ± 1.6 %).

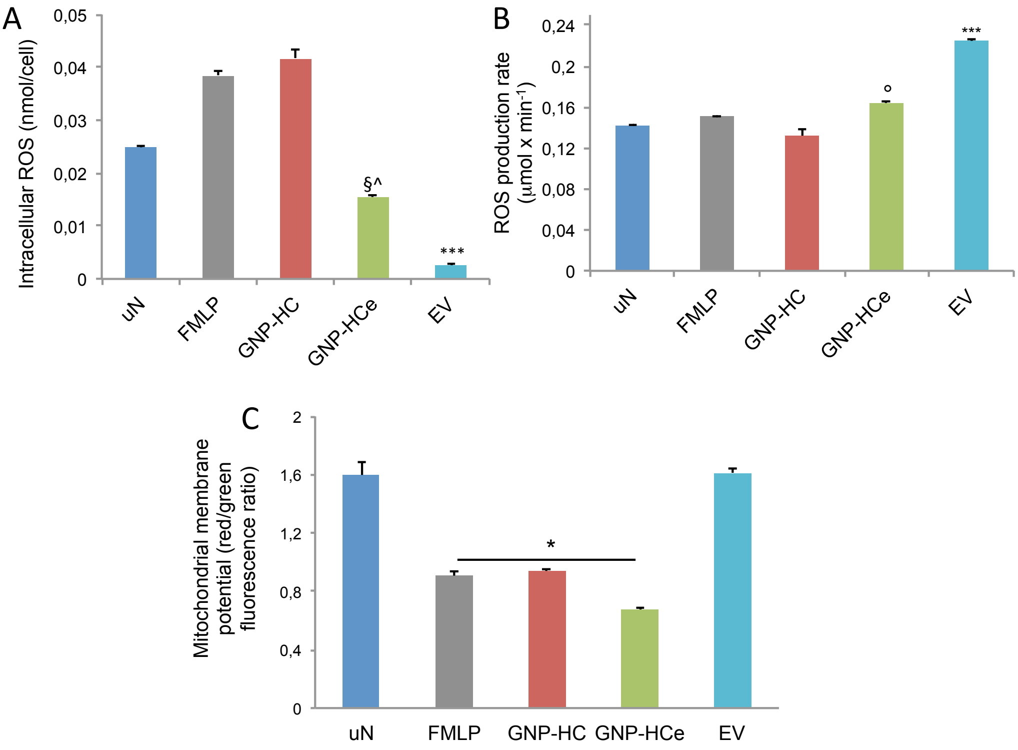

Figure 2.9. Effects of treatments on mitochondrial activity. Only in presence of everolimus both free and nanoformulated we observed an alteration in intracellular (A) and extracellular (B) ROS levels. The measurement of Δψm shown that GNPs treatment depolarized the potential of membrane instead of EV alone (C). §, P<0.05 vs. untreated (uN); ^, P<0.001 vs. GNP-HC, EV, fMLP; ***, P<0.001 vs. uN, fMLP, GNP-HC, GNP-HCe; °, P<0.01 vs. uN, GNP-HC, fMLP; *, P<0.001 vs. uN, EV

Regarding the analysis of mitochondrial function and oxidative stress state after incubation with GNPs and EV alone for 4 h, we observed that GNP-HCe and everolimus significantly increased ROS secretion in culture media, although a dramatic drop in intracellular free radicals was recorded, suggesting a leakage of ROS from the cells rather than a burst of secretion (figure 2.9A and B). As already observed for macrophages, membrane potential was significantly affected both by GNP-HC and GNP-HCe while no changes were induced on incubation with EV (figure 2.9C).

2.3.3 Response of lymphocytes to GNPs treatment

In preliminary experiments, we found that lymphocytes display CD44 expression, as already reported in the literature (2.3.1);[33,34] in fact, we observed that only GNP functionalized with anti-CD44 were internalized by lymphocytes (Figure 2.3C). Like in the case of macrophages, the following experiments were performed under both basal and stimulated conditions of cells by inducing them with Phytohaemagglutinin (PHA), a plant mitogen whose mechanism of induction mimic antigen stimulation of immunocompetent cells.[48]

The differentiation of lymphocytes is regulated by proliferation and migration but also by cell death: in particular, activation-induced cell death (AICD) in T-cells plays a pivotal role in maintaining self-tolerance after transplantation.[49,50] For this reason, we decided to analyze the impact of GNP-HCe on the apoptosis rate of activated lymphocytes, as well as on T-cells under basal conditions, to evaluate if our nanocostruct could ameliorate the self-tolerance against lung graft in BOS patients, thus inducing apoptosis.

Figure 2.10B shows that treatment of PHA-induced lymphocytes with GNP-HCe resulted in significant increase in apoptotic rate after 8 h, also persisting after 24 h, as compared to EV alone, the effect of which vanished with time. These results indicate a persisting action of the drug as a result of encapsulation inside NPs.

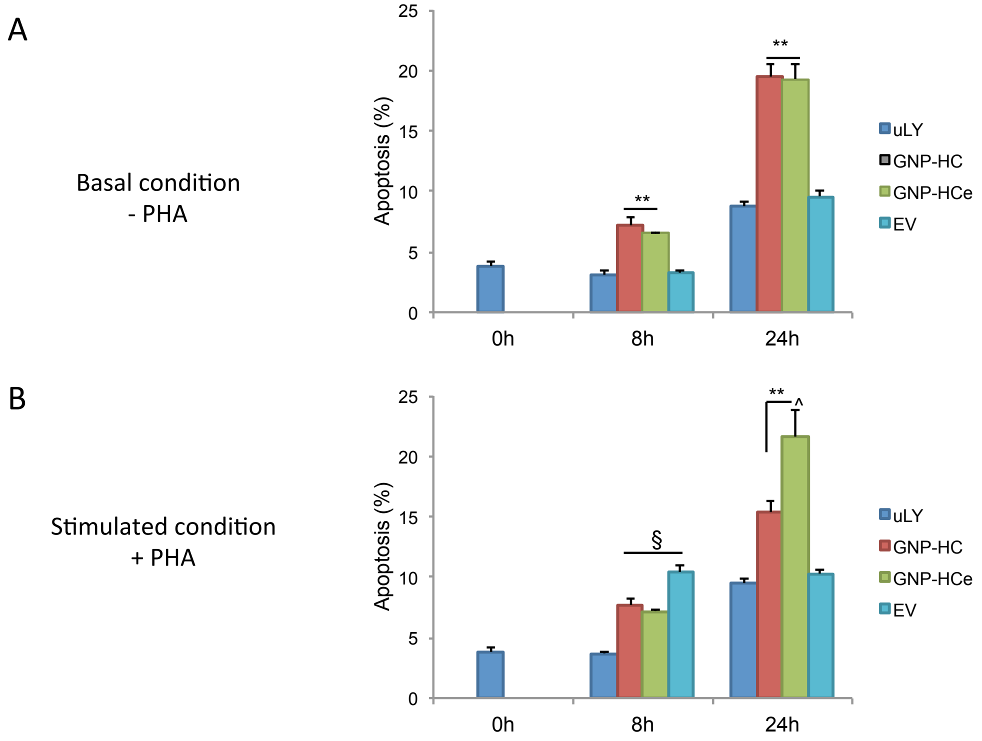

Figura 2.10. Effect of GNP-HCe on lymphocytes' apoptosis. Apoptosis, as assessed by Annexin-V incorporation at 8 and 24 h after incubation with GNP-HCe, GNP-HC and EV, was shown to persist after 24h in GNP-HCe- compared to everolimus-treated cells under basal (A) or stimulated conditions (B). Histograms are obtained from the means ± standard error of three experiments. The error bars represent the standard error. **, P<0.01 vs. untreated lymphocytes (uLY) and EV; §, P<0.01 vs. uLY; ^, P<0.01 vs. GNP-HC.

Noteworthy is that GNP-HC and GNP-HCe exerted a comparable effect especially under basal conditions (Figure 2.10A). These data suggest that the presence of anti-CD44 antibody could play an important role in inducing an apoptotic signaling pathway in lymphocytes after binding its specific receptor. Plenty of literature reports on the role of CD44 in the regulation of AICD in T-cells, but there is not general agreement on its effect, probably due to the use of different T cell subpopulation and antibody-mediated ligation of CD44.[51] At the moment, we can only speculate that in our experiments the functionalization of GNP with anti-CD44 antibody together with everolimus might induces the AICD signal in lymphocytes (either induced or not) leading to an enhancement of self-tolerance. The enhancement of the effect of everolimus formulated *via* NPs compared to the drug alone was particularly evident in the analysis of cytokine production (Figure 2.11).

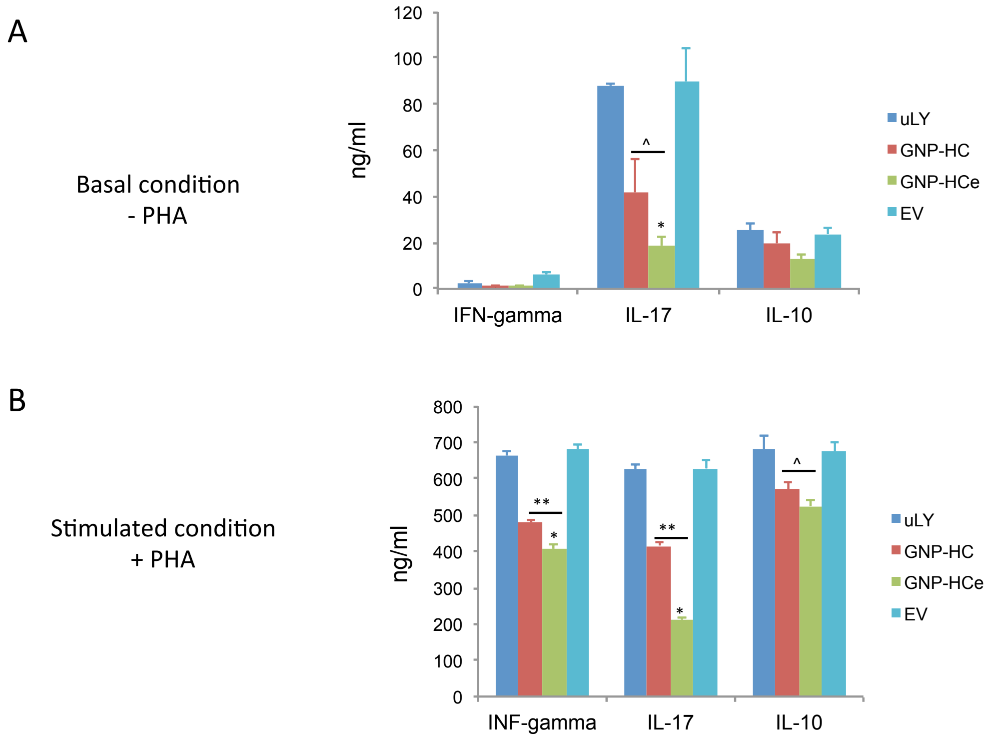

Figure 2.11. Interleukins secretion analysis after treatment with NPs. Cells were exposed with GNPs and EV alone for 48 h. The secretion of IFNγ, IL-17 and IL-10 in supernates were measured by the ELISA technique. The results are represented as the mean of three independent experiments ± standard errors. ^, $P<0.05$ vs. untreated lymphocytes (uLY), EV; *, $P<0.01$ vs. GNP-HC; **, $P<0.001$ vs. uLY, EV.

For the purpose of this work, it should be stressed that the effect of GNP-HCe was particularly evident in PHA-stimulated lymphocytes (Figure 2.11B), where our nanovehicle decreased significantly the secretion of INF-γ, IL-17 and IL-10 compared to EV alone, which in contrast had no effect. These results are particularly relevant in a perspective of future therapies based on GNP-HCe, because IFN-γ and IL-17 are two major elements in BOS disease. In particular, IFN-γ, mostly produced by activated T cells, is a major player in allograft rejection in that induces major histocompatibility complex (MHC) expression in epithelial and endothelial cells against foreign antigens.[52,53] Furthermore, IL-17 is a potent inducer of IL-8 release by lung endothelial and epithelial cells, creating a chemotactic gradient towards airways lumen for innate immune cells (2.1.1).

Mammalian TOR (mTOR) exerts many different activities, among which the capability to modulate the immune response, altering the regulation of T cell trafficking by induction of expressions of certain cell surface receptors like CD8 and CD4.[54] Therefore, we assayed the effect of GNP-HCe on $CD4^+$ and $CD8^+$ expression in $CD3^+$ lymphocytes population in order to evaluate whether and how everolimus encapsulated in NPs could modify the ratio between the two surface receptors, as compared to the effect of the free drug.

We found that GNP-HCe slightly reduced $CD3^+CD4^+$ population under both experimental conditions (+/- PHA) similarly to everolimus alone (figure 2.12A and B). In the case of $CD3^+CD8^+$ population, the effect of everolimus was evident only if the drug was encapsulated inside the NPs (Figure 12B). Moreover, also in this case the role of the anti-CD44 antibody was apparent, as GNP-HC showed the same behavior of GNP-HCe.

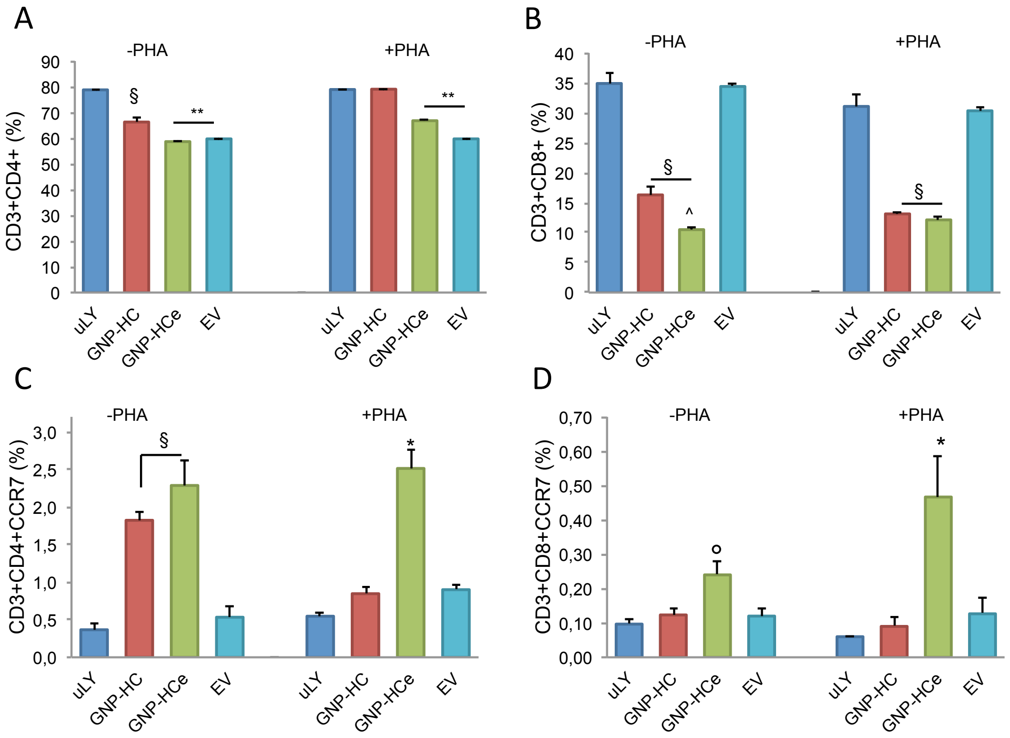

Figure 2.12. Enumeration of two specific lymphocytes populations and analysis CCR7 expression. Treatment with GNP-HCe reduced the percentage of both cell populations (A, B), which was more evident in the case of CD3$^+$CD8$^+$ population (B). The analysis of CCR7 expression revealed that GNP-HCe was capable of increasing its expression on both populations (C, D). Histograms were obtained by mean of three different set of experiments ± standard errors. **, $P<0.001$ vs. untreated lymphocytes (uLY), GNP-HC; §, $P<0.001$ vs. uLY; ^, $P<0.05$ vs. GNP-HC; *, $P<0.001$ vs. all other conditions; °, $P<0.05$ vs. all other conditions.

In addition, it is known that inhibitors of mTOR increase the expression of CCR7, a chemokine receptor necessary for T-cells exit from peripheral tissues.[54,55] After treatment with GNP-HCe and EV alone, we noticed that the expression of the CCR7 surface marker was increased only by treatment with NP-encapsulated EV, probably as a result of higher internalization (Figure 2.12C and B). These results also suggest that GNP-HCe could improve the propensity of these cells to home to secondary lymphoid tissues, thus promoting allograft survival.

2.3.4 Localization of inhaled GNP-HC in normal mice

One of the main purposes when we designed the nanovehicle-based treatment to specifically target MCs was to administer them by the inhalatory route. Therefore, we undertook *in vivo* experiments treating normal mice with a) GNP-HC without everolimus to understand the fate of NPs and b) GNP-HCe in order to evaluate if our "fully armed" NPs could induce an inflammatory insult. Mice were aerosolized with either GNPs 30 min/day, for 2 weeks, 5 days per week.

The experiments demonstrate that mice lungs were strongly positive to fluorescence-labeled GNP-HC when inhaled, compared to untreated mice (Figure 2.13A and B) and there were no accumulation of NPs in spleen, kidney or liver (Figure 13C). This is in contrast with the observation by Sung et al.[56] and Yu et al.[57], in which an accumulation at the liver was described. However, there are several differences in the treatment conditions (for instance, different inhalation exposure) and NP characteristics (for instance, surface coating) that could explain this discrepancy.

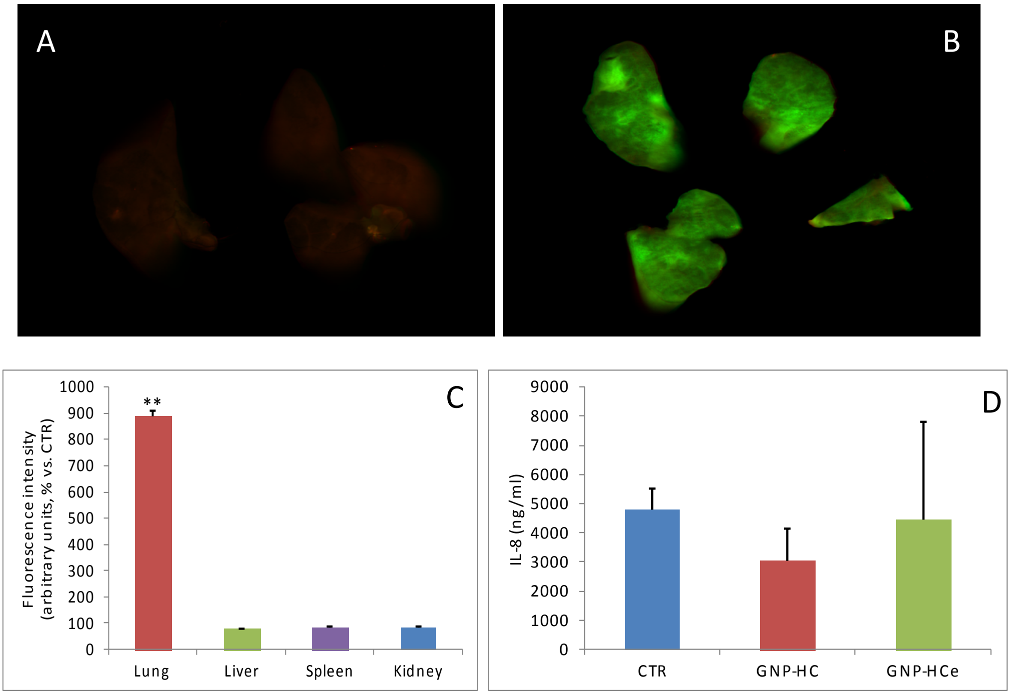

Figure 2.13. Evaluation of IR-820 dye-NH2 marked GNP-HC signal by near infrared light microscopy technology (A-C), IL-8 measurements in mice's BAL by ELISA test (D). No fluorescent signal is evident in untreated mice lungs (A); mice lungs show a strong positive fluorescence after GNP-HC treatment (B); no signal differences are recorded in liver, kidney and spleen (C); no significant induction of IL-8 secretion by macrophages after treatment with GNP-HCe and GNP-HC (D). **, $P<0.001$ GNP-HCe treated *vs.* untreated lungs (CTR).

We also evaluated the bronchoalveolar lavage of treated mice that, interestingly, did not show any significant increase in IL-8 pro-inflammatory cytokine, suggesting that GNP-HCe did not elicit an inflammatory response (Figure 2.13D).

In another work, a single intratracheal instillation of 50 and 250 nm GNP generated only a mild inflammatory response, being mostly taken up by alveolar macrophages.[58] In our experiments, TEM images showed that anti-CD44-functionalized NPs were inside the macrophages (Figure 2.14D) confirming that macrophage clearance represents the most prominent defense line of the respiratory tract.[59] This result is in accordance with other works in which gold NPs with similar size locally administered by inhalation or intratracheal instillation were retained mostly in the lungs,[55,57,60] confirming our results obtained by NIR imaging technology.

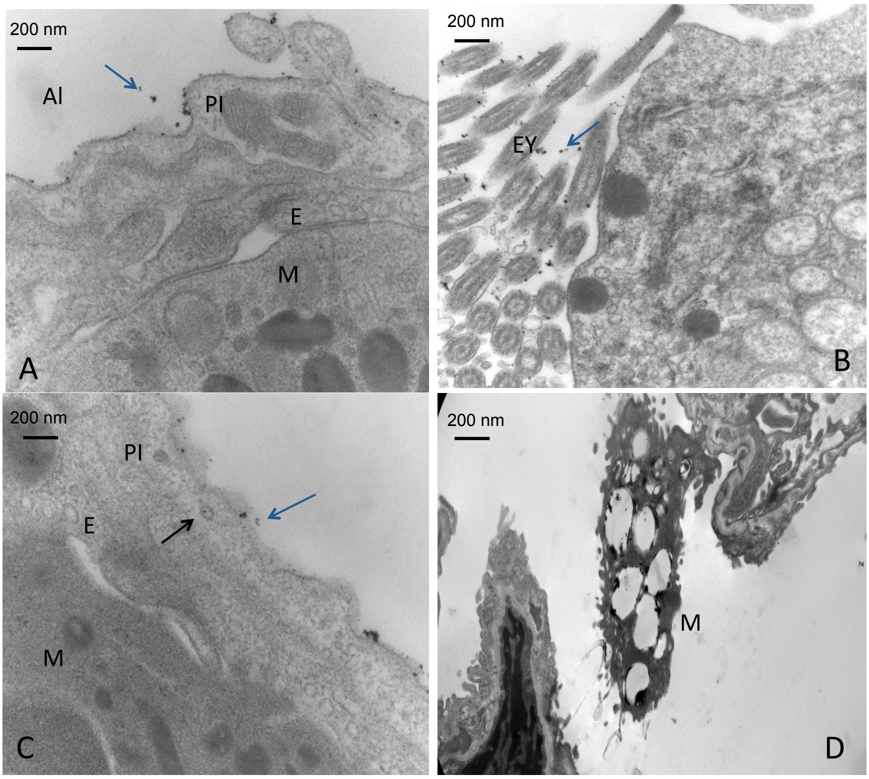

Figure 2.14. Transmission electron microscopy images. GNP-HC (indicated by blue arrows) localized in bronchoalveolar lumen and on surface of pneumocytes (A, B). GNP-HC observed in an endosome as indicated by black arrow (C). GNP-HC up-take by macrophages (D). M: macrophages; PI: pneumocytes; E: endothelium; EY: lung eyelashes; Al: alveolus.

2.3.5 Conclusions

In summary: 1) the size of our NPs (50 nm) is not associated with any detectable toxicity when they are administered by the inhalation route, since they accumulate in lungs, do not significantly cross the alveolar epithelia, nor do they elicit any inflammatory response; 2) PEG coating decreases nonspecific interactions with cell surface or biological fluid proteins, which makes them functional and efficient nanovehicles; 3) the functionalization of our nanoconstruct with anti-CD44 antibody directed toward MCs is an important component also in view of targeting adaptive and innate immune cells, as the CD44 receptor is expressed both in lymphocytes and in macrophages and neutrophils. Given the phagocytic features of the latter types of cells, the functionalization of GNPs is obviously not essential for the uptake by these innate immune cells, although active targeting is expected to favor localized accumulation.

Although these data suggest a predominant localization at lung macrophages, the final destiny of these macrophages and the clearance of GNP are still in debated. Of course, further *in vivo* experiments under chronic administration regimen are necessary. These experiments should be performed on a lung allograft transplanted animal model since the NPs have been specifically engineered to target a cell population that overproliferates in a pathological context.

In conclusion, we can state that our gold NPs do not further boost the inflammatory response, whereas they do enhance the immunosuppressive effect of EV. The presence of an anti-CD44 antibody seems to be crucial for ROS secretion by macrophages and neutrophils and for the decline of $CD3^{+}CD8^{+}$ lymphocytes population. These remarks highlight the role of the molecules conjugated on GNP surface. In any case, an advantage of our local administration by the inhalatory route is that it is likely to decrease the potential side effects that normally could occur when administering NPs through other more conventional treatments.

2.4 References

---

[1] Belperio JA. et al. Chronic lung allograft rejection. Mechanisms and Therapy. *Proc Am Thorac Soc.* 2009; 6: 108-121.

[2] Al-Githmi I. et al. Bronchiolitis obliterans following lung transplantation. *Eur. J. Cardiothorac. Surg*. 2006; 30: 846—851

[3] Knoop C. and Estenne M. Acute and chronic rejection after lung transplantation. *Semin Respir Crit Care Med.* 2006; 27: 521–533.

[4] Van den Berg JW. et al. Bronchiolitis obliterans syndrome and additional costs of lung transplantation. *Chest.* 2000; 118: 1648–1652.

[5] Todd JL. et al. Bronchiolitis Obliterans Syndrome: The Final Frontier for Lung Transplantation. *Chest.* 2011; 140: 502-508.

[6] Elssner A. et al. The role of neutrophils in the pathogenesis of obliterative bronchiolitis after lung transplantation. *Transpl. Infect. Dis*. 2001; 3: 168-176.

[7] Zheng L. et al. The dynamics and associations of airway neutrophilia post lung transplantation. *Am. J. Transplant.* 2006; 6: 599–608.

[8] Palmer SM. et al. Innate immunity influences long-term outcomes after human lung transplant. *Am. J. Respir. Crit. Care Med.* 2005; 171: 780–785.

[9] Vanaudenaerde BM. et al. Innate and adaptive interleukin-17-producing lymphocytes in chronic inflammatory lung disorders. *Am J Respir Crit Care Med Vol.* 2011; 183: 977–986.

[10] Crestani B. Bronchoalveolar Lavage Brings Mesenchymal Stem Cells to the Light. *Am. J. Respir. Crit. Care Med*. 2012; 185: 7-8.

[11] Lama VN. et al. Evidence for tissue-resident mesenchymal stem cells in human adult lung from studies of transplanted allografts. *J. Clin. Invest*. 2007; 117: 989-996.

---

[12] Sato M. and Keshavjee S. Bronchiolitis obliterans syndrome: alloimmune-dependent and -independent injury with aberrant tissue remodeling. *Semin. Thorac. Cardiovasc. Surg.* 2008; 20: 173–182

[13] Ramirez AM. et al. Activation of tissue remodeling precedes obliterative bronchiolitis in lung transplant recipients. *Biomark. Insights*. 2008; 3: 351–359.

[14] Hayes D. et al. A review of bronchiolitis obliterans syndrome and therapeutic strategies. *J. Cardiothor. Surg*. 2011; 6: 92.

[15] Corris PA. et al. A randomised controlled trial of azithromycin therapy in bronchiolitis obliterans syndrome (BOS) post lung transplantation. *Thorax.* 2015; 70: 442–450.

[16] Bianco R. et al. Inhibition of mTOR pathway by everolimus cooperates with EGFR inhibitors in human tumours sensitive and resistant to anti-EGFR drugs. *Br. J. Cancer*. 2008; 98: 923–930.

[17] Azzola A. et al. Everolimus and mycophenolate mofetil are potent inhibitors of fibroblast proliferation after lung transplantation. *Transplantation.* 2004; 77: 275–280.

[18] Nashan B. Review of the proliferation inhibitor everolimus. *Expert. Opin. Invest. Drugs*. 2002; 11: 1845–1857.

[19] Lu Y. and Chen W. Sub-nanometre sized metal clusters: from synthetic challenges to the unique property discoveries. *Chem. Soc. Rev.* 2012; 41: 3594–3623.

[20] Giljohann DA. et al. Gold nanoparticles for biology and medicine. *Angew. Chem. Int. Ed.* 2010; 49: 3280–3294.

[21] Saha K. et al. Gold nanoparticles in chemical and biological sensing. *Chem. Rev.* 2012; 112: 2739–2779.

[22] Sperling RA. et al. Biological applications of gold nanoparticles. *Chem. Soc. Rev.* 2008*;* 37: 1896–1908.

[23] Kim C. et al. Recognition-mediated activation of therapeutic gold nanoparticles inside living cells. *Nat. Chem*. 2010; 2: 962–966.

---

[24] Kuriyama S. et al. Particle-mediated gene transfer into murine livers using a newly developed gene gun. *Gene Ther*. 2000; 7: 1132–1136.

[25] Brust M. et al. Synthesis of Thiol derivatised Gold Nanoparticles in a Two-phase Liquid-Liquid System. *J Chem Soc Chem Commun*. 1994; 7: 801–802.

[26] Seol SK. et al. One-Step Synthesis of PEG-Coated Gold Nanoparticles by Rapid Microwave Heating. *J. Nanomat.* 2013; 2013.

[27] Pellegrino T. et al. Hydrophobic nanocrystals coated with an amphiphilic polymer shell: A general route to water soluble nanocrystals. *Nano Lett*. 2004; 4: 703–707.

[28] Alkilany AM. Et al. Toxicity and cellular uptake of gold nanoparticles: what we have learned so far? *J Nanopart Res.* 2010; 12(7): 2313–2333

[29] Dykman L. and Khlebtsov N. Gold nanoparticles in biomedical applications: recent advances and perspectives. *Chem. Soc. Rev*. 2012; 41: 2256-2282.

[30] Cova E. et al. Antibody-engineered nanoparticles selectively inhibit mesenchymal cells isolated from patients with chronic lung allograft dysfunction. *Nanomedicine*. 2014.

[31] Kovarik JM. Everolimus in pulmonary transplantation: pharmacokinetics and exposure-response relationships. J. Heart Lung Transplant. 2006; 25: 440 – 446.

[32] Mrakic-Sposta S. et al. Assessment of a standardized ROS production profile in humans by Electron Paramagnetic Resonance. Oxid Med Cell Longev. 2012; 2012:973927.

[33] Baaten BJ et al. Multifaceted regulation of T cells by CD44. *Commun Integr Biol*. 2010; 3: 508–512.

[34] Guan H. et al. CD44 Reciprocally regulates the differentiation of encephalitogenic Th1/Th17 and Th2/regulatory T cells through epigenetic modulation involving DNA methylation of cytokine gene promoters thereby controlling the development of experimental autoimmune encephalomyelitis. *J Immunol*. 2011; 186: 6955–6964.

---

[35] Henneke P. and Golenbock DT. Phagocytosis, Innate Immunity, and Host–Pathogen Specificity. *J. Exp.Med*. 2004; 5: 1-4.

[36] Geiser M. et al. Cellular uptake and localization of inhaled gold nanoparticles in lungs of mice with chronic obstructive pulmonary disease. *Part. Fibre Toxicol*. 2013, 10: 19.

[37] Elssner A. et al. Elevated levels of interleukin-8 and transforming growth factor-beta in bronchoalveolar lavage fluid from patients with bronchiolitis obliterans syndrome: proinflammatory role of bronchial epithelial cells. Munich Lung Transplant Group. *Transplantation*. 2000; 70(2): 362-367.

[38] Vitiello D. et al. Effect of everolimus on the immunomodulation of the human neutrophil inflammatory response and activation. *Cell Mol Immunol*. 2015; 12: 40-52.

[39] Lin HY. et al. Effects of the mTOR inhibitor Rapamycin on Monocyte-Secreted Chemokines. *BMC Immunol.* 2014; 15: 37.

[40] Hsu S. et al. Effects of everolimus on macrophage-derived foam cell behavior. *Cardiovasc. Revasc. Med*. 2014; 15: 269-277.

[41] Wynn TA. Integrating mechanisms of pulmonary fibrosis. *J Exp Med*. 2011; 208: 1339-1350.

[42] Mihalache CC. et al. Inflammation-Associated Autophagy-Related Programmed Necrotic Death of Human Neutrophils Characterized by Organelle Fusion Events. *J Immunol*. 2011; 186: 6532-6542.

[43] Ishimoto T. et al. Macrophage-derived reactive oxygen species suppress miR-328 targeting CD44 in cancer cells and promote redox adaptation. *Carcinogenesis*. 2014; 35: 1003–1011.

[44] Lee WL. et al. Phagocytosis by neutrophils. *Microbes Infect.* 2003; 5: 1299-1306.

[45] Summers C. et al. Neutrophil kinetics in health and disease. *Trends Immunol*. 2010; 31(8): 318–324

---

[46] Torres M. et al. Stimulation of human neutrophils with Formyl-Methionyl-Leucyl-Phenylalanine induces tyrosine phosphorylation and activation of two distinct mitogen-activated protein-kinase. *J Immunol*. 1993; 150: 1563-1578.

[47] Sommerhoff CP. et al. Neutrophil Elastase and Cathepsin G Stimulate Secretion from Cultured Bovine Airway Gland Serous Cells. *J Clin Invest.* 1990; 85(3) :682-689.

[48] Stites DP. et al. Development of Cellular Immunity in the Human Fetus: Dichotomy of Proliferative and Cytotoxic Responses of Lymphoid cells to Phytohaemagglutinin. *Proc. Nat. Acad. Sci.* 1972; 69: 1440-1444.

[49] Nakano K. et al. Engagement of CD44 up-regulates Fas Ligand expression on T cells leading to activation-induced cell death. *Apoptosis*. 2007; 12: 45-54.

[50] Russel JH. Activation-induced death of mature T cells in the regulation of immune responses. *Curr Opin in Immunol*. 1995; 5: 382-388.

[51] Baaten BJ. et al. Multifaceted regulation of T cells by CD44. *Commun Integr Biol.* 2010; 3: 508-512.

[52] Halloran PF. et al. Interferon- Acts Directly on Rejecting Renal Allografts to Prevent Graft Necrosis. *Am J Pathol*. 2001; 158.

[53] Hidalgo LG. and Halloran PF. Role of IFN-g in Allograft Rejection. *Crit Rev Immunol*. 2002; 22.

[54] Araki K. et al. TOR in the immune system. *Curr Opin Cell Biol*. 2001; 23: 707-715.

[55] Debes GF. et al. Chemokine receptor CCR7 required for T lymphocyte exit from peripheral tissues. *Nat Immunol*. 2005; 6: 889-894.

[56] Sung JH. et al. Subchronic inhalation toxicity of gold nanoparticles. *Part Fibre Toxicol.* 2011; 8: 16.

[57] Yu LE. et al. Translocation and effects of gold nanoparticles after inhalation exposure in rats. *Nanotoxicology.* 2007; 235–242.

[58] Gosens I. et al. Impact of agglomeration state of nano- and submicron sized gold particles on pulmonary inflammation. *Part Fibre Toxicol.* 2010; 7: 37.

---

[59] Gordon SB. and Read RC. Macrophage defences against respiratory tract infections. The immunology of childhood respiratory infections. *Br Med Bull*. 2002; 61: 45-61.

[60] Sadauskas E. et al. Biodistribution of gold nanoparticles in mouse lung following intratracheal instillation. *Chem. Cent. J*. 2009; 3:16.

General conclusions

During my PhD I have studied the therapeutic potential of NPs in two different diseases characterized by uncontrolled proliferation of cells: breast cancer (Chapter 1) and bronchiolitis obliterans syndrome (BOS - Chapter 2).

Given the nano structure of these particles, there is a broad range of options in their construction and functionalization of their surface, which makes it possible to endow them with multiple and specific properties.

Drug delivery is one major field of nanotechnology applied to biomedicine because of the capability of NPs to encapsulate hundreds to thousands of drug molecules within a single carrier. However, the efficacy and safety of nanoconstructs must be preserved and validated by *in vitro* and *in vivo* studies in order to avoid side effects, in view of the development of therapeutic approaches. Based on these considerations, in the present thesis I have taken advantage of nanotechnology to address the following issues of biomedical relevance:

- In Chapter 1, I have demonstrated in *in vitro* studies, the possibility to encapsulate ASC-J9, a highly hydrophobic drug, in PLGA NPs and to deliver it to breast cancer cells (MCF-7) via this nanovector, with resulting inducedROS overproduction and apoptotic cell death, without remarkable alteration in non-cancerous cell line (3T3-L1) viability.
- In Chapter 2, I have carried on *in vitro* and preliminary *in vivo* studies, whereby I have evaluated the safety of gold NPs targeted to mesenchymal cells, primary effectors of BOS, thus demonstrating that our nanoconstruct does not alter the immune response even when administered by the inhalation route in murine animal models.

In conclusion, we were able to produce very promising nanovehicles endowed with high efficiency of drug loading, stability and delivery, and good safety for the surrounding microenvironment of therapeutic targets.

Publications

Bioconjugate Chemistry
Communication
pubs.acs.org/bc

Development of U11-Functionalized Gold Nanoparticles for Selective Targeting of Urokinase Plasminogen Activator Receptor-Positive Breast Cancer Cells

Svetlana Avvakumova,[†,∥] Elisabetta Galbiati,[†,∥] Laura Pandolfi,[†] Serena Mazzucchelli,[‡] Marco Cassani,[†] Alessandro Gori,[§] Renato Longhi,[§] and Davide Prosperi*[,†]

[†]NanoBioLab, Dipartimento di Biotecnologie e Bioscienze, Università di Milano-Bicocca, Piazza della Scienza 2, 20126 Milano, Italy
[‡]Dipartimento di Scienze Biomediche e Cliniche "Luigi Sacco", Università di Milano, Via G. B. Grassi 74, 20157 Milano, Italy
[§]CNR-ICRM, Via Mario Bianco, 9, 20131, Milan, Italy

Supporting Information

ABSTRACT: The functionalization of colloidal nanoparticles with short peptides often fails in achieving satisfactory targeting efficiency and selectivity toward receptor-specific human cells. Here, we show that an optimized passivation of gold nanoparticle surface with a mixed self-assembled monolayer, including a targeting ligand, a fluorescent dye, and an intercalating short PEG derivative, led to a very stable, nontoxic, and efficient nanoconjugate for targeting urokinase plasminogen activator receptor-positive breast cancer cells.

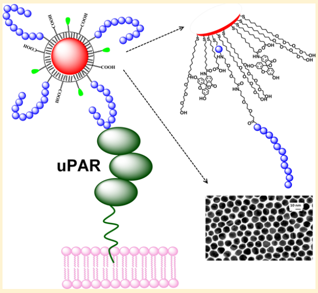

Cancer has become a major public health problem in many countries. Statistically, such cancers as pancreatic, liver, and lung lead to an extremely high level of morbidity and mortality (up to 97%), while breast cancer is most frequently diagnosed, being the leading cause of death for cancer among females.[1] Although targeted therapy with monoclonal antibodies is rapidly becoming the major nonsurgical treatment in many cancers,[2,3] the use of short peptides as targeting ligands of tumor receptors has several potential advantages over commonly employed entire antibodies. In particular, when more sophisticated nanoconjugates are used for drug delivery purposes, short peptides allow for regular and density-controlled distribution of ligands and lower immunogenicity of the nanoconstruct, along with their low nonspecific uptake by the reticuloendothelial system, such as the liver, spleen, and bone marrow. These features have led to their wide application as promising ligands for tumor targeting.[4] In addition, peptides are chemically stable and relatively easy to modify compared to monoclonal antibodies.[5]

A number of peptide-based ligands for cancer cell targeting have been described in the literature, with the most prominent examples being the arginine−glycine−aspartate (RGD) family of peptides for $\alpha_v\beta_{3/5}$ integrin receptor-targeting.[6−9] Peptide sequences derived from urokinase plasminogen activator (uPA) amino-terminal protein fragment (ATF) have recently been used as an efficient way of targeting the uPA receptor (uPAR) on cancerous cells.[10,11] uPAR was found overexpressed across a variety of tumor cells and tissues, including breast, lung, pancreas, liver, and stomach.[7] Moreover, such a high level of expression is considered to be associated with cancer invasion and metastasis.[12−16] Among uPAR-targeting peptide sequences, U11 peptide (VSNKYFSNIHW) represents a prominent part of the recognition fragment in uPA. Its loop-like structure comprises 11 amino acid residues localized at the tip of a β-hairpin loop within the growth factor domain of uPA. The interaction between U11 and uPAR was reported to be characterized by an equilibrium dissociation constant, K_d, of 1.3−1.4 μM.[10]

Thanou and co-workers used a U11 peptide−lipid amphiphile for functionalization of liposomes with the aim of nucleic acid delivery.[10] Although, the authors have obtained an efficient targeting of prostate cancer cells by the U11-functionalized nanoconjugates, still they indicated the presence of strong nonspecific interactions that caused an undesired binding of nanoparticles to the cell membranes. In addition, U11 peptide was shown to form β-sheets on the surface of liposomes when inserted at high densities. However, at low concentrations (1 mol %), the same peptide−lipid conjugates appear to rearrange into more separated structures inside the liposome bilayer.[10] Similarly, Mazzucchelli et al. have observed that direct random conjugation of U11 linear peptide to

Received: May 6, 2014
Revised: July 31, 2014
Published: July 31, 2014

dx.doi.org/10.1021/bc500202b | *Bioconjugate Chem.* 2014, 25, 1381−1386

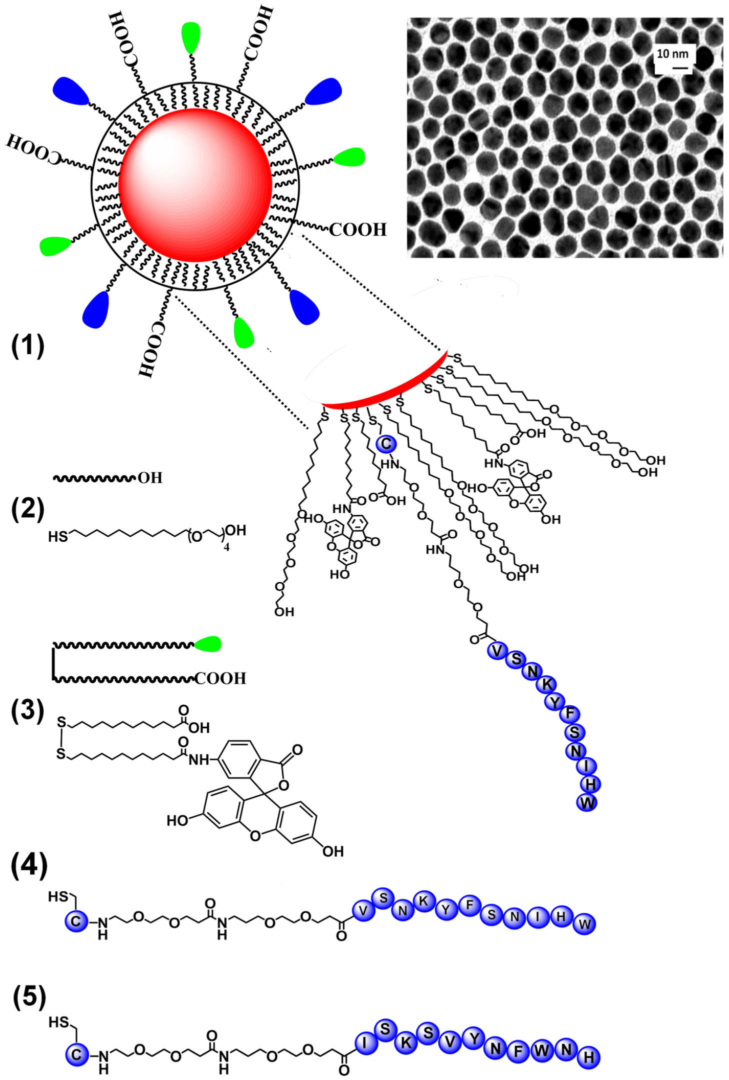

Figure 1. Schematic representation of fluorescent U11 peptide-functionalized Au-(**1**) NPs. A zoomed section of AuNP surface shows the supposed self-assembled organization of the mixed ligand monolayer. Chemical structures and amino acid sequences of the ligands and an example of TEM micrograph of AuNPs (inset) are included.

colloidal nanoparticles led to neither efficient nor selective binding of uPAR-positive cells in comparison with a uPAR-negative control, probably owing to a disadvantageous arrangement of the peptide or low availability for recognition.[17] In that case, likely the number of peptide molecules conjugated to the particle was too low to ensure successful targeting of the cells. Therefore, it is evident that the structure of the targeting molecule and its density and/or distribution on the nanoparticle surface play an important role both in colloidal stability and in the interaction with membrane receptors of the cell.[18,19]

Considering the high binding affinity of uPAR−uPA complex along with the favorable propensity of such complex to be endocytosed by receptor activation, the uPAR−U11 receptor−ligand system could be attractive for the design of smart nanoconjugates selective for uPAR targeting. Among different nanoparticles, gold nanoparticles (AuNPs) are a promising tool for biomedical applications, due to their unique optical and chemical properties, along with straightforward preparation and surface functionalization via Au−thiol chemistry.[20] In addition, the functionalization of nanoparticles with bioactive targeting ligands allows researchers to improve not only the selectivity of the conjugates exploiting a higher capacity to enter the cells but also their antitumor activity over the free drug through an increase of its local concentration.[21,22] However, no AuNPs-based anticancer drug has been approved for clinical therapy yet except for only two AuNPs-containing drugs which have been in phase 0 (pilot study) and phase 1 of clinical trials. AuroShell nanoparticles have been investigated by Nanospectra Biosciences Inc. as potential tool for near-infrared photothermal therapy of head and neak cancers.[22] On the other hand, CytImmune Sciences Inc. has developed tumor necrosis factor (TNFα) bound AuNPs, namely, CYT-6091 Aurimmune, and Taxol and TNFα-bound colloidal gold, namely, and CYT-21001 (Auritol), for the treatment of solid tumors by breaking down tumor defenses.[22]

In this paper, we show that biocompatible fluorescent AuNPs can be successfully functionalized with U11 peptide with the aim of efficient targeting of uPAR-positive cancer cells. We developed an ad hoc nanoconjugate in which U11 peptide was inserted into a mixed monolayer of ligands imparting the required stability and fluorescent properties to AuNPs. Here, U11 peptide molecules were spaced by a short-chain PEG derivative containing both −SH and −OH groups, whose polarity favors the formation of a continuous passivation layer around nanoparticles. The high surface density of PEG chains provided AuNPs with an optimal colloidal stability, allowing them to reduce protein adsorption and nonspecific interactions with nontargeted biological species.[23−26] These features conferred also a more regular distribution of the peptide on the nanoparticle surface, which presumably avoided β-sheets formation resulting in a stronger affinity of immobilized U11 for uPAR. Finally, a fluorescein-modified bis-carboxylic disulfide was used to introduce a fluorescent moiety into the ligand shell, useful for further biological experiments (Figure 1).

U11 peptide was assembled by Fmoc-based solid phase peptide synthesis (see Supporting Information) adding an extra-sequence short PEG spacer in order to separate the main peptide chain from the nanoparticle surface, while an N-terminal cysteine residue was added to allow peptide covalent conjugation to AuNPs exploiting Au−thiol chemistry (Figure 1). A scrambled U11 variant (ISKSVYNFWNH) (**5**) was used as a negative control. Citrate-stabilized AuNPs were prepared by a modified Turkevich−Frens method, in which the reaction parameters were adjusted to yield monodisperse spherical nanoparticles of 16 ± 1.2 nm.[27−29] AuNPs were subsequently stabilized and functionalized by a mixed layer of ligands to give fluorescent Au−U11 nanoconjugates (**1**).[23,30] For this purpose, the components were mixed at specific stoichiometric ratios to achieve precise control over the number of functional ligands on each particle, maintaining reproducibility in the nanoparticle production. A short heterobifunctional PEG (11-mercaptoundecyltetra(ethylene glycol) (**2**)), containing both −SH and −OH groups, a fluorescein-bearing bis-carboxylic disulfide molecule (**3**), and Cys-modified U11 peptide (**4**) were used for nanoparticle derivatization. A typical schematic multifunctional nanoparticle, a TEM micrograph of the nanoparticles, and the chemical structure of the ligands utilized for the synthesis are schematically illustrated in Figure 1.

Although conjugation of peptides to the protecting ligand shell of AuNPs is an appealing strategy to preserve their biological activity, we have already had experience in successfully attaching biologically active thiol-containing peptides and proteins directly to the gold surface, observing retained biological functionality.[31,32]

It has been demonstrated that ligand shell composition and ligand density on nanoparticle surface play an important role in targeting efficiency and particle internalization mechanism.[33,34] Our preliminary experiments suggested to us that 3% of FITC groups is the most suitable amount to render the nanoparticles bright enough for binding studies in cells avoiding false positive results (Figure S8, Supporting Information). On the other hand, on the basis of these preliminary data, the U11 peptide amount for further experiments was established to be 3%. More details on the rationale of using this peptide density are reported in the discussion part of the paper. Furthermore, Au−U11 NPs containing 3% U11 peptide, 3% FITC, and 94% HS-PEG-OH ligands are named Au-(**1**) NPs.

In Table 1, representative characteristics of nanoparticles functionalized with different amounts of U11 peptide are summarized. Our results show that it is possible to obtain stable colloidal nanoparticles reaching a maximum 20% of peptide in the ligand shell. However, the insertion of U11 peptide at higher densities (>20%) resulted in poor stability of nanoparticles and their aggregation occurred shortly after functionalization.

Table 1. Characterization of Au−U11 Nanoparticles Containing Different Amounts of U11 Peptide by UV−Visible Spectroscopy, Transmission Electron Microscopy (TEM), Dynamic Light Scattering (DLS), and ζ-Potential

U11, %	SPR, nm	TEM, nm	DLS, nm	ζ-potential, mV
3	524	16 ± 1.2	21.3 ± 1.56	−30.36 ± 1.02
10	524	16 ± 1.2	21.1 ± 1.24	−23.74 ± 3.12
20	524	16 ± 1.2	23.1 ± 1.54	−18.96 ± 1.38

Although AuNPs are known to quench the dye fluorescence because of energy transfer effects,[35,36] we succeeded in obtaining sufficiently bright nanoparticles suitable for biological experiments. Only freshly prepared AuNPs were used for all biological experiments to avoid false negative results. The quenching efficiency of Au-(**1**) NPs was determined by plotting fluorescence spectra from nanoparticles before and after dissolution of the core. The very low intensity of emission peak from Au−U11 NPs grew considerably when the gold core was dissolved in aqua regia (Figure S5, Supporting Information), corresponding to a quenching efficiency of 98.4%.

The physicochemical properties of Au−U11 NPs have been studied by UV−vis, TEM, DLS, and ζ potential techniques. All the particles exhibited a negative charge and a small hydrodynamic diameter, indicating good colloidal stability and a highly monodisperse distribution under physiological conditions (150 mM NaCl at pH 7). To confirm the good colloidal stability of Au-(**1**) NPs, the particles were incubated with NaCl in a 150 mM to 1.5 M concentration range, and UV−vis spectra alterations were evaluated. In addition, nanoparticle stability in cell culture medium was studied by incubating Au-(**1**) NPs with high glucose DMEM lacking phenol red indicator and supplemented with 50% FBS. As shown in Figure S3 (Supporting Information), the particles are perfectly stable both in cell culture medium and even at the highest salt concentrations, since no UV−vis spectra alterations can be noticed.

To assess biological activity of Au-(**1**) NPs, we used uPAR positive human MDA MB 468 cells, uPAR positive murine 4T1 cells, and uPAR negative CAL51 breast cancer cells. In order to exclude possible cytotoxic effects of the particles, cell death was evaluated by annexin V assay after 1, 3, 24, 48, and 72 h of incubation (Figure 2a). No evidence of cytotoxicity was

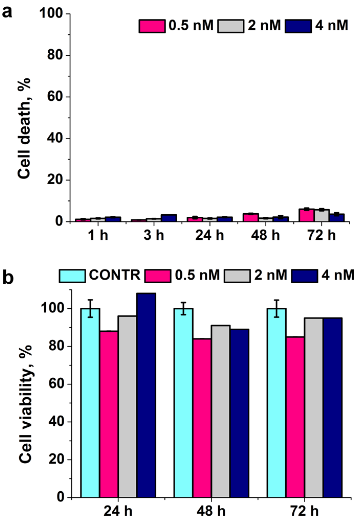

Figure 2. (a) Cell death assay with Au-(**1**) NPs. MDA MB 468 cells were treated with Au-(**1**) NPs (0.5, 2, and 4 nM) for 1, 3, 24, 48, and 72 h. Cell death was assessed to measure the exposure of annexin V evaluated by flow cytometry. The percentage of cell death in untreated population was subtracted. Data are expressed as mean values ± SD of three individual experiments. (b) Cell viability assessed by the MTT assay with Au-(**1**) NPs. MDA MB 468 cells were treated with Au-(**1**) NPs (0.5, 2, and 4 nM) for up to 72 h. The results are expressed as mean values ± SE of six individual experiments. Untreated cells are shown as negative control.

observed in MDA MB 468 cells after short incubation times at the dosages used (0.5, 2, and 4 nM). On the other hand, the nanoparticles induced minimally acceptable in vitro cytotoxicity after longer periods postincubation (24−72 h). As a control experiment, the same assay was performed also on uPAR-negative CAL51 cells, while control Au-PEG NPs were incubated with uPAR-positive MDA MB 468 cells (Figure S11 and Figure S12, respectively, Supporting Information). As indicated in Figure S12, Au−PEG NPs show similar cell death values as Au−U11 NPs after long incubation times, confirming the safety of as-prepared particles to the cells. A cytotoxicity study was performed with a conventional methylthiazolyl-diphenyltetrazolium bromide (MTT) based assay that relies on the color change of MTT by mitochondrial succinate dehydrogenase. The results show that Au-(**1**) NPs are not toxic at commonly used concentrations (Figure 2b).

In addition, in order to ensure that the presence of U11 peptide in the ligand shell does not affect the cytotoxicity of Au-(**1**) NPs, MTT assay with Au-PEG NPs, on MDA MB 468 cell line, as negative control was performed (Figure S13, Supporting Information). The results show a negligible difference between treated and untreated cellular viability profiles, indicating that Au−PEG NPs hardly affect cell profileration.

The binding efficiency between uPAR and Au-(**1**) NPs was studied by fluorescence-based flow cytometry (FACS) as a function of nanoparticle concentration. Cell-associated FITC fluorescence was examined 2 h after incubation of particles with the cells. Our aim was to assess the extent of receptor labeling minimizing nonmediated endocytosis. Hence, cell incubation with nanoparticles was performed at 4 °C. Flow cytometry results are summarized in Figure 3. First, we tested AuNPs containing higher densities of U11 in the ligand shell (5−20%) with the aim to observe a possible binding improvement as a function of ligand density (Figure S8, Supporting Information). However, at very high peptide densities (10−20%) the nanoparticles showed a nonspecific binding to both uPAR-positive (MDA MB 468 and 4T1) and uPAR-negative (CAL51) cells. Importantly, when the U11 amount reaches 20%, the cells show strong aggregation, making it difficult to perform the analysis. This can be explained by a disadvantageous distribution of U11 amino acid sequences on the nanoparticle surface, as it has been already observed by Thanou et al.[6] On the other hand, at lower peptide densities (1%), the binding efficiency was not sufficiently high, probably because of insufficient nanoparticle avidity toward uPAR (Figure S8, Supporting Information). In contrast, treatment of uPAR$^+$ cells with AuNPs containing 3% of U11 peptide produced the most reliable data showing a 2-fold increase in the percentage of cells in the positive region compared to uPAR-negative treated cells (CAL51) at 0.5 nM concentration of AuNPs. At 2 and 4 nM nanoparticle concentration, the percentage of cells in the positive region grew to 53%, indicating the binding in a concentration-dependent manner (Figure 3). Importantly, nanoparticles functionalized with 3% scrambled U11 peptide (**5**) showed negligible binding to all kinds of tested cells, confirming the specificity of Au-(**1**) NPs for uPAR.

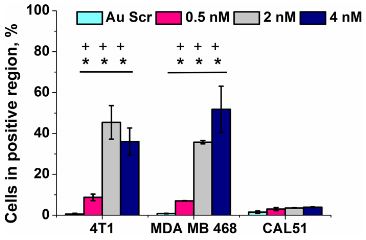

Figure 3. FACS analysis of uPAR targeting with Au-(**1**) NPs on MDA MB468 (uPAR$^+$), 4T1 (uPAR$^+$), and CAL-51 (uPAR$^-$) cells. The cells were incubated for 2 h at 4 °C with 0.5, 2, and 4 nM nanoparticle concentration. The results are expressed as mean values ± SD of three individual experiments normalized on cell proliferation of untreated cells. Student *t* analysis results are calculated and compared to uPAR$^-$ cells (*) and Au-Scr NPs (+).

While flow cytometry is a powerful tool to quantify association of nanoparticles with cells, it does not distinguish between cellular binding and cellular internalization. To confirm cellular uptake and internalization of nanoparticles by breast cancer cells, we performed confocal laser scanning microscopy experiments. Scrambled peptide-conjugated nanoparticles (Au-**scr**) and cell-only controls were also included. The data do indicate the active involvement of a receptor-mediated targeting and U11 specificity to uPAR-positive MDA MB 468 cells, as Au-(**1**) NPs can be observed inside the cell. Negligible internalization was evident with nontargeted Au-**scr** NPs (Figure 4). More images are available in Figure S9, Supporting Information.

In summary, we have presented a robust method for the preparation of urokinase plasminogen activator receptor (uPAR) directed gold nanoparticles for targeting of breast cancer cells. The nanoparticles were functionalized with a short 11-amino acid (U11) peptide derived from the growth factor

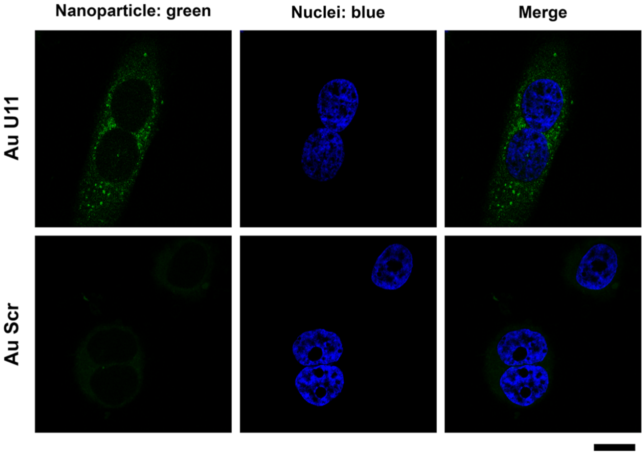

Figure 4. Confocal microscopy study of uPAR targeting with Au-(**1**) and Au-**scr** nanoparticles on MDA MB468 (uPAR$^+$) cells. The cells were incubated for 1 h at 37 °C with 2 nM nanoparticle concentration. Nuclei were stained with 4′,6-diamidino-2-phenylindole (DAPI). Scale bar = 10 μm.

domain of uPA, which is responsible for binding to uPAR due to its epitopal folding. We show that an optimized insertion on gold nanoparticle surface of a 3% U11 in a mixed self-assembled ligand monolayer, including fluorescent dye and intercalating short PEG chains, led to very stable and nontoxic nanoconjugates, which promoted receptor selectivity for improved cell binding and uptake in uPAR-positive cancer cells. The next step will be to prove the efficiency of the optimized U11 nanoparticles for in vivo administration to uPAR-overexpressing breast cancer.

■ ASSOCIATED CONTENT

Ⓢ Supporting Information

Experimental details, HPLC analysis, UV−vis and fluorescence spectra, colloidal stability data, quenching efficiency data, cellular uptake quantification by ICP-AES, confocal microscopy images, and cell death and cell proliferation data. This material is available free of charge via the Internet at http://pubs.acs.org.

■ AUTHOR INFORMATION

Corresponding Author

*E-mail: davide.prosperi@unimib.it.

Author Contributions

[∥]S.A. and E.G. contributed equally.

Notes

The authors declare no competing financial interest.

■ ACKNOWLEDGMENTS

This work was supported by Fondazione Regionale per la Ricerca Biomedica (FRRB), the “NanoBioSense” Project (Sardegna-Lombardia), and Cariplo Foundation (“The MULAN Program”, Project No. 2011-2096). S.A. acknowledges a research fellowship from Nerviano Medical Sciences S.r.l. We thank R. Allevi (CMENA, University of Milan, Italy) for TEM.

■ REFERENCES

(1) Jemal, A., Bray, F., Center, M. M., Ferlay, J., Ward, E., and Forman, D. (2011) Global cancer statistics. *Ca—Cancer J. Clin. 61*, 69−90.

(2) Scott, A. M., Wolchok, J. D., and Old, L. J. (2012) Antibody therapy of cancer. *Nat. Rev. Cancer 12*, 278−287.

(3) Vanneman, M., and Dranoff, G. (2012) Combining immunotherapy and targeted therapies in cancer treatment. *Nat. Rev. Cancer 12*, 237−251.

(4) Stefanidakis, M., and Koivunen, E. (2004) Peptide-mediated delivery of therapeutic and imaging agents into mammalian cells. *Curr. Pharm. Des. 10*, 3033−3044.

(5) Aina, O. H., Sroka, T. C., Chen, M.-L., and Lam, K. S. (2002) Therapeutic cancer targeting peptide. *Biopolymers 66*, 184−199.

(6) Desgrosellier, J. S., and Cheresh, D. A. (2010) Integrins in cancer: biological implications and therapeutic opportunities. *Nat. Rev. Cancer 10*, 9−22.

(7) Danhier, F., Le Breton, A., and Préat, V. (2012) RGD-based strategies to target alpha(v) beta(3) integrin in cancer therapy and diagnosis. *Mol. Pharmaceutics 9*, 2961−2973.

(8) Lee, M. H., Kim, J., Han, H. J., Bhuniya, S., Sessler, J. L., Kang, C., and Seung Kim, J. (2012) Direct fluorescence monitoring of the delivery and cellular uptake of a cancer-targeted RGD peptide-appended naphthalimide theragnostic prodrug. *J. Am. Chem. Soc. 30* (134), 12668−12674.

(9) Park, J., Singha, K., Son, S., Kim, J., Namgung, R., Yun, C.-O., and Kim, W. J. (2012) A review of RGD-functionalized nonviral gene delivery vectors for cancer therapy. *Cancer Gene Ther. 19*, 741−748.

(10) Wang, M., Lowik, D. W. P. M., Miller, A. D., and Thanou, M. (2009) Targeting the urokinase plasminogen activator receptor with synthetic self-assembly nanoparticles. *Bioconjugate Chem. 20*, 32−42.

(11) Wang, M., Miller, A. D., and Thanou, M. (2013) Effect of surface charge and ligand organization on the specific cell-uptake of uPAR-targeted nanoparticles. *J. Drug Targeting 21*, 684−692.

(12) LeBeau, A. M., Duriseti, S., Murphy, S. T., Pepin, F., Hann, B., Gray, J. W., VanBrocklin, H. F., and Craik, C. S. (2013) Targeting uPAR with antagonistic recombinant human antibodies in aggressive breast cancer. *Cancer Res. 73*, 2070−2081.

(13) Rao, J. S., Gondi, C., Chetty, C., Chittivelu, S., Joseph, P. A., and Lakka, S. S. (2005) Inhibition of invasion, angiogenesis, tumor growth, and metastasis by adenovirus-mediated transfer of antisense uPAR and MMP-9 in non-small cell lung cancer cells. *Mol. Cancer Ther. 4*, 1399−1408.

(14) Cantero, D., Friess, H., Deflorin, J., Zimmermann, A., Bründler, M. A., Riesle, E., Korc, M., and Büchler, M. W. (1997) Enhanced expression of urokinase plasminogen activator and its receptor in pancreatic carcinoma. *Br. J. Cancer 75*, 388−395.

(15) Ma, Y. Y., and Tao, H. Q. (2012) Role of urokinase plasminogen activator receptor in gastric cancer: a potential therapeutic target. *Cancer Biother. Radiopharm. 27*, 285−290.

(16) Li, D., Liu, S., Shan, H., Conti, P., and Li, Z. (2013) Urokinase plasminogen activator receptor (upar) targeted nuclear imaging and radionuclide therapy. *Theranostics 3*, 507−515.

(17) Mazzucchelli, S., Colombo, M., Verderio, P., Rozek, E., Andreata, F., Galbiati, E., Tortora, P., Corsi, F., and Prosperi, D. (2013) Orientation-controlled conjugation of HALO-fused homing peptides to multifunctional nanoparticles for specific recognition of cancer cells. *Angew. Chem., Int. Ed. 52*, 3121−3125.

(18) Bhattacharyya, S., Singh, R. D., Pagano, R., Robertson, J. D., Bhattacharya, R., and Mukherjee, P. (2012) Switching the targeting pathways of a therapeutic antibody by nanodesign. *Angew. Chem., Int. Ed. 51*, 1563−1567.

(19) Huang, Y.-F., Liu, H., Xiong, X., Chen, Y., and Tan, W. (2009) Nanoparticle-mediated IgE-receptor aggregation and signaling in RBL mast cells. *J. Am. Chem. Soc. 131*, 17328−17334.

(20) Häkkinen, H. (2012) The gold−sulfur interface at the nanoscale. *Nat. Chem. 4*, 443−455.

(21) Hosta-Rigau, L., Olmedo, I., Arbiol, J., Cruz, L. J., Kogan, M. J., and Albericio, F. (2010) Multifunctionalized gold nanoparticles with peptides targeted to gastrin-releasing peptide receptor of a tumor cell line. *Bioconjugate Chem. 21*, 1070−1078.

(22) (a) Yang, S.-J., Lin, F.-H., Tsai, K.-C., Wei, M.-F., Tsai, H.-M., Wong, J.-M., and Shieh, M.-J. (2010) Folic acid-conjugated chitosan nanoparticles enhanced protoporphyrin IX accumulation in colorectal cancer cells. *Bioconjugate Chem. 21*, 679−689. (b) Ventola, C. L. (2012) The nanomedicine revolution. Part 2: Current and future clinical applications. *P T 37* (10), 582−591. (c) Thakor, A. S., Luong, R., Paulmurugan, R., Lin, F. I., Kempen, P., Zavaleta, C., Chu, P., Massoud, T. F., Sinclair, R., and Gambhir, S. S. (2011) The fate and toxicity of Raman-active silica−gold nanoparticles in mice. *Sci. Transl. Med. 3* (79), 79ra33. (d) Paciotti, G. F., Myer, L., Weinreich, D., Goia, D., Pavel, N., McLaughlin, R. E., and Tamarkin, L. (2004) Colloidal gold: a novel nanoparticle vector for tumor directed drug delivery. *Drug Delivery 11*, 169−183.

(23) Karakoti, A. S., Das, S., Thevuthasan, S., and Seal, S. (2011) PEGylated inorganic nanoparticles. *Angew. Chem., Int. Ed. 50*, 1980−1994.

(24) Gao, J., Huang, X., Liu, H., Zan, F., and Ren, J. (2012) Colloidal stability of gold nanoparticles modified with thiol compounds: bioconjugation and application in cancer cell imaging. *Langmuir 28*, 4464−4471.

(25) Swartz, J. D., Gulka, C. P., Haselton, F. R., and Wright, D. W. (2011) Development of a histidine-targeted spectrophotometric sensor using Ni(II)NTA-functionalized Au and Ag nanoparticles. *Langmuir 27*, 15330−15339.

(26) Krpetic, Z., Davidson, A. M., Volk, M., Levy, R., Brust, M., and Cooper, D. L. (2013) High-resolution sizing of monolayer-protected gold clusters by differential centrifugal sedimentation. *ACS Nano 7*, 8881−8890.

(27) Turkevich, J., Cooper Stevenson, P., and Hillier, J. (1951) A study of the nucleation and growth processes in the synthesis of colloidal gold. *Discuss. Faraday Soc. 11*, 55−75.

(28) Turkevich, J., Stevenson, P. C., and Hillier, J. (1953) The formation of colloidal gold. *J. Phys. Chem. 57*, 670−673.

(29) Frens, G. (1973) Controlled nucleation for the regulation of the particle size in monodisperse gold suspensions. *Nat. Phys. Sci. 241*, 20−22.

(30) Pensa, E., Cortes, E., Cortney, G., Carro, P., Vericat, C., Fonticelli, M. H., Benitez, G., Rubert, A. A., and Salvarezza, R. C. (2012) The chemistry of the sulfur−gold interface: in search of a unified model. *Acc. Chem. Res. 45*, 1183−1192.

(31) Colombo, M., Mazzucchelli, S., Collico, V., Avvakumova, S., Pandolfi, L., Corsi, F., Porta, F., and Prosperi, D. (2012) Protein-assisted one-pot synthesis and biofunctionalization of spherical gold nanoparticles for selective targeting of cancer cells. *Angew. Chem., Int. Ed. 37*, 9272−9275.

(32) Scari, G., Porta, F., Fascio, U., Avvakumova, S., Dal Santo, V., de Simone, M., Saviano, M., Leone, M., del Gatto, A., Pedone, C., and Zaccaro, L. (2012) Gold nanoparticles capped by a GC-containing peptide functionalized with an RGD motif for integrin targeting. *Bioconjugate Chem. 23*, 340−349.

(33) Ma, L. L., Tam, J. O., Willsey, B. W., Rigdon, D., Ramesh, R., Sokolov, K., and Johnston, K. P. (2011) Selective targeting of antibody conjugated multifunctional nanoclusters (nanoroses) to epidermal growth factor receptors in cancer cells. *Langmuir 27*, 7681−7690.

(34) Jiang, W., Kim, B. Y. S., Rutka, J. T., and Chan, W. C. W. (2008) Nanoparticle-mediated cellular response is size-dependent. *Nat. Nanotechnol. 3*, 145−150.

(35) Tu, Y., Wu, P., Zhang, H., and Cai, C. (2012) Fluorescence quenching of gold nanoparticles integrating with a conformation-switched hairpin oligonucleotide probe for microRNA detection. *Chem. Commun. 48*, 10718−10720.

(36) Dulkeith, E., Ringler, M., Klar, T. A., Feldmann, J., Munoz Javier, A., and Parak, W. J. (2005) Gold nanoparticles quench fluorescence by phase induced radiative rate suppression. *Nano Lett. 5*, 585−588.

ChemComm

COMMUNICATION

View Article Online
View Journal | View Issue

Cite this: *Chem. Commun.*, 2014, **50**, 11029

Received 28th April 2014,
Accepted 31st July 2014

DOI: 10.1039/c4cc03159h

www.rsc.org/chemcomm

Gold nanoparticles decorated by clustered multivalent cone-glycocalixarenes actively improve the targeting efficiency toward cancer cells†

Svetlana Avvakumova,‡[a] Paola Fezzardi,‡[b] Laura Pandolfi,[a] Miriam Colombo,[a] Francesco Sansone,[b] Alessandro Casnati*[b] and Davide Prosperi*[a]

A novel approach for multivalent targeting by using gold nanoparticles noncovalently decorated by tight functionalization with a cone-glycocalixarene bearing four mannose units is reported. The targeting efficiency of these multivalent nanoparticles is shown to be remarkably improved compared to that of nanoparticles bearing a monovalent mannosylated derivative.

Multivalent nanoplatforms have attracted great interest in nanobiotechnology because of their ability to promote the targeting of specific cancer cells by simultaneous binding to multiple receptors. Multivalency enhances the overall affinity of a nanoparticle (NP) containing low-affinity ligands by expanding the number of ligating units used for binding.[1] The development of multivalent ligands to discriminate between healthy and cancer cells is a major demand in current research. On the other hand, functionalized NPs are emerging tools for the delivery of drugs to malignant cells and tissues.[2] Calixarenes have been used in molecular recognition and supramolecular chemistry, thanks to their straightforward synthesis even in kilo-scale and well-encoded protocol for their functionalization.[3] Calixarenes can be ideal scaffolds for preparation of multivalent ligands since their valency can be easily varied, while the stereochemical orientation of the ligating arms finely tuned by shaping the scaffold conformation.[4] Glycocalixarenes, *i.e.* calixarenes adorned with a multiple presentation of carbohydrate units, were shown to have remarkable ability to efficiently interact with multivalent carbohydrate recognition proteins (lectins), thus playing a pivotal role in inhibiting pathological events or triggering specific physiological responses.[5] Indeed, carbohydrates are involved in the process of cell recognition and growth and facilitate cellular adhesion in normal processes as well as in the proliferation and metastatic progression of many cancers.[6] Moreover, carbohydrates look particularly promising to obtain functional targeted NPs,[7] as they exhibit strongly reduced immunogenicity compared with peptides and antibodies.[8] Therefore, combining these advantageous features, we reasoned that the use of carbohydrate-functionalized calixarenes on NPs could amplify the carbohydrate–lectin interaction by exploiting multivalency and preorganization of the saccharide repeating units in clusters.

Gold nanoparticles (AuNPs) have been widely used in tumor targeting applications because of their straightforward synthesis and multiple possibilities of functionalization.[9] Most strategies of AuNPs fabrication involve water-phase synthesis by citrate/sodium borohydride reduction with subsequent citrate exchange to different functional molecules.[10] Calixarenes have been grafted on AuNPs *via* Au–thiol chemistry, however, this would require long and tedious functionalization of calixarenes with thiol chains using a chemistry not always compatible with carbohydrate units present on the macrocycle.[11] To the best of our knowledge, no examples of glycocalixarene-functionalized AuNPs were reported so far and even no water-dispersible AuNPs could be obtained exploiting the functionalization with calixarenes.

In this study, we propose a facile, straightforward and robust method for the functionalization of colloidal AuNPs with calixarenes taking advantage of the effective and stable hydrophobic interactions between the calixarene backbone and the dodecanethiol layer capping the surface of AuNPs. We demonstrate that multivalent glycocalixarene-functionalized AuNPs can be ideal candidates to develop clustered multivalent nanosystems for the efficient targeting of cancer cells, alternative to the commonly adopted peptide- or antibody-based nanoconjugates. We used an amphiphilic cone-tetra-man-calix[4]arene to improve the multivalency of NPs (Fig. 1). In brief, the calixarene was synthesized by a "click" reaction starting from tetraamine-tetrapropyl-calix[4]arene, fixed in the cone structure, and peracetylated man-α-isothiocyanate. After deacetylation, the tetramannosylthioureidocalix[4]arene

---

[a] *NanoBioLab, Dipartimento di Biotecnologie e Bioscienze, Università degli Studi di Milano-Bicocca, Piazza della Scienza, 2, Milano, 20126, Italy. E-mail: davide.prosperi@unimib.it; Web: http://www.nanobiolab.btbs.unimib.it*

[b] *Dipartimento di Chimica, Università degli Studi di Parma, Parco/Area delle Scienze 17/A, Parma, 43124, Italy. E-mail: alessandro.casnati@unipr.it*

† Electronic supplementary information (ESI) available: Synthesis and characterization of organic compounds and gold nanoparticles; colloidal stability and protein adsorption; cell culture, nanoparticle uptake and receptor inhibition protocols; cell death assay. See DOI: 10.1039/c4cc03159h

‡ These authors contributed equally to this work.

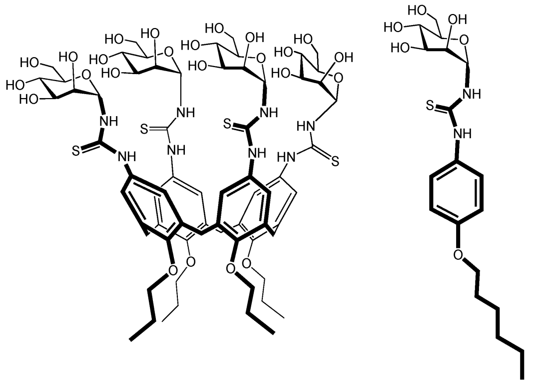

Fig. 1 Structure of amphiphilic Calix-Man (left) and Mon-Man (right).

(Calix-Man), which was isolated and characterized (see ESI†), showed a pronounced amphiphilic character being poorly soluble in most of the organic solvents and in water. Colloidal AuNPs were synthesized by the Brust–Schiffrin method to give hydrophobic dodecanethiol-stabilized AuNPs ($\sim$6 nm).[12]

A simple and straightforward approach to render the AuNPs water-soluble was realized by a chloroform-to-water phase transfer using as a capping agent, the mannose-functionalized amphiphilic glycocalixarene (Scheme 1). The molar ratio between Calix-Man and AuNPs suitable for successful phase transfer of AuNPs was optimized to obtain a complete water-dispersion of NPs. The amphiphilic calixarene molecules intercalate the hydrophobic dodecanethiol surfactant layer with their hydrophobic moieties and impart water solubility to the nanocomplex by taking advantage of their hydrophilic mannose groups. The strategy of using amphiphilic polymers to render NPs water-soluble has been successfully used by different researchers.[13] However, in order to confer the targeting properties, such NPs need to be subsequently functionalized using various coupling chemistries. In our innovative approach, amphiphilic calixarene molecules were previously modified to provide the necessary recognition moieties, thus resulting in a single-step nanoparticle functionalization and colloidal stabilization.

In order to compare the targeting efficiency of the clustered multivalent Au–Calix-Man NPs with that of AuNPs functionalized with a classical acyclic monovalent system, we decided to synthesize a simpler glycoside, consisting of a single phenol group bearing only one saccharide unit (Mon-Man, Fig. 1), thus resembling the monomeric homologue of the tetravalent calixarene compound. The simple multivalent glyco-AuNPs were synthesized by the same procedure using a four-fold molar amount of Mon-Man with respect to Calix-Man. Hence, the experimental number of Calix-Man and Mon-Man molecules intercalated into the dodecanthiol ligand shell was found to be approximately 1390 and 4210 per nanoparticle, respectively. The calculation was made determining the calixarene and monomer concentration by measuring the absorbance at 230 nm. Significantly, the introduction of mannose residues through a calixarene scaffold allowed us to increase (by roughly 25–30%) the maximal number of saccharide units that can be presented on the surface of NPs.

The TEM micrograph shows water-dispersible NPs with a mean diameter of 6.0 ± 1.1 nm (Fig. 2). Both Au–Calix-Man and Au–Mon-Man were stable for months in an aqueous solution. The surface charge was determined by ζ potential measurements in Milli-Q water by addition of 0.1 M NaCl, resulting in -41.31 ± 1.79 mV and -37.65 ± 1.94 mV for Au–Calix-Man and Au–Mon-Man NPs, respectively. Hydrodynamic diameters of NPs were recorded in phosphate buffer saline (PBS) by dynamic light scattering (DLS). Values of 20.1 ± 1.6 nm and 27.7 ± 2.4 nm were found for Calix-Man and Mon-Man AuNPs, respectively, suggesting a higher colloidal stability of Au–Calix-Man. In principle, the monovalent mannose unit could be in equilibrium between the intercalated and free state, because the binding affinity is lower than that of calix, which would result in a lower effective mannose concentration than expected, leading to a concomitantly lower targeting effect. However, we have to highlight that Mon-Man is very insoluble in water and its intercalation between hydrophobic chains on the surface of NPs seems as efficient as that of Calix-Man, which makes the dissociation of mannoside molecules from its intercalated state unfavourable. The concentrations of both Calix-Man and Mon-Man on NPs were monitored by UV measurements and no appreciable decrease of absorbance was found even after several washings of the functionalized NPs with buffered solutions.

The colloidal stability of the NPs in cell culture medium (DMEM) was assessed by UV-vis spectroscopy by recording the changes in the aggregation parameter (AP), as a variation of the integrated absorbance in the range between 600 and 700 nm.[12] It is evident that both kinds of NPs show good colloidal stability

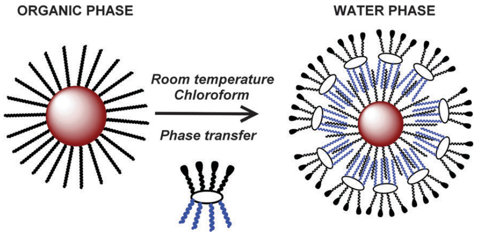

Scheme 1 Schematic representation of Au–Calix-Man NP synthesis *via* chloroform-to-water phase transfer.

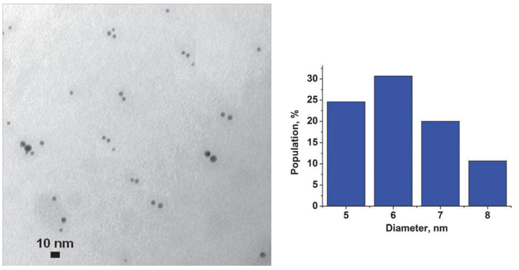

Fig. 2 TEM micrograph and size distribution diagram of Au–Calix-Man NPs. Scale bar = 10 nm.

in DMEM, with a maximal AP lower than 0.4. It has been shown elsewhere that, when NPs are immersed in biological media, they are rapidly coated by a so-called ''protein corona'', which may affect both colloidal stability and uptake by cells.[14] As a consequence, this can result in a partial or even complete loss of functionality of the immobilized targeting molecules.[15] To probe such a tendency in our NPs, we evaluated their interaction with bovine serum albumin (BSA), as a model abundant protein in serum. After incubation of both clustered multivalent and simple multivalent NPs (50 μg mL^{-1}) with FITC-labeled BSA (BSA-FITC, 250 μg mL^{-1}) for 24 h at room temperature, NPs were separated by centrifugation, and supernatants were analyzed by fluorescence spectroscopy to measure the amount of unbound BSA-FITC (Fig. S8, ESI†). The fluorescence intensity was reduced by 8% and 10% after incubation with Au–Man-Calix and Au–Mon-Man, respectively, which is rather low compared to common values obtained with uncoated and peptide-coated NPs.[15] In order to assess whether the mannose moiety and/or the ligand structure was indeed responsible for the ''stealth'' properties of the NPs, AuNPs prepared in the same manner but functionalized with an amphiphilic polymer often utilized for aqueous stabilization of colloidal NPs (PMA)[13] were used. This polymer did not contain any saccharide moieties. In this case, we observed a 23% reduction of fluorescence, confirming good ''stealth'' properties for the calixarene-modified AuNPs.

To assess the potential of mannose functional NPs in binding receptors that are known to occur in diseased tissues, we studied the targeting efficiency of our NPs using a mannose receptor-expressing cervical cancer cell line, HeLa.[16] Carbohydrates have been used previously on the surface of functional NPs to enhance the cellular uptake efficiency and specificity.[14] Firstly, the cytotoxicity of Au–Calix-Man and Au–Mon-Man in HeLa cells was evaluated using the Annexin-PE-Cy5 apoptosis detection kit. NPs were incubated (10 and 20 nM) for 3 and 24 h at 37 °C and the cells were stained with a fluorescent conjugate of Annexin V. The results of flow cytometry analysis revealed that both kinds of NPs were not cytotoxic at these relatively high concentrations (Fig. S9, ESI†).

In a second step, we investigated the cell uptake of functionalized NPs. Au–Calix-Man and Au–Mon-Man (50 nM) were incubated with HeLa cells for 2 h at 37 °C. As a negative control, mannose-free Au–PMA NPs were used. The cells were properly treated and the gold content was measured by ICP-AES. This method is much more reliable than fluorescence labeling, when NPs quantification is desired using gold NPs, as quenching effects are unavoidable with gold surface. The results in Fig. 3 show that the uptake of NPs was strongly improved by the presence of mannose. This mannose-dependency of the process was evidenced by the addition of dextran (often used as a mannose receptor inhibitor),[18] which blocks the uptake for Au–Calix-Man and Au–Mon-Man NPs. On the other hand, mannose-free Au–PMA NPs were internalized by the cells *via* a less efficient passive endocytosis poorly influenced by the addition of dextran. Remarkably, the cellular uptake of Au–Calix-Man was three-fold higher than that of Au–Mon-Man, indicating a significantly enhanced ability of the clustered multivalent NPs compared to the simple multimannosylated ones to interact with cancer cells (Scheme 2). Although there is at least a 25% higher mannose content on Au–Calix-Man, this is not feasible to account for such a remarkable increment in the targeting efficiency of functionalized NPs. We suggest that a pronounced cluster effect due to the calixarene structure plays a major role in enforcing the oriented multivalent interaction with mannose receptors, as previously documented with other calixarenes in different biological contexts.[17] In addition, the binding of clustered multivalent Au–Calix-Man NPs to a single mannose receptor leads to increased statistical rebinding due to enhanced local concentration of NPs that favors nanoparticle uptake by the cells.[18,19] Finally, the experiment with dextran demonstrates that inhibiting the functionality of the mannose receptor nearly completely prevent the uptake of glyco-NPs, suggesting a low intrinsic propensity of mannosylated AuNPs to be passively internalized.

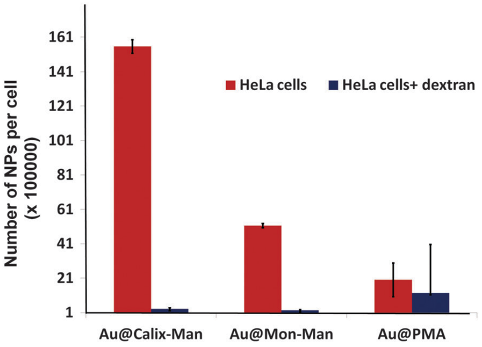

Fig. 3 Quantified nanoparticle association at 37 °C in HeLa cells without a blocking ligand (red bars) and with dextran to block binding to the mannose receptor (blue bars). All NPs were administered at a concentration of 50 nM.

In conclusion, this preliminary proof-of-concept study highlights the usefulness of using clustered multivalent ligands supported on gold nanoplatforms for improving the efficiency

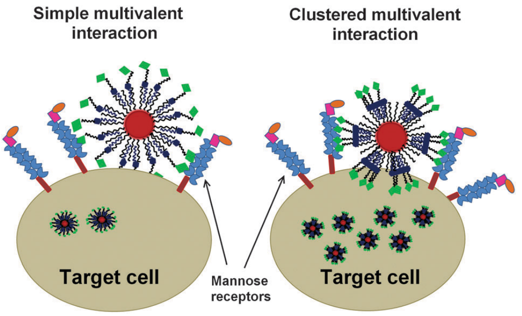

Scheme 2 Schematic representation of enhanced targeting efficiency of the mannose receptor by simple multivalent interaction between Au–Mon-Man NPs and a target cell (left panel) *versus* clustered multivalent interaction between Au–Calix-Man NPs and a target cell (right panel).

and sensitivity in targeting cancer cells. In particular, calixarenes are promising candidates as they can be easily functionalized with appropriate targeting moieties and used as phase transfer agents for a wide range of nanocrystals. Therefore, designing multivalent molecular systems, such as glycocalix derivatives, offers great promise in the search for selective targeting ligands alternative to more common peptides and antibodies, in the purpose of developing novel nanocarriers of a wide range of drugs with reduced immunogenicity and improved therapeutic indices.

This work was supported by MIUR (PRIN2010JMAZML MultiNanoIta), EU-COST Action CM1102 'MultiGlycoNano', Cariplo (2011–2096), FRRB and Regione Lombardia. We thank R. Allevi (CMENA, University of Milan) for TEM image and CIM (Parma University 'G. Casnati') for the use of NMR and Mass facilities.

Notes and references

1 (*a*) N. M. Barkey, N. K. Tafreshi, J. S. Josan, C. R. De Silva, K. N. Sill, V. J. Hruby, R. J. Gillies, D. L. Morse and J. Vagner, *J. Med. Chem.*, 2011, **54**, 8078–8084; (*b*) S. Avvakumova, M. Colombo, P. Tortora and D. Prosperi, *Trends Biotechnol.*, 2014, **32**, 11–20; (*c*) J.-H. Park, G. von Maltzahn, L. Zhang, M. P. Schwartz, E. Ruoslahti, S. N. Bhatia and M. J. Sailor, *Adv. Mater.*, 2008, **20**, 1630–1635; (*d*) S. Hong, P. R. Leroueil, I. J. Majoros, B. G. Orr, J. R. Baker and M. M. Banaszak Holl, *Chem. Biol.*, 2007, **14**, 107–115.

2 (*a*) Y. Cheng, J. D. Meyers, A.-M. Broome, M. E. Kenney, J. P. Basilion and C. Burda, *J. Am. Chem. Soc.*, 2011, **133**, 2583–2591; (*b*) M. Piazza, M. Colombo, I. Zanoni, F. Granucci, P. Tortora, J. Weiss, T. Gioannini, D. Prosperi and F. Peri, *Angew. Chem., Int. Ed.*, 2011, **50**, 622–626.

3 (*a*) C. D. Gutsche, *Calixarenes: an introduction*, RSC Publishing, 2nd edn, 2008; (*b*) L. Baldini, F. Sansone, A. Casnati and R. Ungaro, Calixarenes in molecular recognition, in *Supramolecular Chemistry: From Molecules to Nanomaterials*, ed. J. W. Steed and P. A. Gale, John Wiley & sons, Chichester, 2012, pp. 863–894.

4 (*a*) L. Baldini, A. Casnati, F. Sansone and R. Ungaro, *Chem. Soc. Rev.*, 2007, **36**, 254–266; (*b*) A. Dondoni and A. Marra, *Chem. Rev.*, 2010, **110**, 4949–4977; (*c*) F. Sansone and A. Casnati, *Chem. Soc. Rev.*, 2013, **42**, 4623–4639.

5 (*a*) D. Arosio, M. Fontanella, L. Baldini, L. Mauri, A. Bernardi, A. Casnati, F. Sansone and R. Ungaro, *J. Am. Chem. Soc.*, 2005, **127**, 3660–3661; (*b*) J. Garcia-Hartjes, S. Bernardi, C. A. G. M. Weijers, T. Wennekes, M. Gilbert, F. Sansone, A. Casnati and H. Zuilhof, *Org. Biomol. Chem.*, 2013, **11**, 4340–4349; (*c*) S. Cecioni, R. Lalor, B. Blanchard, J. P. Praly, A. Imberty, S. E. Matthews and S. Vidal, *Chem. – Eur. J.*, 2009, **15**, 13232–13240; (*d*) C. Geraci, G. M. L. Consoli, E. Galante, E. Bousquet, M. Pappalardo and A. Spadaro, *Bioconjugate Chem.*, 2008, **19**, 751–758; (*e*) S. Aleandri, A. Casnati, L. Fantuzzi and G. Mancini, *Org. Biomol. Chem.*, 2013, **11**, 4811–4817.

6 E. Gorelik, U. Galili and A. Raz, *Cancer Metastasis Rev.*, 2001, **20**, 245–277.

7 (*a*) A. G. Barrientos, J. M. de la Fuente, T. C. Rojas, A. Fernandez and S. Penades, *Chem. – Eur. J.*, 2003, **9**, 1909–1921; (*b*) M. Marradi, F. Chiodo, I. García and S. Penadés, *Chem. Soc. Rev.*, 2013, **42**, 4728–4745.

8 (*a*) S. Mornet, S. Vasseur, F. Grasset and E. Duguet, *J. Mater. Chem.*, 2004, **14**, 2161–2175; (*b*) M. Hattori, K. Nagasawa, K. Ohgata, N. Sone, A. Fukuda, H. Matsuda and K. Takahashi, *Bioconjugate Chem.*, 2000, **11**, 84–93; (*c*) S. van Drunen Littel-van den Hurk, G. Hughes and L. A. Babiuk, *J. Gen. Virol.*, 1990, **71**, 2053–2063; (*d*) A. M. Sinclair and S. Elliott, *J. Pharm. Sci.*, 2005, **94**, 1626–1635.

9 (*a*) M. Colombo, S. Mazzucchelli, V. Collico, S. Avvakumova, L. Pandolfi, F. Corsi, F. Porta and D. Prosperi, *Angew. Chem., Int. Ed.*, 2012, **124**, 9406–9409; (*b*) Z. Krpetic, S. Saleemi, I. A. Prior, V. See, R. Qureshi and M. Brust, *ACS Nano*, 2011, **5**, 5195–5201.

10 (*a*) J. Turkevich, P. Cooper Stevenson and J. Hiller, *Discuss. Faraday Soc.*, 1951, **11**, 55–75; (*b*) J. Turkevich, P. C. Stevenson and J. Hiller, *J. Phys. Chem.*, 1953, **57**, 670–673; (*c*) G. Frens, *Nat. Phys. Sci.*, 1973, **241**, 20–22.

11 (*a*) A. Arduini, D. Demuru, A. Pochini and A. Secchi, *Chem. Commun.*, 2005, 645–648; (*b*) T. R. Tshikhudo, D. Z. X. Wang, M. Brust, A. Secchi, A. Arduini and A. Pochini, *Angew. Chem., Int. Ed.*, 2005, **44**, 2913–2916.

12 M. Brust, M. Walker, D. Bethell, D. J. Schiffrin and R. Whyman, *Chem. Commun.*, 1994, 801–802.

13 (*a*) L. Fiandra, S. Mazzucchelli, C. De Palma, M. Colombo, R. Allevi, S. Sommaruga, E. Clementi, M. Bianchi, D. Prosperi and F. Corsi, *ACS Nano*, 2013, **7**, 6092–6102; (*b*) C. A. J. Lin, R. A. Sperling, J. K. Li, T. Y. Yang, M. Zanella, W. H. Chang and W. J. Parak, *Small*, 2008, **4**, 334–341; (*c*) R. Levy, N. T. K. Thanh, R. C. Doty, I. Hussain, R. J. Nichols, D. J. Schiffrin, M. Brust and D. G. Fernig, *J. Am. Chem. Soc.*, 2004, **126**, 10076–10084.

14 (*a*) T. Cedervall, I. Lynch, S. Lindman, T. Berggård, E. Thulin, H. Nilsson, K. A. Dawson and S. Linse, *Proc. Natl. Acad. Sci. U. S. A.*, 2007, **104**, 2050–2055; (*b*) M. Lundqvist, J. Stigler, G. Elia, I. Lynch, T. Cedervall and K. A. Dawson, *Proc. Natl. Acad. Sci. U. S. A.*, 2008, **105**, 14265–14270; (*c*) G. Maiorano, S. Sabella, B. Sorce, V. Brunetti, M. A. Malvindi, R. Cingolani and P. P. Pompa, *ACS Nano*, 2010, **4**, 7481–7491.

15 (*a*) M. P. Monopoli, C. Åberg, A. Salvati and K. A. Dawson, *Nat. Nanotechnol.*, 2012, **7**, 779–786; (*b*) A. Salvati, A. S. Pitek, M. P. Monopoli, K. Prapainop, F. Baldelli Bombelli, D. R. Hristov, P. M. Kelly, C. Åberg, E. Mahon and K. A. Dawson, *Nat. Nanotechnol.*, 2013, **8**, 137–143.

16 (*a*) N. Zheng, L. Yin, Z. Song, L. Ma, H. Tang, N. P. Gabrielson, H. Lu and J. Cheng, *Biomaterials*, 2014, **35**, 1302–1314; (*b*) J. S. Basuki, L. Esser, H. T. T. Duong, Q. Zhang, P. Wilson, M. R. Whittaker, D. M. Haddleton, C. Boyer and T. P. Davis, *Chem. Sci.*, 2014, **5**, 715–726; (*c*) B. Carrillo-Conde, E.-H. Song, A. Chavez-Santoscoy, Y. Phanse, A. E. Ramer-Tait, N. L. B. Pohl, M. J. Wannemuehler, B. H. Bellaire and B. Narasimhan, *Mol. Pharmaceutics*, 2011, **8**, 1877–1886; (*d*) J. H. Ahire, I. Chambrier, A. Mueller, Y. Bao and Y. Chao, *ACS Appl. Mater. Interfaces*, 2013, **5**, 7384–7391.

17 V. Bagnacani, V. Franceschi, M. Bassi, M. Lomazzi, G. Donofrio, F. Sansone, A. Casnati and R. Ungaro, *Nat. Commun.*, 2013, **4**, 1721.

18 S. M. D'Addio, S. Baldassano, L. Shi, L. Cheung, D. H. Adamson, M. Bruzek, J. E. Anthony, D. L. Laskin, P. J. Sinko and R. K. Prud'homme, *J. Controlled Release*, 2013, **168**, 41–50.

19 (*a*) B. Powell Gray, S. Li and K. C. Brown, *Bioconjugate Chem.*, 2013, **24**, 85–96; (*b*) L. L. Kiessling, J. E. Gestwicki and L. E. Strong, *Angew. Chem., Int. Ed.*, 2006, **45**, 2348–2368.